UNIVERSIDAD NACIONAL AUTÓNOMA DE MÉXICO

PROGRAMA DE POSGRADO EN ASTROFÍSICA

Instituto de Astronomía, UNAM

Ondas de choque internas de cuásares, micro-cuásares y destellos de rayos gamma.

PARA OPTAR POR EL GRADO DE
DOCTOR EN CIENCIAS (ASTROFÍSICA)

PRESENTA
M. en C. Yaxk'in Ú Kan Coronado González

TUTOR
DR. SERGIO MENDOZA RAMOS. INSTITUTO DE ASTRONOMÍA

MÉXICO, D. F. JUNIO 2015

Internal shock waves from quasars, micro-quasars and gamma ray bursts

Yaxk'in U Kan Coronado González

June, 2015

Acknowlegments

This dissertation would not have been possible without the help of so many people: people not only from the Instituto de Astronomía of the the Universidad Nacional Autónoma de México (IA-UNAM), but also from outside.

I would like to express my special appreciation and thanks to my advisor Dr. Sergio Mendoza Ramos, you have been a tremendous mentor for me. I would like to thank you for encouraging my research and for allowing me to grow as a research scientist. Your advice on both research as well as on my career have been priceless. I would also like to thank my committee members, Dra. Deborah Dultzin Kessler, Dr. Francisco Siddhartha Guzmán Murillo, Dr. Omar López Cruz, Dr. Pablo Luis Rendón Garrido, for serving as my committee members even at hardship. I also want to thank you for your brilliant comments and suggestions, thanks to you.

I take this opportunity to express gratitude to all of the Instituto de Astronomía members for their help and support, in particular my teachers: Xavier Hernandez, Juan Carlos Hidalgo, Debohra Dultzin, Barbara Pichardo, Hector Hernandez, Octavio Valenzuela, Antonio Garcia Barreto, and all the amazing people in the Institute. Thanks also to collaborators Erika Benitez, Ignacio Cabrera, Oliver Lopez and Marco Sorcia.

I would especially like to thank to Julieta Fierro for sharing expertise, and sincere and valuable guidance and encouragement extended to me. Thanks also to Nahiely Flores, Sandro Mendoza and Antonio Vazquez and my gratitude for their friendship.

I would especially like to thank to Bertha Vazquez for her patience and support with all the administrative process.

I wish to acknowledge the help provided by Noemi Rebollo, Ana Zavaleta, Pavel Sulca, Omar Anguiano, Miguel Monroy, Zeus Valtierra and Rut Salazar at Falcultad de Ciencias as a teacher assistant.

A special thanks to my parents Jorge and Florencia, and my sisters Lucila and Yatzibeth

for always been listening to me, giving me support and all their encouragement. Words cannot express how grateful me.

Thanks also to my friends during these past years, in the IA-UNAM and the Facultad de Ciencias Rut Salazar, Sandro Mendoza, Tula Bernal, Mario de Leo, Aldo Batta, Rodrigo Sacahui, Roberto Figuera, Mary Loly, Eva Martinez, Claudio Toledo, Antonio Vazquez, Ernesto Barrientos, Miguel Monroy, Omar Anguiano, Jackie Garcia, Zeus Valtierra, Jhonatan Reyes, Francisco Hernandez and all the post-doc, Phd. students, Master degree students and undergraduate students who I meet in all this years.

I would like to offer my special thanks to Alejandro Radillo for his help and friendship. Also for their friendship all these years to Juan Carlos Cajas, Elba Campos, Yolitzi Saldívar, Roberto Romero, Gustavo Armendariz, Eduardo Barrios, Francisco Rodriguez, Zaira Luz, Alejandro Radillo and all my friends who encourage me to conclude this stage. Also I would like to thank to Esmeralda Carrasco for being so patient and kindly with me during the last stages of the PHD. She provide me a lot of support.

My founding was provided by the Consejo Nacional de Ciencia y Tecnologia CONACyT with grant number 210965 and multiple proyects (240512,CB-2009-01,#132400) and the Dirección General de Asuntos del Personal Académico from the UNAM grants(PAPIIT IN116210-3, IN111513-3), during the last months of my PhD. I gratefully acknowledge this support.

Contents

List of Figures

Resumen

§0.1 Resumen

Los jets astrofísicos relativistas son flujos colimados con velocidades muy cercanas a la de la luz, cuyos factores de Lorentz van desde uno hasta 500. Estos jets astrofsicos representan los objetos individuales mas energéticos del universo, despidiendo una energa tan alta como $10^{36} - 10^{40}$ joules por segundo en un tiempo de vida de 10^8 años, a estos jets se les asocia agujeros negros super masivos con masas $\sim 10^8 M_\odot$ en blazares, y una energía de 10^{44} joules por segundo despedida en unos cuantos segundos para el caso de jets asociados e destellos de rayos gamma, producidos por agujeros negros de masa $\sim 10 M_\odot$. Además los jets relativistas manifiestan el mismo fenómeno a diferentes escalas destacando una relación de escalamiento entre ellos y revelando la física fundamental en el proceso de eyección de jets.

Uno de los objetos más impresionantes del universo en términos de energía son los flujos bipolares emitidos desde objetos compactos conocidos como jets relativistas. Los jets son flujos de materia colimada a velocidades supersónicas, conducidos a lo largo de un eje que parte de un motor central o maquinaria central que impulsa los jets, dicho motor es asociado a estrellas jóvenes, estrellas de neutrones o agujeros negros de masas estelares o supermasivos.

Comúnmente alrededor del motor central se encuentra un disco de acreción, alimentando de material la parte central, eventualmente el motor central concentra y conduce el material a través de un canal que será eyectado en el jet. Si el motor central es un objeto gravitacionalmente relativista como un agujero negro o una estrella de neutrones el material dentro del jet alcanzara velocidades ultrarelativistas con factores de Lorentz altos.

En términos generales los jets son clasificados de acuerdo a la naturaleza de su motor central:

- Objetos Estelares Jóvenes. Estos jets tienen longitudes de $0.01 - 1$ pc, y velocidades típicas de $v \sim 100 - 400\text{Kms}^{-1}$. El motor central corresponde a una estrella recién nacida de $1M_{\odot}$. La tasa de eyección de masa de estos jets estelares es de $\dot{M} \sim 10^{-9} - 10^{-6}M_{\odot}/\text{yr}$.

- Jets Extragalácticos. Asociados a galaxias, estos son las estructuras coherentes mas largas del universo, que en general, se observan en galaxias activas, es decir, galaxias que albergan una región compacta en el centro de la galaxia con una luminosidad mucho mayor en todo el espectro electromagnético que una galaxia normal. Esta región es conocida como un núcleo activo de galaxia (NAG) y algunos de ellos presentan líneas de emisión en esta región. Entre la familia de los NAGs los jets más extendidos son albergados en las radio galaxias y cuásares y los más poderosos están en los blazares o cuásares de espectro radio plano. Los jets extraglacticos tienen longitudes típicas de $0.01 - 1$ Mpc. La velocidad promedio del plasma en el jet presenta altos valores del factor de Lorentz del orden $\sim 2 - 50$. Estos son impulsados por un agujero negro supermasivo de una masa alrededor de $M_{BH} \sim 10^6 - 10^9 M_{\odot}$.

- Micro-cuásares. Estos jets se presentan en sistemas de binarias de rayos X, compuestos por una estrella masiva de $8 - 20M_{\odot}$ enlazada gravitacionalmente a un agujero negro de $\sim 1 - 10M_{\odot}$. La estrella masiva provee el material que formara el disco de acreción alrededor del agujero negro. En algunos de estos sistemas el material es eyectado a velocidades relativistas con factores de Lorentz de $2 - 8$ con una longitud de $1 - 100$ pc. Debido a su similitud morfológica con cuásares, estos sistemas pueden ser pensados como una versión escalada de los mismos.

- Destellos de Rayos Gamma. Estos corresponden a los destellos más energéticos en el universo. Debido a la alta emisión de energía en rayos gamma que estos objetos presentan, se presume que estos jets son flujos colimados de plasma moviéndose a factores de Lorentz de $100-500$, impulsados por un agujero negro de masa $\sim 1-2M_{\odot}$, y eyecta de una a media masa solar durante el destello. La duración del destello oscila entre $1 - 10$ segundos para los destellos largos. La longitud estimada para estos jets esta alrededor de $0.01 - 100R_{\odot}$.

Los últimos tres jet son relativistas debido a los altos factores de Lorentz del flujo promedio, producidos por agujeros negros estelares o supermasivos como motor central.

La característica principal de los jets son el flujo colimado transportando materia y energía magnética al medio interstelar o intergaláctico.

Entre las características que comparten los jets astrofísicos relativistas se encuentran el transporte colimado de masa y plasma llevando momento, energía y flujo magnético a su medio circundante desde escalas galácticas hasta extragalácticas. Algunas de las características comprenden un gran rango de luminosidades $(10^{53} - 10^{3})$ $L_{\odot}$ con un pequeño grado de colimación. El fenómeno de jets es observado desde los nucleos activos de galaxias hasta los jets asociados a objetos estelares jóvenes en nuestra galaxia. En la escala intermedia entre estos dos extremos, uno encuentra evidencia de flujos asociados a estrellas de neutrones, sistemas masivos de binarios de rayos X, estrellas simbióticas y agujeros negros galácticos de masa estelar (micro cuásares).

Tambien esta asociado al fenómeno de jets los destellos de rayos gamma, descubiertos en 1967 y descritos como las explosiones mas brillantes en el universo. Estos objetos se localizan a distancias cosmológicas con rangos de luminosidad desde $10^{42} - 10^{47}$J/s, emitiendo radiación sincrotrón desde los jets relativistas. Los destellos de rayos gamma largos están asociados con super novas de estrellas Wolf-Rayet.

La mayoría de estos flujos a pesar de sus diferencias físicas de escala y potencia, son morfológicamente muy similares, sugiriendo un origen físico común. En un extremo los jets de NAGs tienen tamaños típicos de $\gtrsim 10^{6}$ pc, factores de Lorentz del jet $\sim 10 - 100$, y cuyos motores centrales son agujeros negros con masas $\sim 10^{6} - 10^{9}$ $M_{\odot}$ y luminosidades $\sim 10^{43} - 10^{48}$ $L_{\odot}$. En contraste los jets de objetos estelares jóvenes tienen tamaños típicos ~ 1 pc, factores de Lorentz del jet ~ 1, y emergen de protoestrellas de baja masa ~ 1 $M_{\odot}$ con luminosidades de $0.1 - 2 \times 10^{4}$ $L_{\odot}$ por lo tanto el fenómeno de jets visto en escala física cubre mas de siete ordenes de magnitud en la masa del motor central, aun asi, todos estos jets comparten las mismas características que en general son:

- Flujos altamente colimados y en la mayoría de los casos bipolares, originados en sistemas gravitacional mente acoplados tales como estrellas de reciente formación o estrellas de neutrones o sistemas de agujeros negros.

- Muestran una serie de acumulaciones, mas o menos, regularmente espaciadas en emisión de nudos en la cual la mayoría de los casos presentan movimientos super lumínicos alejándose de la fuente central, mostrando su naturaleza relativista.

- Esta asociados campos magneticos cuya dirección de proyección se infiere de medidas

de polarización.

- Muestran evidencia de acreción de materia en la fuente central por un disco de acreción con actividad variable en algunos casos.

Los jets extragalácticos son el mejor ejemplo de eyecciones relativistas emergiendo desde el centro de núcleos activos de galaxia y extendiéndose a distancia de algunos megaparsec en el medio intergaláctico. Algunos de sus parámetros básicos como la velocidad del jet, el numero de Mach o el cociente de la densidad del jet a la densidad del ambiente, pueden ser directamente restringidos por observaciones, estos parámetros son empleados en modelos fsico-matemáticos de jets.

El desarrollo de modelos analíticos y semi-analíticos para jets astrofísicos relativistas, nos permiten el estudio de las condiciones del jet con simples aproximaciones para entender el rol fundamental que juega la física de choques en los procesos de emisión y la emisión de su curva de luz, logrando obtener en algunos modelos parámetros fsicos del fenmeno.

El fenómeno de ondas de choque moviéndose dentro de jets astrofísico es descrito por Mendoza et al. (2009) como variaciones periódicas de la velocidad o inyección de masa en la base del jet, estás variaciones producen eyecciones de fluido dentro del jet, de tal manera que fluido rápido alcanza a fluido lento previamente eyectado, produciendo una discontinuidad inicial sobre las cantidades hidrodinámicas llevando a la formación de una superficie de trabajo, es decir dos ondas de choque separadas por una discontinuidad de contacto. La superficie de trabajo representa la región de emisión de los nudos dentro del jet relativista. El motor central eyecta el material en la base del jet en una dirección preferencial tal que la superficie de trabajo es descrita como una colisión de dos parcelas de fluido a lo largo del jet.

El modelo de Mendoza et al. (2009) considera que las escalas de tiempo radiativo son pequeñas comparadas con el tiempo dinámico característico del jet, permitiendo una descripción balística del problema con una solución semi-analítica. Bajo la consideración que la superficie de trabajo es delgada y que esta no pierde masa con ella, la energía perdida dentro de la superficie de trabajo puede ser calculada como la diferencia entre la energía total inyectada en la base del jet y la energía del flujo dentro de la superficie de trabajo. Considerando un mecanismo eficiente que convierte toda la energía cinética perdida en radiación, la luminosidad puede ser calculada como la derivada temporal de esta energía radiada. Esta luminosidad es función de la velocidad y la tasa de inyección de masa del fluido, con la simple consideración de hacer que las variables del fluido son inyectadas de

manera periódica, forzando naturalmente al fluido a producir una superficie de trabajo que se mueve a lo largo del jet. El modelo original de Mendoza et.al. (2009) fue construido para reproducir las curvas de luz asociadas a destellos de rayos gamma largos.

En esta tesis se uso el modelo de Mendoza et al. (2009) para explicar las curvas de luz multi-frecuencia asociadas a diferentes objetos astrofísicos: blazares, microcuásares y cuásares, para hacer esto el modelo es usado en la forma mas general y los ajustes a las diferentes fuentes fueron implementados usando diversas herramientas estadísticas variando desde un simple método χ^2 a algoritmos genéticos. Los jet astrofísicos modelados son:

(a) La curva de luz multi-frecuencia del nudo HST-1 dentro del jet de la galaxia M87. Extendidas observaciones en tiempo del nudo han producido detalladas curvas de luz en rayos-X, ultravioleta y bandas de radio. La emisión del nudo desarrolla un máximo de intensidad en 2005 y todas las longitudes de onda muestran dos claros estallidos en la luminosidad. Para modelar la curva de luz asociada al nudo HST-1 se usaron variaciones periódicas en la velocidad del flujo inyectado y la tasa de inyección de masa en la base del jet. Los ajustes de los parámetros del modelo a los datos observacionales fueron realizados usando un algoritmo genético y los resultados fueron obtenidos con un nivel de confianza estadístico mayor a $2-\sigma$.

La mejor estimación de parámetros dio una tasa máxima de eyección en la base del jet $\dot{m} \sim 10^{-2} M_{\odot}/\mathrm{yr}$ y un máximo en el factor de Lorentz de ~ 30, ambos corresponden al máximo de la curva de luz en 2005.

(b) El microcuásar A06200-00, muestra un impresionante estallido de 1975 a 1976 produciendo una muy detallada curva de luz en rayos X mostrando un estallido principal seguido por uno menor. El modelo describe exitosamente la fuente usando dos diferentes escenarios el primero considera la superposición de dos destellos producidos por variaciones periódicas en el flujo de la velocidad inyectada. El segundo tiene una variación periódica adicional en la tasa de eyección de masa. Los ajustes a los datos observacionales fueron realizados con un análisis de regresión lineal, contando con una presión del 10 %.

Ambos escenarios dan una tasa de eyección de masa $\dot{m} \sim 10^{-11} - 10^{-12} M_{\odot}/\mathrm{yr}^{-1}$ de acuerdo a modelos previos del micro cuasar A06200-00 con un factor de Lorentz $2.3 - 3.6$.

(c) El blazar PKS 1510-089 observado en rayos gamma del 2008 al 2011 exhibe tres promin-

entes estallidos en los años 2008 , 2009 y 2011, el último muestra un tremendo estallido durando al menos una semana y poniendo la fuente en la posición espectacular de ser el objeto mas luminoso en rayos gamma observado en el cielo. La alta actividad en rayos gamma y observaciones detallada de esta fuente, la convierte en un excelente candidato para ser modelada usando la propuesta de Mendoza et al. (2009).

Los ajustes a la curva de luz se realizaron usando variación periódica a la velocidad del jet para cada estallido detectado en PKS 1510-089, usando una prueba estadística χ^2 e infiriendo factores de Lorentz $\Gamma \sim 10 - 380$ y tasas de inyección de masa $\dot{m} \sim 2 - 25 \times 10^{-3} M_{\odot}\mathrm{yr}^{-1}$, tales factores de Lorentz tan altos nunca habían sido inferidos en un blazar, esta fuente puede ser pensada como un escalamiento de un destello de rayos gamma largo.

Finalmente se presentan los primeros pasos de un nuevo modelo totalmente hidrodinámico no relativista para la superficie de trabajo con una solución analítica, sin al necesidad de la aproximación tradicional de capa delgada, este modelo toma en cuenta todas las variables hidrodinámicas del jet para calcular la luminosidad de la curva de luz. El modelo fue aplicado para ajustar la curva de luz asociada al jet de la galaxia 3C120.

El modelo de Mendoza et al. (2009) puede ser aplicado exitosamente a diferentes objetos específicos que contengan jets tales como destellos de rayos gamma largos, cuásares, blazares y micro-cuasares, mostrando que una posible relación de escala debe de existir para todos ellos asemejado el fenómeno físico de la generación de ondas de choque internas. Aunque el modelo original de Mendoza et al. (2009) aproxime el jet con una descripción balística, se presenta un nuevo enfoque de la solución de una superficie de trabajo para jets no relativistas. En el futuro se desarrollara un modelo que tenga la parte relativista con aplicaciones útiles a ondas de choque internas dentro de jets altamente energéticos asociados a destellos de rayos gamma largos, cuásares, blazares y microcuásares.

Abstract

All the astrophysical objects that involve an accretion process to a stellar or super massive black hole produce powerful relativistic jets generically known as, μ-quasars, quasars and gamma ray bursts. All these share the same phenomenology, suggesting a scaling law for the physical phenomena associated to them.

For the case of active galactic nuclei, the presence of knots in astrophysical jets are commonly interpreted as shock waves moving along its jet. These knots show in many cases apparent superluminical motions. Observation of these knots during extended periods of time have produced precise light curves. In particular, the well studied radio knot HST-1 in the galaxy M87 has produced light curves on many wavelengths that are difficult to reproduce due to its complicated morphology.

Using a semi-analytical approach, developed by Mendoza et al. (2009), which can reproduce light curves of working surfaces moving along any relativistic jet, we have fitted complicated light curves of different astrophysical objects in particular the ones associated to the of HST-1 knot. These high accuracy fits were performed in multi wavelengths on many of the studied objects.

Using this model we are also able to reproduce the observation of the light curve of the micro-quasar A06200-00 with high accuracy and the long time blazar PKS 1510-089 observations in gamma-rays.

Finally, we develop an analytical model in the non-relativistic regime for a working surface without the thin layer approximation. This model reproduces successfully the light curve of radio galaxy 3C120 and opening a new understanding in the hydrodynamics processes of internal shock wave formation and evolution inside the jets.

Chapter 1

Introduction

Relativistic astrophysical jets are collimated flows a with high Lorentz factor from a few units up to 500. These astrophysical jets represent the single most energetic objects in the universe, releasing energies up to $10^{36} - 10^{40}$ joules per second in 10^8 years for the case of jets associated to $\sim 10^8 M_\odot$ supermassive black holes in blazars and 10^{44} joules per second in up to a few seconds for the case of jets associated to long gamma ray bursts produced by a $\sim 10 M_\odot$ stellar black hole. Additionally, the relativistic jets manifest the same phenomena at different scales, leading a scale relation between them, reveal a fundamental physics of jet outflows.

§1.1 History of jets, accretion flows and outflows

One of the most impressive objects in the Universe in terms of energy are the bipolar outflows emitted from compact objects known as relativistic jets. Jets are streams of collimated supersonic matter driven along the axis from a central engine associated to a young star, a neutron star, a stellar black hole or a super massive black hole.

An accretion disc surrounding the central engine feeds and channels matter into it which is later ejected by the jet. If the central engine is a relativistic gravitational object such as a black hole or a neutron star, the bulk jet velocities are able to reach ultrarelativistic speeds with large Lorentz factors.

In general terms, the jets are classified depending on the nature of their central engine:

- Young Stellar Objects. These jets have lengths of $0.01 - 1$ pc, and typical velocities

of $v \sim 100 - 400\text{Kms}^{-1}$. The central engine corresponds to a new born star of $1M_{\odot}$. The mass ejection rate produced by these stellar jets is $\dot{M} \sim 10^{-9} - 10^{-6} M_{\odot}/\text{yr}$.

- Extragalactic jets. Associated to galaxies, these are the largest coherent structures, which are, in general, seen in active galaxies, i.e. galaxies hosting a compact region at the center of the galaxy with a higher luminosity over all the electromagnetic spectrum than a normal galaxy. This region is know as Active Galaxy Nuclei (AGN) and some of them present emission lines in this region. Among the family of AGNs the largest jets are hosted in radio galaxies and quasars and the most powerful are in the Blazars or Flat Spectrum Radio Quasars (FSRQ). The extragalactic jets have a typical length of $0.01 - 1$ Mpc. The velocity bulk of the plasma jet presents high Lorentz factors in the order of $\sim 2 - 50$. These are powered by a super-massive black hole of mass around $M_{BH} \sim 10^6 - 10^9 M_{\odot}$.

- Micro-quasar. These jets are present in X-ray binary systems, composed of a massive star of $8 - 20M_{\odot}$ gravitationally bound to black holes of $\sim 1 - 10M_{\odot}$. The massive star provides the material that constitutes the accretion disk around the black hole. In some of these systems the material is ejected at relativistic speeds with Lorentz factors of $2 - 8$ with a length of $1 - 100$ pc. Due to their morphological similarities with quasars, these systems can be thought of as a scaled version of them.

- Gamma Ray Burst. These correspond to the most energetic bursts in the Universe. Due to the high energy emission in gamma-rays these objects present, it is presumed that they are a collimated outflow of plasma moving at Lorentz factors of $100 - 500$. They are powered by a black hole of mass $\sim 1 - 2M_{\odot}$, and eject one or a half solar masses during the burst. The duration of the burst ranges from $1 - 10$ seconds for long bursts. The estimated length of the jets is around $0.01 - 100R_{\odot}$.

The last three jets are named as relativistic jets due to the high Lorentz factor of the bulk flow, produced by stellar or supermassive black hole object as central engine. The principal characteristic of jets are the collimated flow, transporting matter and magnetic energy to the interstellar or intergalactic media.

The first observation of an extragalactic jet corresponds to the galaxy M87 (NGC 4486, Virgo A, Arp 152 or 3C 274) and was carried out by Curtis (1918) reveal a “curious straight jet ... apparently connected with the nucleus by a thin line of matter”. These

optical observations were not followed by Curtis until the development of radio astronomy and the theory related to the emission process of the astronomical sources in the 1960's.

The first radio observations of Jansky (1933) and Reber (1944) were concentrated in the studies of diffuse galactic radio emission, resulting in a common radiation process to a non-thermal process such as radio Bremsstrahlung, but it was difficult to determine the process due to diffuse emission and the sensitivity of the radio telescopes.

In search for the determination of radio emission process, Alfvén & Herlofson (1950) were the first to propose that the galactic radio emission might be synchrotron radiation of energetic electrons gyrating in magnetic fields in the atmosphere of stars. A key test of the synchrotron hypothesis was the search for polarised radio emission from the diffuse interstellar medium, and this was observed by Razin (1958) and by Westerhout et al. (1962) at Dwingloo in the Netherlands. The synchrotron theory was finally accepted as a mechanism to produce the diffuse galactic radio emission.

Even more remarkably, the radio source Cygnus A was identified with a galaxy at a redshift of 0.057, implying that a radio luminosity of 5.0×10^{37}W between 10MHz and 400GHz (Baars et al., 1977), more than one million times grater than that of our Galaxy in radio. It must therefore be the source of vast quantities of relativistic material. The fact that the radio emission did not originate from the galaxy itself, was just as unexpected. Jennison & Das Gupta (1953), at Jodrell Bank used interferometric techniques to show that the radio emission originated from two huge lobes. Once the identification was made in the following year, it turned out that these lobes were located on opposite sides of the radio galaxy (Baade & Minkowski, 1954). Thus, not only must the radio galaxy accelerate an enormous amount of material to relativistic energies, but this material also has to be ejected to the intergalactic space in opposite directions.

During the late 1960s and early 1970s, the first high resolution radio maps were taken of extragalactic radio sources with the new generation of Earth-rotation aperture synthesis radio telescopes and these began to reveal the details of the structure of these sources. The culmination of these studies were high quality maps, such as the one of Cygnus A (see Figure 1.1) made with the Very Large Array in New Mexico. Fanaroff and Riley noticed that the morphologies of these radio structures depended very strongly on their radio luminosities. In powerful double radio sources such as Cygnus A, the maximum radio surface brightness of the lobed structures is observed in *hot-spots* towards the outer ends of the diffuse radio lobes and these are referred to as *Fanaroff-Riley Class* 2 (FR-II) radio sources with luminosities $\mathrm{L} \gtrsim 10^{24}\mathrm{WHz}^{-1}\mathrm{sr}^{-1}$. In contrast, those sources in which the

maximum surface brightness occurs less than halfway from the active galactic nucleus to the edge of the diffuse radio lobe structure, the *Fanaroff-Riley Class* 1 (FR-I) sources with luminosities $L \lesssim 10^{24}\mathrm{WHz}^{-1}\mathrm{sr}^{-1}$, have radio luminosities which are lower than those of Class 2. The distinction between the two classes occurs rather abruptly at well defined radio luminosities.

Moreover, the morphology classification for radio source reveals for *Fanaroff-Riley Class* 2 that the core and jets are also brighter than the FR-I class radio galaxies, but fainter respect to the lobes. The jet structure is only detected in > 10 percent of radio galaxies. The jets have an small opening angle and are knotty. Most of the jets of the FR-II class are a one-sided beam lobe often jet is hidden due to relativistic beaming effects, at Kpc scale and the host galaxy correspond to a Gigant elliptic.

The FR-I radio galaxies presents a low bright central region that diminish away from the central galaxy. The jet detection spans over 80 percent for these galaxies. Most of the FR-I galaxies start as one-sided close to the core and beyond the Kpc scale present a two-sided continuous beam, with an opening angle of $\leqslant 8\,\mathrm{deg}$ with variation along the jet. These sources are associated to large radio galaxies with a radio structure distorted through ram pressure of the external medium.

The formation of the lobes was explained with plasma confinement and the expansion of such material is attributed to ram pressure exerted on the intergalactic medium (De Young, 1967). The mechanism driving these powerful lobes is the production of bipolar flows, described first by Longair et al. (1973) who proposed that beams are made of hot, magnetised gas. Later, Blandford & Rees (1978, 1974) and Scheuer (1974) assumed a relativistic beam of strong electromagnetic waves of fast particles without magnetic fields, known as the "*twin exhaust model*".

§1.2 Active Galactic Nuclei

Astronomical observations of extragalactic objects in the 1950's and 1960's, began to show unusual signs of activity in galaxies. These galaxies had a blue intense emission and a peculiar spectrum that do not correspond to stellar or gas integrated emission of a galaxy. The spectrum had intense lines of emission toward the high energies and a continuum emission hotter than most massive stars. Some of these sources presented noticeable variability of the order of days in time associated to their host galaxy. These objects made a new classification of galaxies with a central source know today as Active Galactic Nuclei

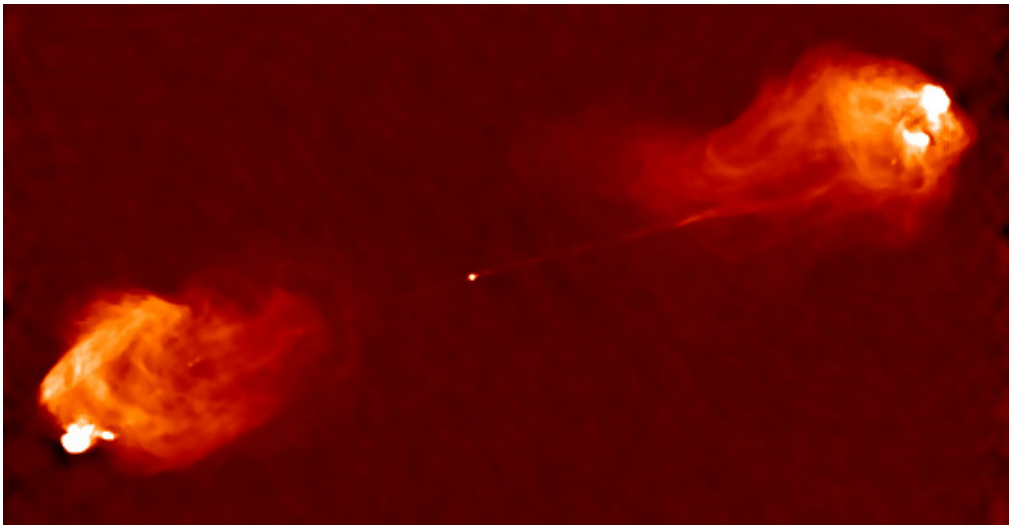

Figure 1.1: An image of the radio galaxy Cygnus A (3C 405) shows the jet and radio lobes. The image was taken by the Very Large Array in New Mexico at a frequency of 5GHz. The radio lobes or "hot spots" are the bright spots where its the interaction between the jet and the interstellar or intergalactic medium occurs (Perley et al., 1984). The source extends about 150 Kpc end to end. In contrast, when the galaxy is observed in optical wavelengths its size is less than a tenth of its radio length.

(AGN). Today we know that the central engine that powers the emission is a super massive black hole in the nuclei of the host galaxy showing evidence of accretion and providing a luminosity of 10^{33} W to 10^{40} W.

Later observations made in the next decades together with the high accurate position of radio sources, revealed that some of the active galaxies present an intense radio emission due to collimated, supersonic jets of gas. The observations of jets were also useful to accurately find the location of the optical host galaxy of the source. One of these first associations was made for the object 3C273, revealing a high redshift of 0.158 (Schmidt, 1963) and exposing the origin of extragalactic jets at the center of active galaxies.

The most basic classification of AGN is made by dividing them in two radio families according to their radio properties; (a) radio-loud, with radio luminosities $L \gtrsim 10^{24}\mathrm{WHz}^{-1}\mathrm{sr}^{-1}$, and (b) radio-quiet, for which $L \lesssim 10^{24}\mathrm{WHz}^{-1}\mathrm{sr}^{-1}$. Only about 10 % of the AGN are radio-loud, the rest are radio-quiet.

The refinement of radio observations with the VLBI, display impressive radio images of radio-load AGN jets showing blobs or knots where are bright structures of "agglomeration" within the jet moving outward from the core. In many cases the proper motion of these knots in the line of the sky present apparent superluminal motions, i.e. structures that in the plane of the sky present apparent speeds greater than the speed of light. These phenomena were predicted by Rees (1966),and show that "an object moving relativistically in suitable directions may appear to move in the plane of the sky with a transverse velocity much greater than the velocity of light". This interpretation, was successful explain the radio images and the speeds of the knots inside the jet. On the other hand, the one sidedness observed in radio loud sources was explained with relativistic beaming effects due to the fact that the radio galaxy lies not completely in the plane of the sky, diminishing with this the detection of the jet particles moving and pointing away from us.

The study of the knotty structure in relativistic and non-relativistic jets have opened up new ways to understand their multifrequency observations. Rees (1978) suggested that the optical knots observed in the jet of the galaxy M87 can be interpreted by periodic bulk speed variations in the beam producing internal shock waves in the jet. This was tested in numerical hydrodynamical simulations by Norman et al. (1982), exploring the morphology of jets over a large range of parameters for different Mach numbers, temperature ratios and hydrodynamical instabilities such as the Kelvin-Helmholtz instabilities all for the jet working surface and the cocoon, in the context of an ideal gas moving at non-relativistic velocities.

Later models (Birkinshaw, 1984; Cielo et al., 2014; Keppens et al., 2013; Walg et al., 2013) were done in the relativistic regime and effectively show the same trends as the non-relativistic description: periodic variations on the bulk flow velocities developed shocks identified with shock waves that moved along the jet with ultrarelativistic velocities.

The internal shock model has been successfully applied in other sources. For example, micro-quasars (Kaiser et al., 2000) and Gamma Ray Burst (Rees & Meszaros, 1994; Piran, 2004), showing the efficient conversion factor of kinetic energy to luminosity.

§1.3 Jets at all scales

A variety of astrophysical objects present highly collimated supersonic jets, emerging from compact objects such as galactic black holes, X-ray binary systems and in the nuclei of active galaxies (AGNs). Despite their different physical scales in size, velocity, magnetic field and the amount of energy transported, they have strong similarities.

Astrophysical jets are channels carry on mass, momentum, energy and magnetic flux, transporting plasma and mass from galactic and extragalactic objects to the surrounding medium. The base of the jets are narrow (a small opening angle) conical or cylindrical/semi cylindrical geometry (Das, 1999), and represent ubiquitous phenomenon in the universe. Some of their characteristics cover a large range of luminosities $(10^{53} - 10^{3})$ $L_{\odot}$ with a few degrees of collimation. The jet phenomena are observed from the nuclei of active galaxies to the jets associated to low-mass young stellar objects (YSOs) with our own galaxy. In the intermediate scale, between these two extremes, one finds evidence of outflows associated to neutron stars, massive X-ray binary systems, symbiotic stars, and galactic stellar mass black holes (or microquasars).

Also associated to jet phenomena are the long gamma ray bursts (GRBs). Since their discovery in 1967 they have been described as the brightest explosions in the universe apart from the Big Bang itself. These objects are located at cosmological distances with luminosities ranging from $10^{42} - 10^{47}$J/s, emitted from relativistic jets via synchrotron emission. Long GRBs bursts are to be associated with supernovae of massive Wolf-Rayet stars (Mészáros, 2002) *.

*The classification for GRBs comes from the duration of the bursts in a bimodal distribution:bursts which last lees than two seconds are being termed short and those of greater duration are long. For the case of short GRBs their luminosities range from $10^{43} - 10^{44}$J/s, and are associated with the merger of compact objects.

As largely stressed in the literature (Mirabel & Rodríguez, 1998; Sams et al., 1996; Rees, 1998; Castro-Tirado et al., 1999; Maccarone et al., 2006; Fender et al., 2005; Fender & Gallo, 2014), most of these outflows, despite their different physical scales and power, are morphologically very similar, suggesting a common physical origin. In one extreme, AGN jets have typical sizes $\gtrsim 10^6$ pc, jet Lorentz factors $\sim 10 - 100$, and central engines which are massive black holes with masses $\sim 10^6 - 10^9$ $M_\odot$ and luminosities $\sim 10^{43} - 10^{48}$ $L_\odot$. In contrast, YSO jets have typical sizes ~ 1 pc, jet Lorentz factors ~ 1 , and emerge from low mass protostars with masses ~ 1 $M_\odot$ with luminosities of $0.1 - 2 \times 10^4$ $L_\odot$. Therefore, the jet phenomenon is seen on physical scales that cover more than seven orders of magnitude in central engine mass. Nonetheless, all the jet classes share common properties. In general, they

- are highly collimated outflows and in most cases two sided,
- originate from sufficiently well gravitationally bound systems such as a recently born star or a compact neutron or black hole system,
- show a series of blobs, more or less, regularly spaced emission knots which in some cases move at apparent superluminal velocities away from the central source, showing its relativistic nature (Mirabel & Rodríguez, 1998),
- are associated with magnetic fields whose projected directions are inferred from polarization measurements,
- show evidence of accretion of matter onto the central source via an accretion disk, with variable activity in some cases.

Extragalactic jets are the best example of relativistic ejection observed to be emerging from the nuclei of active galaxies, and may extend for distances of a few mega-parsecs into the intergalactic medium. Some of them are considered to be the largest single coherent structures found in the Universe. None of the basic parameters, like the jet velocity, the Mach number, or the jet to the ambient density ratio can be directly constrained by observations and so, a physical mathematical model is required to get these parameters.

The first relativistic jets were discovered in the nuclei of galaxies and distant quasars, and although the distance to these galaxies are of the order of mega parsecs, the jets seem to be absent in our Galaxy with the exception of the object SS443, the only object

presenting relativistic jets for more than two decades (Margon, 1984). The reason for this paradox is that the accretion disks about supermassive black holes emit at optical and UV wavelengths. For a black hole accreting at the Eddington limit, the characteristic black body temperature at the last stable orbit in the surrounding accretion disk will be given approximately by $T \sim 2 \times 10^7 (\mathrm{M}/\mathrm{M}_\odot)^{1/4}\mathrm{K}$ (Rees, 1984; Kolykhalov & Sunyaev, 1984), where M is the black hole mass. Indeed, exist an inverse relation between the mass of the black hole and the temperature of the surrounding accretion disk. Therefore, while accretion disks in AGNs have strong emission in the optical and ultraviolet with distinct broad emission lines, black holes and neutron star binaries usually are identified by their X-ray emission. These X-ray sources were only found as the techniques of X-rays astronomy improved.

With the development of the X-ray astronomy and the use of multi-frequency observations in the range of the hard X-rays on the one hand (Sunyaev et al., 1991), and in the range of radio wavelengths on the other, revealed the existence of new binary stellar systems sources of relativistic jets known as microquasars (Mirabel & Rodríguez, 1998). Microquasar or relativistic jets from stellar-mass black holes in binary stars emitting X-rays (also denominated BHXRTs), are scaled-down versions of quasar jets, typically extending for ~ 1 pc and most probably powered by spinning black holes with masses of $\lesssim 10\mathrm{M}_\odot$. These are X-ray binary systems in our galaxy, combine two relevant fields of relativistic astrophysics: accretion of matter on to black holes of stellar origin identified by the production of hard X-rays and gamma-rays from surrounding accretion disks, and relativistic jets of particles observed by means of their synchrotron emission

Microquasar or relativistic jets from stellar-mass black holes in binary stars emitting X-rays (also denominated BHXRTs), are scaled-down versions of quasar jets, typically extending for ~ 1 pc and most probably powered by spinning black holes with masses of $\lesssim 10\mathrm{M}_\odot$. Despite the enormous difference in scale, both classes share a lot of similarities in their physical properties. As seen from figure 1.2, they are both believed to be surrounded by an accretion disk and since the characteristic times in the flow of matter onto the black hole are proportional to its mass (Rees, 1998), the accretion-ejection phenomena in microquasars is expected to last much shorter time of the order of $10^{-7} - 10^{-5}$ times of their quasar counterpart.

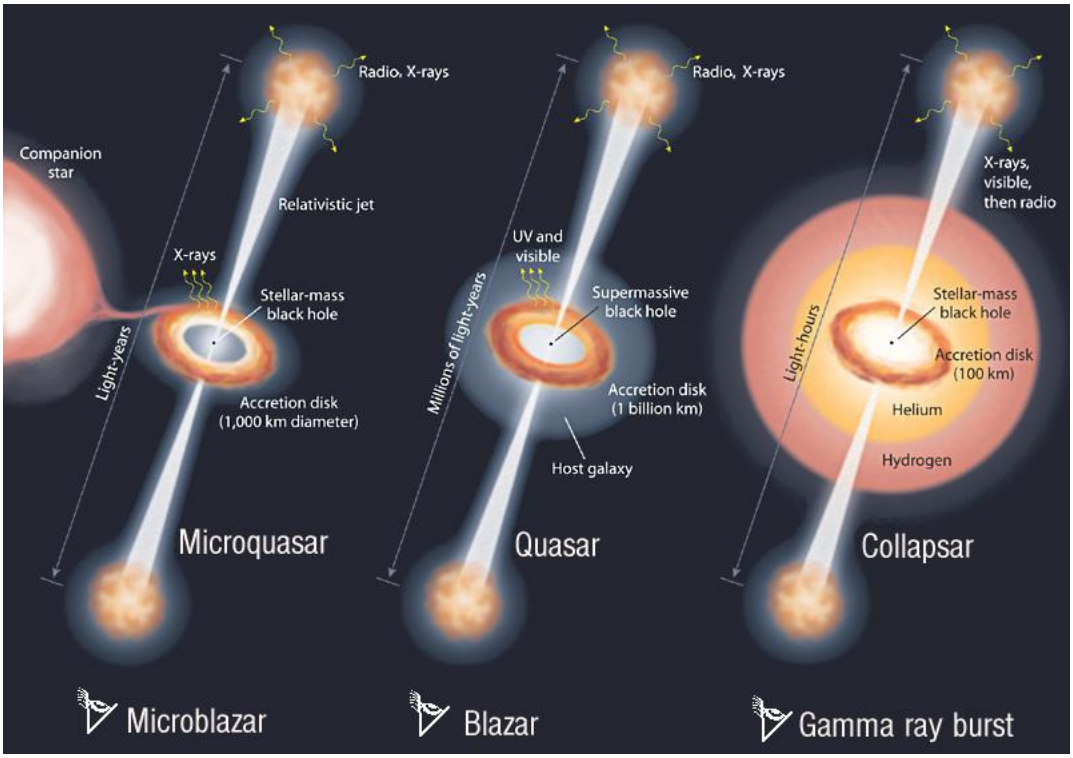

Figure 1.2: The figure shows the morphological similarities that the accretion-ejection mechanism presents for three different classes of relativistic objects, μ-quasars, quasars and long GRB's (not to scale). Note that the fundamental emission of the accretion disk depends on the mass of the black hole. As the mass of the black hole increases, the energy of the main disk emission decreases. All the jets have relativistic jet bulk velocities and they all share terminal shocks, or lobes in the case of AGNs. The orientation effect proposed for the AGNs is extended for jets in stellar black holes. Finally, the length of the jet differs in more than seven orders of magnitude but the same phenomena is preserved, indicating that these three areas should help to understand the universal mechanism of relativistic jet phenomena observed everywhere in the universe. Figure credit: Mirabel & Rodriguez, Sky & Telescope, 2002.

§1.4 Scaling relations in black holes and jets

For the case of quasars and microquasars, scaling relations are fundamental to understand the physical background in the production of jet outflows in black holes. Both quasars and microquasars present the basic ingredients of the jet-disk coupling phenomena in black holes: a supermassive or stellar black hole, an accretion disk about it and a collimated jet of high-energy particles.

Simple scaling of the laws that govern the physics of astrophysical flows around black holes allows for the description in terms of dimensionless parameters. The dimensionless ratio $r/r_{\rm g}$ where $r_{\rm g} = {\rm GM/c^2}$ is the gravitational radius, where M is the mass of the gravitational object and r is the distance to the gravitational radius, represents an important parameter for the description of the problem according to Buckingham's theorem of dimensional analysis (Buckingham, 1915). The same also happens for the orbital time scales of particles around the black hole since this time is proportional to the mass of the black hole and the ratio thus indicates that a stellar mass black hole has a lower time scale with more variable accretion times than a super massive black hole. These relations are called *scaling laws for black holes* and it is important to note that the scale depends on the mass of the black hole (Sams et al., 1996; Rees, 1998). It can be shown that the accretion disk density and average temperature associated to the disk are proportional to M^{-1} and $M^{-1/4}$, respectively, where M is the mass of the black hole (Mendoza, 2002). Similarly, if we consider lengths, accretion rates, central masses and luminosities in terms of the Schwarzschild radius $r_s = 2GM/c^2$, solar masses $M_\odot$ and Eddington luminosities, the physical laws scale with the mass of the black hole M only.

Radio and X-ray observations from different astrophysical objects such as AGNs, μ-quasars and other accreating compact objects display a relation between the radio emission of the jet and the X-ray emission of the accretion disk (Merloni et al., 2003; Falcke et al., 2004) in a range seven orders of magnitude in the mass of the black holes. This relation is known as *the fundamental plane of the black holes*. These observational relations could provide clues on the coupling between disk accretion and jet formation.

§1.5 Micro-quasars

In the past it was believed that the instantaneous mass accretion rate $\dot{\rm M}$ was responsible for the x-ray binary states of activity, which are: quiescence → low/hard → intermediate

$\rightarrow$ high/soft $\rightarrow$ very high (see e.g. Esin et al., 1997). However it has been recently observed that $\dot{M}$ does not determine these states. Alternative models suggest that the transitions between these states respond to changes in the disk itself Homan & Belloni (2005). This model involves a new definition based on the flux disk fraction contributing to the spectra from 2-20 KeV, considering the ratio between the spectral index of the power law and the strength of the continuous power: 'Low/Hard' as low state (LS); 'High/Soft' as hard state (Hard) and 'very high' or 'intermediate' as 'VHS/IS' state, this last one not only be one, have both type hard and soft variants.

Additional observational evidence of powerful radio-emitting outflows from some states of X-ray binary systems showed a high brightness temperature 'non-thermal' spectrum and, in some cases high degree of polarization originated in synchrotron radiation from relativistic electrons ejected by the system with large bulk velocities. This was first associated to a transient burst and transition states in microquasars, and was finally resolved by Mirabel & Rodríguez (1998) as a relativistic component displacement out of the binary system. A few years later, it was detected in the X-ray band (Corbel et al., 2002). These events typically display an optically thin radio spectrum (synchrotron) with a ($\alpha \leq -0.5$) index.

The current model which connects the accretion-jet and relativistic jet in microquasars has four phases. This model's qualitative physics is described as follows (cf. figure 1.3):

1. Sources in the low-luminosity state LS produce a steady jet with a power that correlates as $L_{jet} \propto L_x^{0.5}$ (ignoring any mass terms). This phase probably extends down to very low luminosities ('quiescence').

2. The motion in the Hardness intensity diagram (HID) for a typical outburst occurs on a vertical line. There is a peak in the LS after which the motion in the HID becomes more horizontal (to the left) and the source moves into the very high or intermediate state 'hard'VHS/IS. Despite this softening of the X-ray spectrum, the steady jet persists, with a quantitatively very similar coupling to that seen in the LS.

3. The source approaches the 'jet line'(the solid vertical line in the schematic HID) in the HID between jet-producing and jet-free states. As the boundary is approached, the jet properties change, most notably its velocity. The final, most powerful, jet has the highest Lorentz factor, causing the propagation of an internal shock through the slower-moving outflow in front of it.

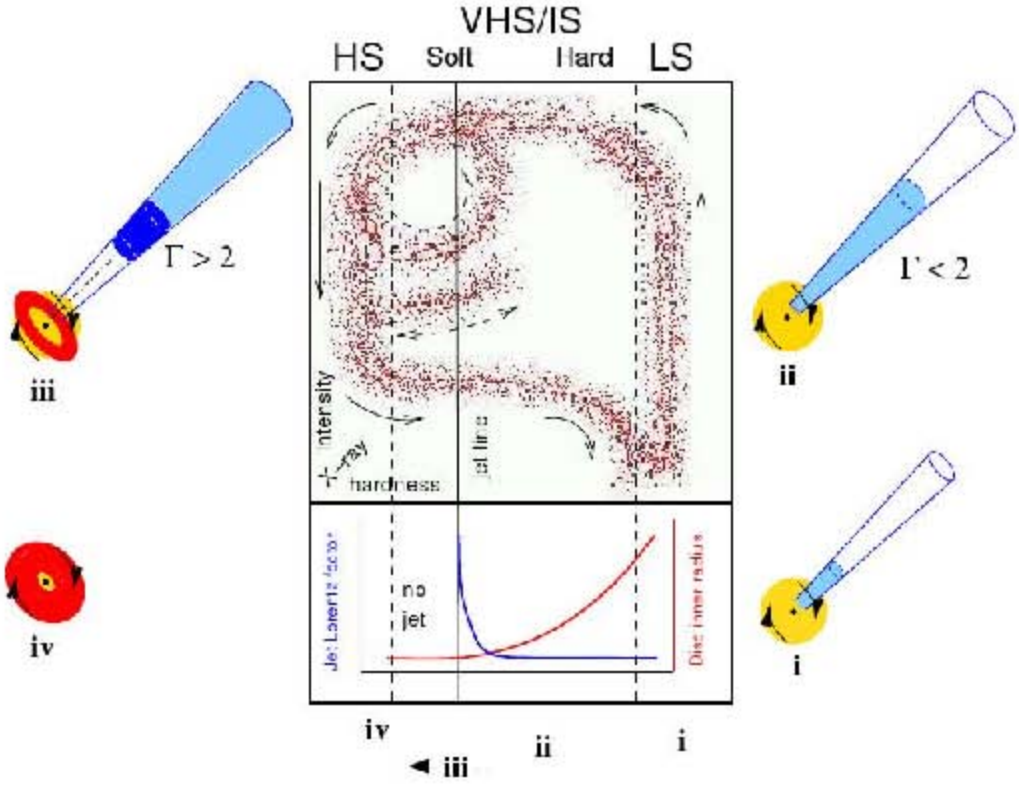

Figure 1.3: The upper central box panel represents an X-ray hardness intensity diagram (HID). 'HS' indicates the 'high/soft state' , 'VHS/IS' the 'very high/intermediate state' and 'LS' the 'low/hard state'. In this diagram, X-ray hardness increases to the right and intensity upwards. The lower panel indicates the variation of the bulk Lorentz factor of the outflow with hardness - in the LS and hard VHS/IS the jet is steady with an almost constant bulk Lorentz factor $\Gamma < 2$, progressing from state i to state ii as the luminosity increases. At some point; usually corresponding to the peak of the VHS/IS increases rapidly, producing an internal shock in the outflow (state iii) followed in general by cessation of jet production in a disc-dominated HS (state iv). At this stage fading optically thin radio emission is only associated with a jet/shock which is now physically decoupled from the central engine. As a result the solid arrows indicate the track of a simple X-ray transient outburst with a single optically thin jet production episode. The dashed loop and dotted track indicate the paths through which μ-quasars and some other transients take in repeatedly hardening and then crossing zone iii - the jet line - from left to right, producing further optically thin radio outbursts. The sketches around the outside illustrate our concept of the relative contributions of jet (blue), corona (yellow) and accretion disc (red) at these different stages. The figure was taken from Fender et al. (2004)

4. The source is in the 'soft'VHS/IS or the canonical HS and no jet is produced. For a while, following the peak in phase 3, a fading optically thin emission is observed from the optically thin shock.

§1.6 Outflows

As seen in the previous section, the fundamental interaction between the accretion disk and the ejection flow is the key to understand the jet-disk coupling. One way to explain this was via a combination between the geometry in the accretion disk around the black holes and the form of jet outflows. The strongest radio-emitting jet outows are produced in black hole systems when the accretion is a geometrically thick ($H/R \sim 1$) inow. Here H is the vertical scale and R the radius of the disc. The case where the black hole is rotating helping the jets production correspond to active galactic nuclei Meier (2001).

This type of jets presents a classification according to the disk state: 1) low/hard (ADAF, Advection Dominated Accretion Flow) or very high with a geometrically thin disk, radiation pressure dominated and unstable ows, and 2) high/soft state with an optically thick disk, favoured by the thin-disk solutions and weak jet power. These two states are clearly observed in micro-quasars, but for the case of active galactic nuclei and, in particular, for quasars, the high/soft state should not exist. This is due to the large mass of the black hole causing a dominant radiation pressure. The difference between the radio power of FRI and FRII is explained by an effect of the radio galaxy state. For example, a radio galaxy with a Kerr black hole in low/hard state corresponds to FRI or FRII without strong nuclear emission lines, and a Kerr black hole in a very high state corresponds to a quasar or FRII broad-line radio galaxy.

Additionally, the dichotomy between FRI and FRII jets seems to be due to environmental effects. An indication for this is the fact that more radio power is required to form an FRII radio jet. It seems that both jet classes are basically similar near the nucleus and that differences in the environment are able to destabilize (possibly via onset of turbulence at the boundary layer between the jet and the ambient medium) and decelerate FRI jets more effectively than FRII jets. These succeed to propagate, nearly unchanged, up to the working surface, to produce the bright lobe with hot spots without much deceleration (Bicknell, 1995; Bowman et al., 1996). Another clue that supports this interpretation of the effects in the environment was the observation of six Hybrid MOrphology Radio Sources (HYMORS) that show FRI morphology on one side of the core and FRII morphology

on the other side. This is a clear indication that the environment plays a basic role in determining the radio jet appearance at kilo- parsec scales (Gopal-Krishna & Wiita, 2000).

Chapter 2

Relativistic hydrodynamics and outflows

The description of relativistic jets, is possible with a relativistic formulation of the hydrodynamical equations, describing the conditions of a relativistic fluid in terms of density, pressure and velocity. The production of shock waves are intimately correlated to discontinuities in the fluid, leading to emission zones inside the jet. These variations are connected to oscillations the supplied material in the base of the jet.

§2.1 Introduction

There are a variety of astrophysical systems amenable to a fluid dynamical description, stars, clouds in the interstellar medium, jets, accretion discs, etc. Relativistic fluid velocities are mainly produced by strong relativistic potentials such as the ones generated by neutron stars and black holes.

The description of a system as a fluid is based on the concept of a fluid element, i.e. a sufficiently small region over which we can define local thermodynamical variables, such as the entropy, temperature, density etc. The size of the region is assumed to be such that:

The region size l_r is much smaller than a characteristic length scale over which changes of any relevant variable are negligible. In other words we can ignore systematic variations Δq for any variable q across this fluid element and so:

$$l_r \ll l_{scale} \sim \frac{q}{\mid \Delta q \mid}, \tag{2.1}$$

The region size is large enough that the element contains sufficient particles to ignore the fluctuations due to a finite number of particles. Thus:

$$n l_r^3 \gg 1, \tag{2.2}$$

where n is the particle number density.

In addition to the criteria for fluid description, a collisional fluid must satisfy the following criterion:

The fluid element is large enough so that the constituent particles softly collide with each other, so if the mean free path is λ, we require that

$$l_r \gg \lambda. \tag{2.3}$$

A relativistic description of fluid dynamics is necessary in situations where the local velocity of the flow is close to the speed of light or where the local internal energy density is comparable (or larger than) the local rest-mass density of the fluid. Relativistic flows are present in numerous astrophysical phenomena, from stellar to galactic scales. Phenomena of this type can be core collapse supernovae, X-rays binaries, pulsars, coalescing neutron stars and black holes, micro-quasars, active galactic nuclei, gamma-ray bursts and, in general, any astrophysical scenario involving compact objects.

§2.1.1 The equations of special relativistic hydrodynamics

The description of relativistic fluids, is constructed from the energy-momentum 4-tensor T^{ik} for a fluid in a flat space-time with a metric tensor g_{ik}, such that $(\mathrm{diag}(g)) = (1, -1, -1, -1)$. Here and in what follows Latin indices take values 0,1,2,3 and Greek are 1,2,3. We use Einstein summation notation convention over repeated indices and the signature of the metric is chosen as $(+, -, -, -)$ for the coordinates (ct, x, y, z) with c the speed of light. In general, the components of the symmetric tensor T^{ik} are such as $T^{00} = T_{00}$ is the energy density, and the space components $T^{0\alpha}/c = -T_{0\alpha}/c$ are the α-components of the momentum density vector. The components $T^{\alpha\beta} = T_{\alpha\beta}$ represents the 3-momentum flux-density tensor and $cT_{0\alpha}$ is the energy flux density vector. In the local rest frame of the fluid, according to Pascal's Principle: "the pressure exerted by a given portion of the fluid is the

same in all directions and perpendicular to the surface on which it acts". This enables us to express all the energy-momentum 4-tensor T^{ik} in the following form:

$$T^{ik} = \begin{pmatrix} e & 0 & 0 & 0 \\ 0 & p & 0 & 0 \\ 0 & 0 & p & 0 \\ 0 & 0 & 0 & p \end{pmatrix}, \tag{2.4}$$

where e is the proper energy density and p is the pressure. In order to obtain a general expression for T^{ik} in any frame of reference, we use the fact that the 4-velocity u^i has the values $u^0 = 1$ and $u^\alpha = 0$ in the local rest frame. Combining this with equation (2.4) it follows that:

$$T^{ik} = \omega u^i u^k - p g^{ik}, \tag{2.5}$$

where $\omega = e + p$ is the heat function or enthalpy per unit volume. Since equation (2.5) has the same form in any system of reference, it yields the required expression for the energy-momentum 4-tensor in relativistic fluid mechanics *.

The conservation of momentum and energy are represented by the null divergence of the energy momentum tensor, i.e.:

$$\frac{\partial T_i^{\ k}}{\partial x^k} = 0. \tag{2.6}$$

The motion equations do not include external sources of energy or momentum. They do not take in account any dissipative process. Let us now project (2.6) with the orthogonal 4-velocity u^i tensor $(\delta_i^l - u_i u^l)$, i.e.:

$$\frac{\partial T_i^k}{\partial x^k} - u_i u^l \frac{\partial T_l^k}{\partial x^k} = 0. \tag{2.7}$$

For the case of a perfect fluid the previous relation takes the following form:

$$\omega u^k \frac{\partial u_i}{\partial x^k} = \frac{\partial p}{\partial x^i} - u_i u^k \frac{\partial p}{\partial x^k}. \tag{2.8}$$

This last relation is known as the 4-dimensional Euler equation. The spatial components

*When discussing relativistic fluid mechanics we take the values of different thermodynamic quantities in their local proper frame. For example the internal energy density e, the enthalpy per unit volume ω, the entropy density σ, and the temperature T are all referred to this system of reference.

constitute the relativistic Euler equation:

$$\frac{\gamma\omega}{c^2}\left(\frac{\partial v}{\partial t} + v\cdot\nabla v\right) = -\nabla p - \frac{v}{c^2}\frac{\partial p}{\partial t}, \tag{2.9}$$

where v is the flow velocity and the Lorentz factor γ is ($\gamma^{-2} = 1 - v^2/c^2$). The time component of the relativistic Euler equation follows from the space components.

In the absent of sinks and sources, the continuity equation is (Landau & Lifshitz, 1995):

$$\frac{\partial n^k}{\partial x^k} = 0, \tag{2.10}$$

where the particle flux 4-vector $n^k = nu^k$ and the scalar n is the particle number density.

Projecting (2.6) on the direction of the 4-velocity and using the fact that $u^i u_i = 1$ implies

$$nu^k\left(\frac{\partial}{\partial x^k}\left(\frac{\omega}{n}\right) - \frac{1}{n}\frac{\partial p}{\partial x^k}\right) = 0. \tag{2.11}$$

Using the fist law of thermodynamics per unit volume $\mathrm{d}(\omega/n) = T\mathrm{d}(\sigma/n) + (1/n)\mathrm{d}p$, where T is the temperature and σ is the entropy per unit volume, we could rewrite (2.11) as:

$$u^k\frac{\partial}{\partial x^k}\left(\frac{\sigma}{n}\right) \equiv \frac{d}{ds}\left(\frac{\sigma}{n}\right) = 0. \tag{2.12}$$

In other words, as the fluid moves the quantity $\sigma/n = const$, i.e. the motion is adiabatic.

The system of equations requires a relation between thermodynamical quantities, this relation is known as a equation state for a gas. It is common in astrophysics to consider gases that change their thermodinamic quatities under cuasi-statical process. This gas was called polytopic gas.

For a polytropic gas the changes is done quasi-statical and is such that its specific heat remains constant during the entire process, from this it follows:

$$P/\rho^\kappa = const, \tag{2.13}$$

where the polytropic index κ is constant and has a value of $5/3$ for an adiabatic monoatomic gas.

In order to derive the non-relativistic equations of hydrodynamics, note that thermodynamics four quantities. In the relativistic case are defined with respect to the proper system of reference of the fluid. In non-relativistic thermodynamics, these quantities are

referred to the laboratory frame. Furthermore in the relativistic case, the thermodynamic quantities, such as the internal energy density e, the entropy density σ and the enthalpy density ω, are all defined with respect to the proper volume of the fluid. In non-relativistic fluid dynamics, these quantities are measured in units of mass of the fluid element they refer to. When taking the limit in which the speed of light c tends to infinity we must also bear in mind that the internal energy density e includes the rest energy density nmc^2, where m is the rest mass of the particular fluid element under consideration. Therefore, the following limits should be taken when moving from relativistic to non-relativistic fluid dynamics:

$$mn \underset{c\to\infty}{\longrightarrow} \rho\sqrt{1-\frac{v^2}{c^2}} \approx \rho\left(1-\frac{v^2}{c^2}\right), \tag{2.14}$$

$$e \underset{c\to\infty}{\longrightarrow} nmc^2 + \rho\epsilon \approx \rho c^2 - \frac{1}{2}\rho v^2 + \rho\epsilon, \tag{2.15}$$

$$\frac{\omega}{n} \underset{c\to\infty}{\longrightarrow} mc^2 + m\left(\epsilon + \frac{P}{\rho}\right) \approx m(c^2 + w). \tag{2.16}$$

§2.2 Shock waves

The phenomena of the knots explained as relativistic shock waves in the previous section constitute a fundamental piece of the emission process of the jets. As seen in different astrophysical objects from jets of active galaxies to μ-quasars, the emission and formation of internal shocks in jets, have been an active field in high energy astrophysics (Panaitescu et al., 1999; Spada et al., 2001; Kaiser et al., 2000; Bošnjak & Daigne, 2014; Levinson, 2006). The description of this type of shock requires a discontinuity in the fluid moving at relativistic velocities inside of a jet.

The laws of conservation of mass, momentum and energy in equations (2.6) and (2.10), can not only describe continuous flows but also discontinuous ones (Landau & Lifshitz, 1995). The surface of discontinuity is in general terms thinner than the characteristic length associated to the variations of the hydrodynamical quantities. Tangential discontinuities are stable only when the relative velocity of the flow is zero in both sides of the discontinuities. These stable tangential discontinuities can only occur in the density, leaving the pressure constant between both sides of the discontinuities. They are commonly designated as “contact discontinuities” are strong discontinuities that occur in all hydro-

dynamical quantities leaving continuous only the fluxes of mass, energy and momentum across the surface of discontinuity. They are known as shock waves.

For the case of a non-relativistic fluid, the conservation of mass, energy and momentum imply that the pre-shock (labelled with subindex 0) and post-shock (labelled with subindex 1) pressure P, density ρ and velocity v satisfy the following relations:

$$\rho_1 u_1 = \rho_0 u_0, \tag{2.17}$$

$$P_1 + \rho_1 u_1^2 = P_0 + \rho_0 u_0^2, \tag{2.18}$$

$$\epsilon_1 + \frac{P_1}{\rho_1} + \frac{u_1^2}{2} = \epsilon_0 + \frac{P_0}{\rho_0} + \frac{u_0^2}{2}, \tag{2.19}$$

where ϵ represents the specific internal energy of the flow. in terms of the specific enthalpy $h = \epsilon + P/\rho$, equation 2.19 takes the following form:

$$h_1 + \frac{u_1^2}{2} = h_0 + \frac{u_0^2}{2}. \tag{2.20}$$

Equations (2.17)-(2.19) form a system of three algebraic equations with six variables P_0, ρ_0, v_0, P_1, ρ_1 and v_1. By knowing the equation of state of the fluid and/or if a politropic relation is satisfied by it, the algebraic system can be solved for in terms of the pre-shocked quantities.

Equations (2.17), (2.18) and (2.19), can be manipulated so that the following relation is obtained:

$$\epsilon_0 - \epsilon_1 + \frac{1}{2}\left(\frac{1}{\rho_0} - \frac{1}{\rho_1}\right)(P_0 - P_1) = 0, \tag{2.21}$$

or

$$h_0 - h_1 + \frac{1}{2}\left(\frac{1}{\rho_0} + \frac{1}{\rho_1}\right)(P_1 - P_0) = 0, \tag{2.22}$$

By analogy with the physical equations between the initial and final pressures during an adiabatic compression of a fluid, the previous is named the shock adiabat relation or Hugoniot adiabat. It is important to note that the shocks are an irreversible process: the entropy, as well as P, ρ, and ϵ are discontinuous at the shock interface. Additionaly, $s_1 > s_0$ as consequence of the second the law of thermodynamics. This in turn implies that:

$$u_0 > c_{s0}, \quad u_1 < c_{s1}. \tag{2.23}$$

For all standard gases it follows that $\left(\partial^2 1/\rho/\partial p^2\right)_s > 0$, and so:

$$P_2 < P_1, \quad \rho_2 > \rho_1. \tag{2.24}$$

For the case of a polytropic gas equations (2.17) - (2.22) can be written as:

$$\rho_1/\rho 0 = (\gamma+1)M_0^2/\left((\gamma-1)\,M_0^2+2\right), \tag{2.25}$$

$$P_1/P_0 = \left(2\gamma M_0^2-(\gamma-1)\right)/(\gamma+1), \tag{2.26}$$

$$T_1/T_0 = \left(2\gamma M_0^2-(\gamma-1)\right)\left((\gamma-1)\,M_0^2+2\right)/(\gamma+1)^2\,M_0^2, \tag{2.27}$$

$$M_1^2 = \left(2+(\gamma-1)\,M_0^2\right)/\left(2\gamma M_0^2-(\gamma-1)\right), \tag{2.28}$$

where $M := v/c$ is the Mach number of the flow and c is the local speed of the sound.

When the discontinuities in the pressure across the shock wave are such that $P_1(\gamma-1) \gg P_2(\gamma+1)$ the shock is said to be strong with the consequence that $M_0 \gg 1$. For this particular case the density contrast reaches a constant value: $\rho_1/\rho_0 = (\gamma+1)/(\gamma-1)$ which has a value of 4 for for a monoatomic gas with polytropic index $\gamma = 5/3$.

Relativistic shocks in a Minkowsky space-time require more detail in their treatment, particularly since they are difficult to describe in different systems of inertial reference. For the case in which the shock wave discontinuity is at rest, equations (2.17)-(2.19) can be substituted by the following relations (Taub, 1948):

$$\frac{\gamma_1}{c}\rho_1 u_1 = \frac{\gamma_0}{c}\rho_0 u_0, \tag{2.29}$$

$$P_1 + \frac{\gamma_1}{c}\rho_1 u_1^2 = P_0 + \frac{\gamma_0}{c}\rho_0 u_0^2, \tag{2.30}$$

$$\omega_1 + u_1\gamma_1^2 = \omega_0 + u_0\gamma_0^2, \tag{2.31}$$

where ω is the enthalpy per unit volume and γ the Lorentz factor of the flow. Note that the previous relativistic Taub jump conditions do not reach a density contrast limit when the shock is strong, i.e. when $P_1 \gg P_2$. This is a helpful fact to understand the huge amounts of energy inferred from the observations of relativistic jets on different sources.

.

Chapter 3

A Semi-analytic model of internal shock waves inside astrophysical jets

The development of analytical and semi-analytical models for astrophysical relativistic jets, allow us to study the conditions of the jet with simple approximations to understand the fundamental role played by the shock wave physics in the emission process and the emission of its light curve. In this chapter we present the model developed by Mendoza et al. (2009), in order to describe relativistic internal shock waves. We also applied this model to the light curve of three particular objects, the knot HST-1,observed in the galaxy M87, the recent μ-quasar A06200-00 during its historical outburst in 1975-1976 and to the gamma ray light curve blazar PKS 1510-089.

§3.1 Introduction

The first model of internal shock waves in a jet starts with detailed and long term period radio observations of the radio lobes in distant radio galaxies. The high resolution images enable to resolve the conduits that feed on the lobes and see peculiar and curious knots or blobs travelling inside the jet. These were initially explained as the interaction of the jet with inhomogeneities of the surrounding medium. Other mechanisms include the changes in the geometry of the jet or deviations, and the time parameter fluctuations in the parameters of the ejection. This last mechanism was developed as an extension of the

models of ejection, (Raga et al., 1990; Raga & Kofman, 1992; Falle & Raga, 1993, 1995; Cantó et al., 2000) i.e. those those which do not involve relativistic speed, to a relativistic model.

Rees (1978) initially proposed a model with relativistic speeds including a variation in the speed of the material, producing internal shock waves in the jet. This model was constructed to explain the knots inside the jet in M87 with the result that the luminosity is a function of the time scale, variations of the flow and the material speed inside the jet. Later models of the structure and dynamics of extragalactic jets, show the knotty structure produced by different mechanisms such as instabilities on the flow of the jet, suggesting the existence of cuasi-periodic shock waves (Norman et al., 1982).

There are a quiet few analytical models used to explain non-relativistic internal shocks associated to the Herbig-Haro Objects with time-depend sources (Raga et al., 1990; Raga & Kofman, 1992; Falle & Raga, 1993, 1995; Cantó et al., 2000). They reproduce the knotty structure observed and predict the shock velocities, characteristic mass ejection rate and luminosity. Full relativistic numerical models commons are applied to GRBs (Mészáros, 2002; Rees & Meszaros, 1994; Panaitescu et al., 1999), Blazars (Boettcher, 2010) and μ-quasars (Kaiser et al., 2000).

In this chapter we describe the semi-analytical approach by Mendoza et al. (2009) for which the velocity variations make faster fluid overtake slower ejections producing an initial discontinuity, and so developing two shocks separated by a contact discontinuity, a hydrodynamical object known as a working surface that represents the emission region of the knots inside the jets (cf. Fig 3.1)

Although several models and particular aspects of the phenomenon have been presented in the literature (see e.g Panaitescu et al., 1999; Spada et al., 2001; Sahayanathan & Misra, 2005), there is no simple analytical description. The usual approach description assumes that the radiation time scales are small compared to the characteristic dynamical times of the jet (Spada et al., 2001). As a consequence, the pressure of the fluid is negligible and the collision is described approximately as ballistic. This assumption is valid if the flow within the jet is nearly adiabatic and non–turbulent (Sahayanathan & Misra, 2005).

Mendoza et al. (2009) proposed a model which describes the working surface as the collision of two parcels of fluid ejected in a preferred direction from a source with variable mass ejections ejections rates and/or speed ejections. The first parcel is initially ejected at a velocity $v_1(\tau)$ and the second at a velocity $v_2(\tau)$ at a later time, both dependent on the time τ as measured from the jet's source (see Figure 3.1). The condition $v_2 > v_1$ allows

for the parcel shocks to eventually form a working surface which travels along the jet at an average velocity $v_{ws}(\tau)$, as measured from the reference frame of the central engine.

Following the non–relativistic formalism first proposed by Cantó et al. (2000), assuming that the working surface is thin and that there are no mass losses within it (e.g. by sideways ejection of material (cf Falle & Raga, 1993, 1995) and that the ejected flow will move in a free-streamig way (Raga et al., 1990), Mendoza et al. (2009) developed a relativistic extension of the problem, showing that the energy loss inside the working surface could be calculated as the difference between the initial rest plus kinetic energy E_0 of the injected material, and the energy of the flow inside the working surface E_{ws}. Assuming an efficient mechanism which converts all this kinetic energy into radiation power, the total luminosity L is given by:

$$L := \frac{dE_{\rm r}}{{\rm d}t} \tag{3.1}$$

where $E_{\rm r} := E_0 - E_{\rm ws}{}^*$. The luminosity L turns out to be a function of the velocities $\mathrm{v}_1, \mathrm{v}_2$ of the fluid parcels, the proper times at which each parcel was ejected of each parcel and the mass ejection rate $\dot{m}$:

$$\begin{aligned} L = & \frac{\dot{m}(\tau_2)}{{\rm d}t/{\rm d}\tau_2}\left\{\gamma_{\rm ws} + \frac{m}{M_\gamma}\gamma_{\rm ws}^3\gamma_2\left(v_{\rm ws}v(\tau_2) - v_{\rm ws}^2\right) - \gamma_2\right\} \\ & - \frac{\dot{m}(\tau_1)}{{\rm d}t/{\rm d}\tau_2}\frac{{\rm d}\tau_1}{{\rm d}\tau_2}\left\{\gamma_{\rm ws} + \frac{m}{M_\gamma}\gamma_{\rm ws}^3\gamma_1\left(v_{\rm ws}v(\tau_1) - v_{\rm ws}^2\right) - \gamma_1\right\}, \end{aligned} \tag{3.2}$$

where the Lorentz factors $\gamma_{1,2}^{-2} := 1 - v^2(\tau_{1,2})$, the weighted mass ejected between the times τ_1 and τ_2, the mass inside the working surface is m and the subindex ws corresponds to the working surface.

*The result in equation (3.1) does not take into account any radiative terms, that should appear in any hydrodynamical radiation process (either relativistic or non-relativistic). As such this calculation and any further result deriving from it should be consider a first approximation to the problem of the formation, evolution and radiation of internal working surfaces propagating along an astrophysical jet. As it will be seen from the result obtain in the following chapters, the infer physical parameters of our model yield result very close to the once expected from different particular sources: GRB. blazars, quasars, micro-quasars. This means that our approximations do not deviate too much from a correct full numerical hydrodynamical simulation that takes into account radiation processes. Furthermore, the free parameters of the model require to fix real observational data. This statistical can only be achieve with the aid of a semi analytical model which produces a light curve in a small amount of time. Performing statistical calculations with a full hydrodynamical model we produce computational times extremely large to be developed with current computational power.

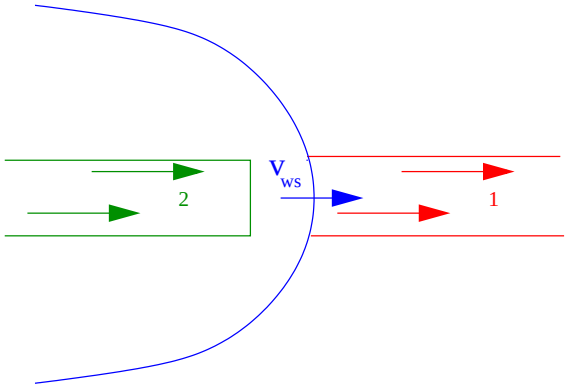

Figure 3.1: When a fast velocity flow 2 moves over a slow velocity flow 1, a working surface (represented with a curved line) moving with velocity $v_{\rm ws}$ is generated as a result of the interaction.

In order to test this analytical description, lets consider first the particular case where he mass ejection rate $\dot{m}$ is constant and generate a working surface with sinusoidal oscillations on the parcels of fluid at the base of the jet. In other words:

$$v(\tau) = v_0 + \eta^2 \sin \omega\tau, \tag{3.3}$$

in which the constant $\eta \ll 1$. These variations need to be small in order that the bulk velocity of the flow not exceed the speed of the light. Calculating the luminosity L with this velocity profile produces a general light curve depend only on the bulk velocity of the jet v_0, the mass ejection rate $\dot{m}$, the variation speed η and the frequency ω.

This model reproduces with high accuracy the light curves for long gamma-ray bursts as shown by Mendoza et al. (2009), using a simple linear fit between the luminosity and frequency, assuming these are around $10^{45} - 10^{46}$ W and $0.1 - 1.0$ sec respectively.

In the next sections we show the variety of applications of the model proposed by Mendoza et al. (2009), to active galaxies (in particular the nearest example the galaxy M87), a quasar and one of the most intense gamma rays active galaxy, the blazar PKS 1510-089. Finally, the fit light-curve in X-rays of the μ-quasar A06200, using this model.

§3.2 M87

The jet in the galaxy M87 is historically the most studied astrophysical extragalactic jet. Due to its close distance with z= 0.004360 (Jordán et al., 2005) and huge amount of observations in all wavelengths, it is to be taken as the prototype quasar. Due to its close distance, the good multiwavelength resolution of the jet allows to test its complex hydrodynamic effects such as the formation and evolution of shocks inside the jet, the related instabilities of the flow. The good resolution of the instruments and the long-time observations of the source have with time light curves of individual knots as they move inside the jet.

A particular knot, named HST-1 has been closely monitored by Biretta et al. (1999) all the way from its formation up to its internal motion along the jet.

In X-ray observations of HST-1 (Marshall et al., 2002), showed an unexpected high emission as compared to the other knots. Subsequent Chandra X-ray observations revealed a flare which attained a peak in 2005 (Harris et al., 2006).

This same behaviour was observed in optical-ultraviolet (Madrid, 2009) and radio bands (Chang et al., 2010), with successive peaks after the main burst in 2006 and 2011. Harris et al. (2009) found, via detailed studies of the X-ray observations in HST-1, quasi-periodic signatures in the brightening and dimming, showing a manifestation of a modulation in the jet power, where the local oscillation of the process most probably converts the bulk kinetic jet power to internal energy of the emitting plasma.

The complex emission mechanics in the HST-1 knot observed in the X-ray light curve during the outburst led construction of different models to explain its observed behaviour. For example, Cheung et al. (2007) built a model in which the main contribution to the X-rays is an effect of the hot accretion disc with its corona. Another model details particular features using a recollimation shock with the jet (Stawarz et al., 2006). Besides these explanations, part of the emission of the radio observations (Giroletti et al., 2012) show that the knot is well isolated from its nucleus and the activity region is displaced away from the central engine by $\gtrsim 120\,\mathrm{pc}$. These radio observations show also superluminal motion of the knot, which means that its bulk velocity is highly relativistic (Giroletti et al., 2012).

To analyse the light curve of HST-1, we use a time between the years 2000 to 2009, centred in the maximum flare that occurred in 2005. Since the observations cover different wavelengths, then it is best to normalise all observations to the intrinsic luminosity of HST-1. For X-rays we use the procedure developed in Harris et al. (2006), which gives a

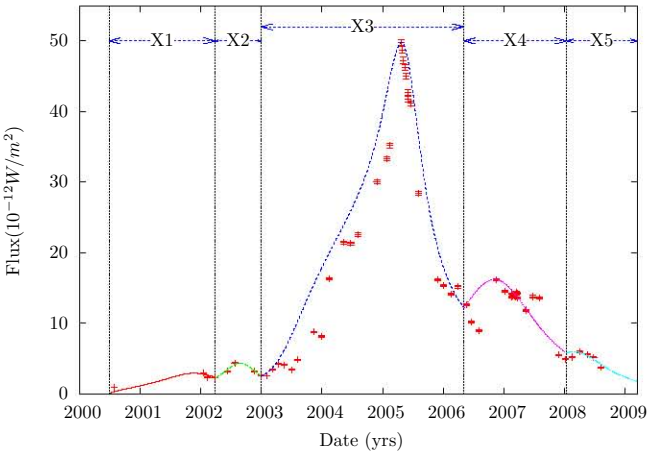

Figure 3.2: The figure show the fits (lines) to the X-ray data points of the light curve of the HST-1 knot observed by Harris et al. (2009) using the model by M09. The data points were divided into 5 time sections marked by the dotted vertical lines corresponding to individual outbursts, and labelled X1, X2, X3, X4 and X5. The resulting calibration of the free parameters of the model by M09 to the observed light curve are shown in Table 3.1.

power law index for the flux of 1.5 at a wavelength of 2cm (Chang et al., 2010). For the UV data we use the flux density using the reference wavelength of the camera ACS/F220W at 2255.5Å (Madrid, 2009).

We have assumed an isotropic emission of the source at a distance of 16 Mpc (Jordán et al., 2005), which gives a lower limit to the luminosity emitted by the HST-1 knot. On the other hand, the mean velocity v_0 of the jet is taken in a range $v_0 = 0.1\mathrm{c} - 0.999\mathrm{c}$ which is in agreement with the observed mean Lorentz factor of the knots in M87 (Biretta et al., 1999). The value of the parameters η^2 and the frequency ω of equation (3.3) are searched as an optimization problem by genetic algorithms (GA).

This algorithm of heuristic search mimic the natural evolution. In this search technique, the space of parameters initially are mapped by points considered as individuals (solution candidates), which as a whole form a population. The fitness of an individual is evaluated by a objective function, this value is a number indicating quality solution of the problem. In order to optimize the search of solutions by GAs, this include a set of fundamental genetic operations that work on the genotype (solution candidate codification): mutation, recombination and selection operators Mitchell (1998).

The fitting was made individually for each wavelength. Particularly, the light curve

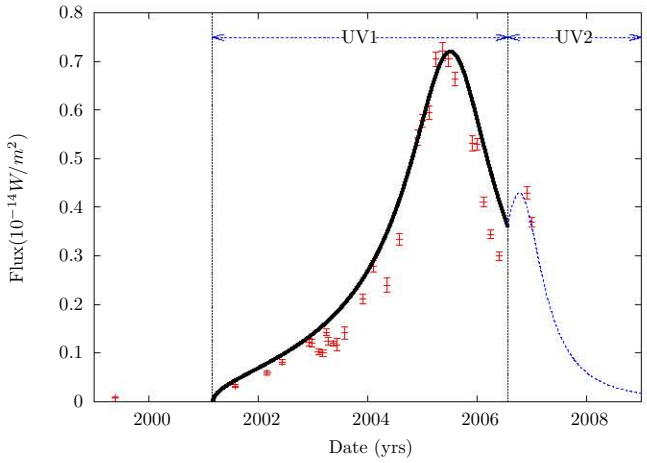

Figure 3.3: The figure show fits (lines) to the UV data points of the light curve of the HST-1 knot observed by Madrid (2009) using the model by M09. The data points were divided into 2 time sections marked by the dotted vertical lines corresponding to individual outbursts, and labelled UV1 and UV2. The resulting calibration of the free parameters of the model by M09 to the observed light curve are shown in Table 3.1.

of HST-1 does not fit with just a simple periodic variation on the velocity of the jet as described by equation (3.3). For this case it was also necessary to additionally adopt a periodic variation on the injected mass given by $\dot{m} = \dot{m}_0 + \dot{\mu}\sin\Omega t$, where $\dot{m}_0$ is the background average mass ejection rate and Ω is the oscillation frequency of the mass ejection rate. The parameter $\dot{\mu}$ is the amplitude of the injected oscillation. This corresponds to an increment of mass in the working surface, which in turns leads to a shock that rises the luminosity in a short period of time. This variation, add new parameters to the optimization. Finally the parameters v_0, η^2, $\dot{\mu}/\dot{m}_0$ and Ω/ω were searched in the range consistent with physical restrictions $v_0 = 0.1 - 0.999$, $\eta^2 = 10^{-4} - 0.889$, $\dot{\mu}/\dot{m}_0 = 10^{-3} - 1.0$ and $\Omega/\omega = 10^{-3} - 20$. We use as objective function the root sum square (RSS) between the numeric results of the model and the observed data, in order to obtain the best fit parameters to the light curves of the observed data.

The results are shown in figures (3.2)-(3.4), and as it can be seen from the figures there is at least one subsequent increase in luminosity after the maximum peak. Local peaks are modelled by GA, including rapid variation of the value of the discharge $\dot{m}$ injected in the jet according to the high variability of the core of M87 (Harris et al., 2009).

The formation and evolution of the knot HST-1 modelled by simple variations serve to

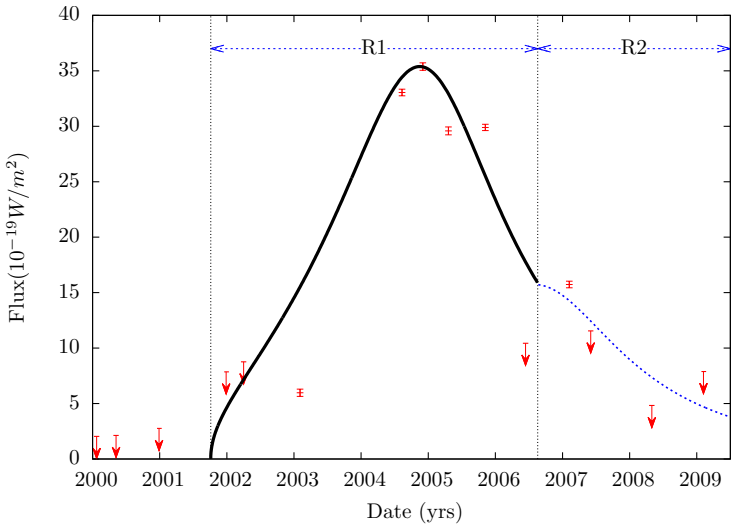

Figure 3.4: The figure show fits (lines) to the radio data points of the light curve of the HST-1 knot observed by Chang et al. (2010) using the model by M09. The data points were divided into 2 time sections marked by the dotted vertical lines corresponding to individual outbursts, and labelled R1 and R2. The resulting calibration of the free parameters of the model by M09 to the observed light curve are shown in Table 3.1.

ID	v_0/c	η^2/c	$\dot{m}_0$ $(10^{-3}M_\odot \mathrm{yr}^{-1})$	$\dot{\mu}$ $(10^{-3}M_\odot \mathrm{yr}^{-1})$	$\dot{m}_{\max}$ $(10^{-3}M_\odot \mathrm{yr}^{-1})$	ω_0^{-1} (days)	Ω^{-1} (days)	$\Gamma_{\min}$	$\Gamma_{\max}$	Γ_{bulk}
X_1	0.9631	0.0360	4.252	0.415	4.667	53.8	0.716	2.67	23.12	3.72
X_2	0.9573	0.0420	3.476	1.119	4.596	26.4	4.361	2.48	27.32	3.46
X_3	0.8156	0.1839	9.727	3.943	13.671	374	2322.5	1.29	31.32	1.73
X_4	0.9713	0.0275	36.56	3.351	39.916	118	45.874	3.03	20.16	4.2
X_5	0.9150	0.0823	4.511	2.057	6.569	83.5	36.0	1.81	13.49	2.48
			$(10^{-6}M_\odot \mathrm{yr}^{-1})$	$(10^{-6}M_\odot \mathrm{yr}^{-1})$	$(10^{-6}M_\odot \mathrm{yr}^{-1})$					
UV_1	0.9020	0.0976	1.569	0.588	2.157	296	50.818	1.68	32.97	2.32
UV_2	0.9762	0.0228	8.094	3.338	11.433	16.1	4.139	3.31	22.83	4.61
			$(10^{-9}M_\odot \mathrm{yr}^{-1})$	$(10^{-9}M_\odot \mathrm{yr}^{-1})$	$(10^{-9}M_\odot \mathrm{yr}^{-1})$					
R_1	0.9450	0.0536	2.650	2.033	4.683	195.5	33.072	2.21	19.18	3.06
R_2	0.9724	0.0270	9.156	2.821	11.978	75.43	31.21	3.07	27.12	4.28

Table 3.1: Best parameter estimations using the X-ray, UV and radio light curves of the HST-1 knot of the galaxy M87. The resulting light curves are shown in Figures 3.2-3.4. The fits were performed by dividing the light curves in time ID sections represented by the first column of the table. The quantity $\dot{m}_{\max}$ corresponds to the maximum mass ejection rate discharged by the jet for a particular outburst. The values $\Gamma_{\min}$, $\Gamma_{\max}$ and Γ_{bulk} are the minimum, maximum and background (i.e. v_0 bulk "average" velocity of the flow) Lorentz factors of the flow. All parameters were obtained to a precision above a 2-σ statistical confidence level.

call; rate initial model parameters, such as the velocity v_0 with the Lorentz factor $\Gamma \sim 2-35$ and mass ejection rates $\dot{m}_0 \sim 10^{-3}\mathrm{M}_{\odot}$. These are in good agreement with the mean value observed values of for the knot during the flare of 2005.

Mon. Not. R. Astron. Soc. **000**, 000–000 (0000) Printed 28th May 2015 (MN LATEX style file v2.2)

Understanding the light curves of the HST-1 knot in M87 with internal relativistic shock waves along its jet

Y. Coronado[1], O. López-Corona[1,2] & S. Mendoza[1⋆]
[1] *Instituto de Astronomía, Universidad Nacional Autónoma de México, AP 70-264, Distrito Federal 04510, México*
[2] *Centro de Ciencias de la Complejidad, Universidad Nacional Autónoma de México, Ciudad Universitaria, Distrito Federal, México.*

ABSTRACT
Knots or blobs observed in astrophysical jets are commonly interpreted as shock waves moving along them. Long time observations of the HST-1 knot inside the jet of the galaxy M87 have produced detailed multiwavelength light curves. In this article, we model these light curves using the semi-analytical approach developed by Mendoza et al. (2009). This model was developed to account for the light curves of working surfaces moving along relativistic jets. These working surfaces are generated by periodic oscillations of the injected flow velocity and mass ejection rates at the base of the jet. Using genetic algorithms to fit the parameters of the model, we are able to explain the outbursts observed in the light curves of the HST-1 knot with an accuracy greater than a 2-σ statistical confidence level.

Key words: hydrodynamics – relativistic processes – shock waves – galaxies:jets.

1 INTRODUCTION

The jet in the galaxy M87 was detected in the optical band by Curtis (1918). It is the closest Active Galaxy Nuclei with a redshift $z = 0.004360$ and has been extensively monitored in multi-frequency campaigns, particularly over the last decade. Radio interferometry and high resolution optical and X-ray observations show the complex structures formed inside the jet as close as $\sim$ 100pc from the nucleus (Waters & Zepf 2005). The most exotic of these structures, is a particular knot formed in 1999 and labelled HST-1. The evolution of HST-1 began to be closely followed in 2000 with the Chandra X-ray telescope (Harris et al. 2003, 2006, 2009) since it started to develop a rapid increase on its X-ray emission, achieving a maximum in 2005, corresponding to a factor of 50 as compared to the emission detected in 2000. After this maximum, the emission decreases and is followed by two further increments in 2006 and 2008. Ultraviolet (Madrid 2009) and radio (Chang et al. 2010) observations show a similar behaviour of its light curve. The whole emission of M87 presents an optical outburst in 2005 (Madrid 2009) which is related to the maximum emission of the HST-1 knot in the same year. This strongly suggests that the outburst is produced by the strong emission of the knot.

Knots in astrophysical jets are usually identified with internal shock waves travelling along the jet. These internal shock waves can be produced by different mechanisms: (a) interactions of the jet with an overdense medium, e.g. clouds (cf. Mendoza 2000; Mendoza & Longair 2001), (b) bending of jets above a critical value (Mendoza 2000; Mendoza & Longair 2002), and (c) Periodic variations of the injected velocity and mass at the base of the jet (e.g. Rees & Meszaros 1994; Jamil et al. 2008; Mendoza et al. 2009, and references therein).

In the literature, the main contribution of the X-ray emission of the HST-1 knot is still under discussion and the interpretations vary between an effect of a hot accretion disc with the corona (Marscher et al. 2002) and a particular phenomena of a re-collimation shock (Stawarz et al. 2006), causing the impressive flare in X-rays. Later observations in radio revealed superluminal motions in HST-1 being a well isolated knot from the nucleus (Biretta et al. 1999), displaced from the central engine by $\geqslant$ 120 pc (Cheung et al. 2007). All this makes HST-1 the best studied knot for a possible internal shock mechanism inside a jet. It is also an ideal target to observe due to its proximity. The strong multiwavelength emission from the jet and its knots allow to test the physics of knots and shock waves in the relativistic regime.

Since relativistic outbursts are usually thought of as internal shock waves travelling along the jet, produced by periodic variations of the injected flow, it is quite natural to model the high emission light curve of the HST-1 knot as shock waves produced by this mechanism. The semi-analytical model by Mendoza et al. (2009) (denoted as M09 in what follows) has been quite useful in modelling not only outbursts associated to long gamma-ray bursts but also to the many outbursts detected on the light curve of the blazar PKS 1510-089 (Cabrera et al. 2013). We show in this article, that such a model is also good for modelling and understand-

⋆ E-mail address: {coronado,olopez,sergio}@astro.unam.mx.

ing the multi-frequency features observed in the HST-1 knot of the M87 galaxy.

Harris et al. (2009) found a quasi-periodic impulse signature in the brightening and dimming of the core of M87. This was interpreted as a manifestation of past modulation of jet power, possibly by a local oscillation of the process that converts the bulk kinetic jet power to the internal energy of the emitting plasma. This result reinforces the use of the M09 model in order to explain the formation and evolution of the HST-1 knot.

The article is organised as follows. In section 2 we present the multi-wavelength observation campaigns of the HST-1 knot and its light curves features. In section 3 we present a brief description of the hydrodynamical model developed by Mendoza et al. (2009) and the system of dimensionless units in which it is useful to make comparisons with observations. The fits to the light curves using the hydrodynamical model of Mendoza et al. (2009) are developed in the section 4. The result of our fits and a discussion of the obtained physical parameters of the model are presented in section 5.

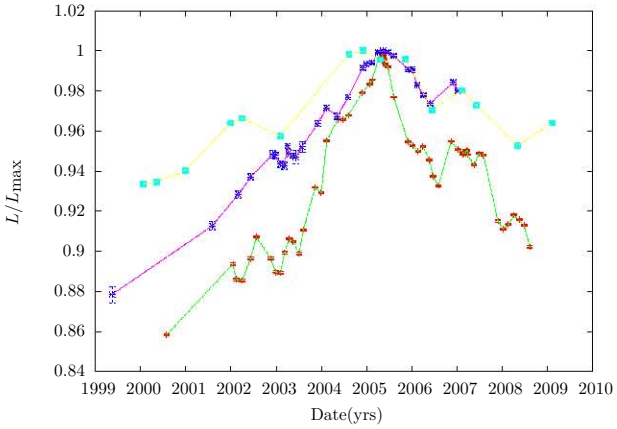

Figure 1. The figure shows multi-frequency luminosity curves of the HST-1 knot of the galaxy M87. All curves have been normalised to the maximum intensity. From bottom to top the curves represent 2cm radio (Chang et al. 2010), 225.5nm UV Madrid (2009) and Chandra 2Kev X-ray (Harris et al. 2009).

2 OBSERVATIONAL DATA

The multi-frequency light curves were taken from three separate datasets and are shown in Figure 1. X-ray observations were taken from a multi-frequency program coordinating Chandra and HST monitoring (Harris et al. 2009). Ultraviolet data are part of the same program and carried out during the years 1999 to 2006 (Madrid 2009). Finally the radio data corresponds to observations with the VLBI at 2cm (Chang et al. 2010). As mentioned in section 1, these all show a clear outburst with a maximum emission occurring in 2005. After this epoch, subsequent micro-outbursts differ from each other in the global decay of the light curve. Although all the observational data show the same morphology in the light curves, the spectral power law differs in each section of the spectrum from radio to X-rays, revealing that a simple power law cannot describe the whole spectra of HST-1 (Harris et al. 2009).

We calculate the flux in X-rays following the procedure described by Harris et al. (2006) and applied it to the observational intensities of the HST-1 knot reported by Harris et al. (2009). The flux in ultraviolet and radio wavelengths is calculated with a conversion between Jy to W/m^2, using a reference wavelength of 225.55nm for the ultraviolet data (Madrid 2009) and 2cm for the radio measurements (Chang et al. 2010).

We assume a negligible extinction factor and an isotropic emission of the source, located at a distance of 16Mpc corresponding to the distance to the galaxy M87 (Jordán et al. 2005). With these assumptions we obtain a lower limit for the luminosity of the HST-1 knot in different wavelengths.

3 MODEL

Let us assume that periodic injections of velocity and mass flows are injected at the base of a 1D relativistic flow moving along a jet and consider a particular time on the ejection process in which a fast parcel of flow is ejected after a slow one. A time later, the fast parcel will "overtake" the slow one and the flow will become multi-valued. In order to arrange this contradiction, nature creates an initial discontinuity of the hydrodynamical values which later develops into a working surface, i.e. a contact discontinuity bounded by two shock waves, that moves along the jet on the direction of the flow as measured from the central engine (see e.g. Landau & Lifshitz 1995).

The first ideas about radiative internal shock waves inside an astrophysical jet were developed by Rees & Meszaros (1994); Daigne & Mochkovitch (1998). Although several extensions and particular aspects of the model have been presented in the literature (see e.g Panaitescu et al. 1999; Spada et al. 2001; Sahayanathan & Misra 2005). A semi-analytical description of this phenomenon was made by M09. These last model assumes periodic injections of mass and velocity at the base of the jet. Using mass and conservations of the ejected material, it is possible to account for the kinetic power loss as the working surface travels along the jet, assuming that the radiation time scales are small compared to the characteristic dynamical times of the problem. The pressure of the fluid is thus negligible and so the description of the flow can be well described by a ballistic approximation. This assumption is valid if the flow within the jet is nearly adiabatic and non–turbulent (see e.g. Sahayanathan & Misra 2005). In what follows we will use the model by M09 to describe the multiwavelength light curve features of the HST-1 knot in M87.

To follow the evolution of the working surfaces M09 considered a source ejecting material in a preferred direction with a velocity $v(\tau)$ and a mass ejection rate $\dot{m}(\tau)$, both dependent on the time τ as measured from the jet's source. A further assumption is made such that the working surface is thin and mass losses within it are negligible. The energy loss $E_{\rm r}$ by the working surface is given by $E_{\rm r} = E_0 - E_{\rm ws}$, where E_0 is the injected energy at the base of the jet and $E_{\rm ws}$ is the energy inside the working surface. The kinetic power available within the working surface is then given by $\mathrm{d}E_r/\mathrm{d}t$. If this power is converted efficiently into radiated

energy then the Luminosity L produced by the emission of the working surface is given by $L = -\mathrm{d}E_r/\mathrm{d}t$.

On the one hand, we assume that the injected velocity at the base of the jet is a periodic function of time, given by:

$$v(\tau) = v_0 + c\eta^2 \sin(\omega\tau), \tag{1}$$

where the velocity v_0 is the "background" average bulk velocity of the flow inside the jet and ω is the oscillation frequency of the injected velocity. The positive dimensionless parameter η^2 measures the amplitude variations of the flow and is such that the oscillations of the flow are sufficiently small, in such a way that the total bulk velocity $v(\tau)$ does not exceeds the velocity of light c.

On the other hand, the mass ejection rate $\dot{m}$ injected at the base of the jet has the following periodic variation:

$$\dot{m} = \dot{m}_0 + \dot{\mu}\sin(\Omega\tau). \tag{2}$$

where $\dot{m}_0$ is the "background" average mass ejection rate and Ω is the oscillation frequency of the mass ejection rate. The parameter $\dot{\mu}$ is the amplitude of the injected oscillation.

In the original article by M09 and in further applications (see Cabrera et al. 2013; Coronado & Mendoza 2014), have succeed in modelling outbursts of long gamma-ray bursts, blazars and micro-quasars assuming that $\dot{\mu} = 0$ and so $\dot{m} =$ const. . Although this simplifies the number of free parameters of the model, it turns out that the light curve of the HST-1 knot in M87 cannot be modelled with such a simple assumption.

In order to use the semi-analytical ballistic M09 model on its more general form, we proceed as follows. The model depends on six unknown parameters: v_0, η^2, ω, $\dot{m}_0$, $\dot{\mu}$, and Ω. To reduce the number of unknown parameters, we proceed as follows.

The luminosity L depends on six dimensional parameters: v_0, η^2, ω, $\dot{m}_0$, $\dot{\mu}$, and Ω. Additionally, the velocity of light c is an important dimensional parameter of the relativistic phenomena we are dealing with and so, it has to be added to the list of important dimensional quantities of the problem. Since there are three fundamental independent dimensions, namely the dimensions of time, length and mass, Buckingham's Π-Theorem of dimensional analysis means that the luminosity can be described as follows:

$$L = \dot{m}_0 c^2\, L'\left(v_0/c,\ \eta^2/c,\ \dot{\mu}/\dot{m}_0,\ \Omega/\omega\right). \tag{3}$$

In the previous equation, the dimensionless luminosity L' is a function of the four dimensionless quantities v_0/c, η^2/c, $\dot{\mu}/\dot{m}_0$, Ω/ω. In other words, the seven dimensional quantities for which the luminosity depends on, can be reduced to the problem of only four dimensionless quantities.

4 FITS TO THE OBSERVATIONAL DATA

The observed and theoretical luminosity, $L_{\rm obs}$ and $L_{\rm th}$ can be fit to the observational data with the use of their dimensionless counterparts $L'_{\rm obs}$ and $L'_{\rm th}$ by rescaling them as follows. Both theoretical and observed dimensionless luminosities can be normalised to their maximum values: $L'_{\rm obs}(\tau'_{\rm max})$ and $L'_{\rm th}(\tau'_{\rm max})$, i.e.

$$\mathbb{L}_{\rm obs} := \frac{L'_{\rm obs}}{L'_{\rm obs}(\tau'_{\rm obs,max})}, \qquad \mathbb{L}_{\rm th} := \frac{L'_{\rm th}}{L'_{\rm th}(\tau'_{\rm th,max})}, \tag{4}$$

where the dimensionless times $\mathbb{T}_{\rm obs,max}$ and $\mathbb{T}_{\rm th,max}$ correspond to the particular times where the observed or theoretical luminosities reach a maximum value respectively. According to Buckingham's Π-Theorem of dimensional analysis, the dimensionless time τ' is related to the time τ by the following relation:

$$\tau = \omega^{-1}\tau'. \tag{5}$$

In order to measure the observed and theoretical times in the same system of dimensionless units we normalised them to the time given by the FWHM of the outburst, i.e.:

$$\mathbb{T}_{\rm obs} := \frac{\tau'_{\rm obs}}{\tau'_{\rm obs}(\mathrm{FWHM})}, \qquad \mathbb{T}_{\rm th} := \frac{\tau'_{\rm th}}{\tau'_{\rm th}(\mathrm{FWHM})}. \tag{6}$$

The best fit of the theoretical luminosity $\mathbb{L}_{\rm th}(\mathbb{T}_{\rm th}$ to the observed light curve $\mathbb{L}_{\rm obs}(\mathbb{T}_{\rm obs}$ yields a direct best value for the four dimensionless free parameters v_0/c, η^2/c, $\dot{\mu}/\dot{m}_0$, Ω/ω. Once these parameters are obtained, then v_0 and η^2 are immediately inferred. The quantity $\dot{m}_0$ is obtained by using (6) evaluated at one particular point of the light curve, which we choose as the point where the light curve reaches its maximum value. Once this last quantity is known, the value for the parameter $\dot{\mu}$ is hence inferred. The frequency ω is obtained using equation (5) evaluated for a particular time, which we choose as the time where the light curve reaches its maximum value. With this, the parameter Ω is then inferred.

The parameter calibration of the model is conceptualised as an optimisation problem and so, we propose to solve it using Genetic Algorithms (GAs), which is an evolutionary based stochastic search algorithm that mimics natural evolution. In this heuristic search technique, points in the search space are considered as individuals (solution candidates), which as a whole form a population. The particular fitness of an individual is a number, indicating its quality for the problem at hand. As in nature, GAs include a set of fundamental genetic operations that work on the genotype, i.e. the solution candidate codification, namely: mutation, recombination and s election operators Mitchell (1998). These algorithms operate with a population of individuals $P(t) = x_1^t, ..., x_N^t$, for a particular t iteration, where the fitness of each x_i individual is evaluated according to a set of objective functions $f_j(x_i)$. This objectives functions allows to order from best to worst individuals of the population in a continuum of degrees of adaptation. Individuals with higher fitness, recombine their genotypes to form the gene pool of the next generation, in which random mutations are also introduced to produce a new variability.

A fundamental advantage of GAs versus traditional methods is that GAs solve discrete, non-convex, discontinuous, and non-smooth problems successfully and so, they have been widely used in Ecology, Natural Resources Management, among other fields (López-Corona et al. 2013) with some astrophysical applications (see e.g. Feigelson &

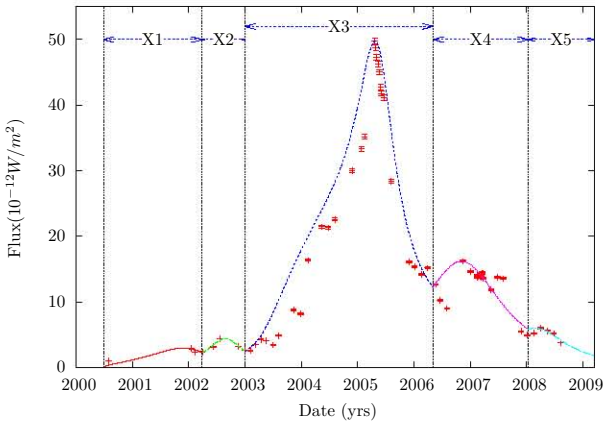

Figure 2. The figure show the fits (lines) to the X-ray data points of the light curve of the HST-1 knot observed by Harris et al. (2009) using the model by M09. The data points were divided into 5 time sections marked by the dotted vertical lines corresponding to individual outbursts, and labelled X1, X2, X3, X4 and X5. The resulting calibration of the free parameters of the model by M09 to the observed light curve are shown in Table 1.

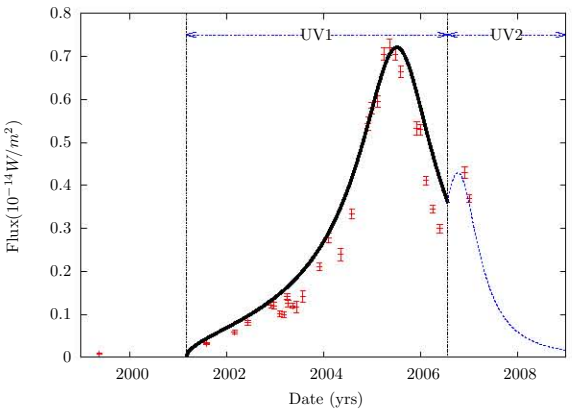

Figure 3. The figure show fits (lines) to the UV data points of the light curve of the HST-1 knot observed by Madrid (2009) using the model by M09. The data points were divided into 2 time sections marked by the dotted vertical lines corresponding to individual outbursts, and labelled UV1 and UV2. The resulting calibration of the free parameters of the model by M09 to the observed light curve are shown in Table 1.

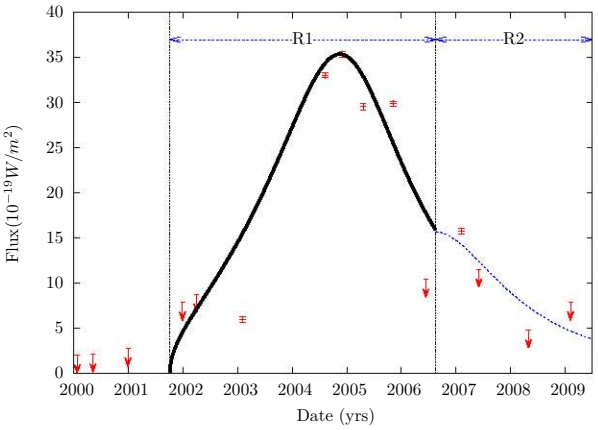

Figure 4. The figure show fits (lines) to the radio data points of the light curve of the HST-1 knot observed by Chang et al. (2010) using the model by M09. The data points were divided into 2 time sections marked by the dotted vertical lines corresponding to individual outbursts, and labelled R1 and R2. The resulting calibration of the free parameters of the model by M09 to the observed light curve are shown in Table 1.

Babu 2012). Our GA evaluated the luminosity function $\mathbb{L}_{\rm th}\left(v_0/c,\ \eta^2/c,\ \dot{\mu}/\dot{m}_0,\ \Omega/\omega\right)$ of M09 in order to compare numerical results from the model with the observed light curve $\mathbb{L}_{\rm obs}$ using standard Residual Sum of Squares (RSS) as objective functions. All parameters were searched in the broadest possible range: $0.1 \lesssim v_0/c \lesssim 0.999$, $0.0001 \lesssim \eta^2 \lesssim 0.899$, $0.001 \lesssim \dot{\mu}/\dot{m}_0 \lesssim 1.0$ and $0.001 \lesssim \Omega/\omega \lesssim 20$. The choice is consistent with the physical restriction of keeping subliminal the full bulk velocity of the flow v and to the fact that a large value of $\dot{\mu}/\dot{m}_0$ would yield a huge unphysical luminosity value. A very large value of Ω/ω produces large mass ejection oscillations, something not clearly visible from the light curves. This search parameter technique generates populations of 100 possible solutions over a maximum 5000 generation search process, with a total of 500000 individuals. The GA algorithms selected were: tournament selection with replacement (Goldberg et al. 1989; Sastry & Goldberg 2001), simulated binary crossover (SBX) (Deb & Kumar 1995) and polynomial mutation (Deb & Kumar 1995; Deb 2001). The obtained final parameters were estimated by averaging the 500 best individuals.

Direct inspection of the light curves in Figure 1 show that multiple outbursts occur during the period of observation. As such and following the procedure of Cabrera et al. (2013) we divided the light curves into individual outbursts. Two clear outbursts appear on all wavelength observations and an additional 3 mini-outburst were defined for the X-ray data -two before the main outburst and one at the end of the observations. The results of the GA explained above for each outburst are presented in Table 1 and the best fits to the light curves with these parameters are shown in Figures 2-4.

5 DISCUSSION

Every modelling process goes an initial exploratory face in which a basic hypothesis space is set up. In this context, Williams (2014) found that a good modelling process should: (a) stay as close as data as possible, (b) includes as much phenomenological information as possible and (c) keep as simple as possible.

The parameter estimation of the model is quite close to the observational data (since it has a $\gtrsim 2\sigma$ confidence level value), with a simple ballistic model describing a complicated hydrodynamical phenomenon.

At first sight, the curves seem not to properly adjust to many data points, as one should expect with such small observational uncertainties in the data. However, the time series represented by the light curve has many temporal gaps. Between these temporal gaps, the value of the inferred physical parameters may not stay the same, making the light curve to present mini-outbursts combined with different oscillations. For example, the data points about 2007 in X-rays can be modelled as a series of mini-outbursts. But model-

ID	v_0/c	η^2/c	$\dot{m}_0$ $(10^{-3}M_\odot \mathrm{yr}^{-1})$	$\dot{\mu}$ $(10^{-3}M_\odot \mathrm{yr}^{-1})$	$\dot{m}_{\max}$ $(10^{-3}M_\odot \mathrm{yr}^{-1})$	ω_0^{-1} (days)	Ω^{-1} (days)	$\Gamma_{\min}$	$\Gamma_{\max}$	Γ_{bulk}
X_1	0.9631	0.0360	4.252	0.415	4.667	53.8	0.716	2.67	23.12	3.72
X_2	0.9573	0.0420	3.476	1.119	4.596	26.4	4.361	2.48	27.32	3.46
X_3	0.8156	0.1839	9.727	3.943	13.671	374	2322.5	1.29	31.32	1.73
X_4	0.9713	0.0275	36.56	3.351	39.916	118	45.874	3.03	20.16	4.2
X_5	0.9150	0.0823	4.511	2.057	6.569	83.5	36.0	1.81	13.49	2.48
			$(10^{-6}M_\odot \mathrm{yr}^{-1})$	$(10^{-6}M_\odot \mathrm{yr}^{-1})$	$(10^{-6}M_\odot \mathrm{yr}^{-1})$					
UV_1	0.9020	0.0976	1.569	0.588	2.157	296	50.818	1.68	32.97	2.32
UV_2	0.9762	0.0228	8.094	3.338	11.433	16.1	4.139	3.31	22.83	4.61
			$(10^{-9}M_\odot \mathrm{yr}^{-1})$	$(10^{-9}M_\odot \mathrm{yr}^{-1})$	$(10^{-9}M_\odot \mathrm{yr}^{-1})$					
R_1	0.9450	0.0536	2.650	2.033	4.683	195.5	33.072	2.21	19.18	3.06
R_2	0.9724	0.0270	9.156	2.821	11.978	75.43	31.21	3.07	27.12	4.28

Table 1. Best parameter estimations using the X-ray, UV and radio light curves of the HST-1 knot of the galaxy M87. The resulting light curves are shown in Figures 2-4. The fits were performed by dividing the light curves in time ID sections represented by the first column of the table. The quantity $\dot{m}_{\max}$ corresponds to the maximum mass ejection rate discharged by the jet for a particular outburst. The values $\Gamma_{\min}$, $\Gamma_{\max}$ and Γ_{bulk} are the minimum, maximum and background (i.e. v_0 bulk "average" velocity of the flow) Lorentz factors of the flow. All parameters were obtained to a precision above a 2-σ statistical confidence level.

ling such a number of mini-bursts in a context of insufficient physical data represents an increase of unjustified additional hypothesis, despite the fact of an increment in statistical accuracy. As pointed out by Roos & Rakos (2000) it should be expected some sort of conflict between parsimony and realism. Nevertheless as models tends to incorporate more hypothesis, and become increasingly complex there is lose in transparency interpretation.

The model by M09 has shown to be quite useful reproducing light curves of long gamma-ray bursts, blazars and micro-quasars. As we have shown in this article, the same model is also good for dealing with the light curve of the HST-1 knot of M87. Our modelling can be adjust more precisely to the observed data by suitably performing more subdivisions of the data set, essentially modelling many mini-outburst. Since no data is available for these mini-outbursts, their introduction would be speculative. In this sense, the current modelling can be interpreted as a baseline modelling (Schwab & Starbuck 2013) that captures the key patterns in the empirical data and the associated physical processes.

ACKNOWLEDGMENTS

This work was supported by DGAPA-UNAM (IN111513-3) and CONACyT (240512) grants. YC, OL and SM acknowledge economic support from CONACyT (210965, 62929 and 26344). OL acknowledges economic support from a DGAPA-UNAM fellowship.

References

Biretta J. A., Sparks W. B., Macchetto F., 1999, ApJ, 520, 621

Cabrera J. I., Coronado Y., Benítez E., Mendoza S., Hiriart D., Sorcia M., 2013, MNRAS, 434, L6

Chang C. S., Ros E., Kovalev Y. Y., Lister M. L., 2010, åp, 515, A38+

Cheung C. C., Harris D. E., Stawarz Ł., 2007, ApJL, 663, L65

Coronado Y., Mendoza S., 2014, arXiv:1401.5395

Curtis H. D., 1918, Publications of Lick Observatory, 13, 55

Daigne F., Mochkovitch R., 1998, MNRAS, 296, 275

Deb K., 2001, Multi-objective optimization using evolutionary algorithms. Vol. 16, John Wiley & Sons

Deb K., Kumar A., 1995, Complex systems, 9, 431

Feigelson E., Babu G., 2012, Modern Statistical Methods for Astronomy: With R Applications. Cambridge University Press

Goldberg D. E., Korb B., Deb K., 1989, Complex systems, 3, 493

Harris D. E., Biretta J. A., Junor W., Perlman E. S., Sparks W. B., Wilson A. S., 2003, ApJL, 586, L41

Harris D. E., Cheung C. C., Biretta J. A., Sparks W. B., Junor W., Perlman E. S., Wilson A. S., 2006, ApJ, 640, 211

Harris D. E., Cheung C. C., Stawarz Ł., Biretta J. A., Perlman E. S., 2009, ApJ, 699, 305

Jamil O., Fender R. P., Kaiser C. R., 2008, in Microquasars and Beyond Internal Shocks Model for Microquasar Jets

Jordán A., Côté P., Blakeslee J. P., Ferrarese L., McLaughlin D. E., Mei S., Peng E. W., Tonry J. L., Merritt D., Milosavljević M., Sarazin C. L., Sivakoff G. R., West M. J., 2005, ApJ, 634, 1002

Landau L., Lifshitz E., 1995, Fluid Mechanics, 2nd ed. edn. Vol. 2 of Course of Theoretical Physics, Pergamon

López-Corona O., Padilla P., Escolero O., Armas F., Garca-

Arrazola R., Esparza R., 2013, Complexity, 19, 9
Madrid J. P., 2009, Astronomical Journal, 137, 3864
Marscher A. P., Jorstad S. G., Gómez J., Aller M. F., Teräsranta H., Lister M. L., Stirling A. M., 2002, Nature, 417, 625
Mendoza S., 2000, PhD thesis, Cavendish Laboratory, Cambridge University U.K., available at `http://www.mendozza.org/sergio/phdthesis`
Mendoza S., Hidalgo J. C., Olvera D., Cabrera J. I., 2009, MNRAS, 395, 1403
Mendoza S., Longair M. S., 2001, MNRAS, 324, 149
Mendoza S., Longair M. S., 2002, MNRAS, 331, 323
Mitchell M., 1998, An Introduction to Genetic Algorithms. A Bradford book, Bradford Books
Panaitescu A., Spada M., Mészáros P., 1999, ApJL, 522, L105
Rees M. J., Meszaros P., 1994, ApJL, 430, L93
Roos A., Rakos C., 2000, Biomass and Bioenergy, 18, 331
Sahayanathan S., Misra R., 2005, ApJ, 628, 611
Sastry K., Goldberg D. E., 2001, Intelligent Engineering Systems Through Artificial Neural Networks, 11, 129
Schwab A., Starbuck W. H., 2013, Philosophy of Science and Meta-Knowledge in International Business and Management, 26, 171
Spada M., Ghisellini G., Lazzati D., Celotti A., 2001, MNRAS, 325, 1559
Stawarz Ł., Aharonian F., Kataoka J., Ostrowski M., Siemiginowska A., Sikora M., 2006, MNRAS, 370, 981
Waters C. Z., Zepf S. E., 2005, ApJ, 624, 656
Williams B. G., 2014, arXiv preprint arXiv:1412.2788

§3.3 μ-quasar A06200-00

In order to probe the generality of the model by Mendoza et al. (2009) in different type of objects, we now proceed to see its applicability to μ-quasars, which are a somewhat scaled version of a quasar (see sections §1.3- §1.5). To do this, we had selected the μ-quasar A06200, which exhibited a huge X-ray outburst from 1975 to 1976.

We modelled the source with two different scenarios. The first considers two separated superpositioned bursts. The second has not only periodic variations of velocity but also of the mass ejection rate. The fits take in account the $0.9c$ jet bulk velocity inferred by the calculations of Kuulkers et al. (1999) through multiple radio observations of the 1976 outburst.

In the first scenario the main outburst and a second smaller one after the first one are produced by independent fluid parcels with different conditions of speed variation through the parameter η^2 and mass rate ejection $\dot{m}$. For the second scenario, the main shock has an additional periodic variation in the mass ejection rate. The results are shown in the figures 3.5 and 3.6 show that it is possible to fit the 1976 with great accuracy.

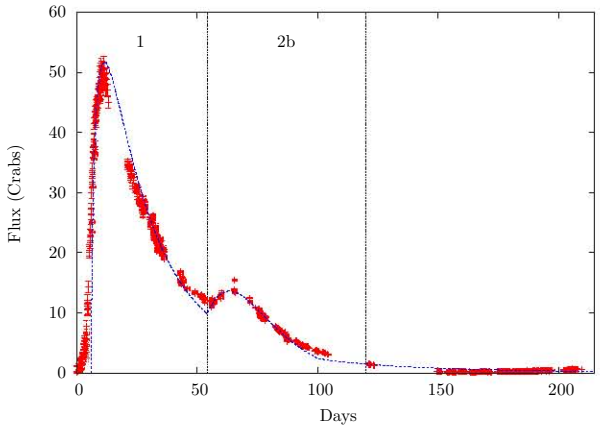

Figure 3.5: The figure shows a burst on the X-ray light curve of the microquasar A06200-00. The data was taken from Elvis et al. (1975) and Matilsky (1976) which was kindly provided by Jeffrey E. McClintock. The continuous curve on the plot is the best fit using the semi-analytical model of Mendoza et al. (2009) and described in section §3.1, using a linear fit to the data yields $\dot{m} = 3.27 \times 10^{-17} \mathrm{M}_{\odot}/\mathrm{yr}$ and $\omega = 200$ days. The second peak after the maximum is modelled as an increase in the discharge of $\dot{m} = 7.2 \times 10^{-14} \mathrm{M}_{\odot}/\mathrm{yr}$ at a time of 55 days with a duration of 45 days.

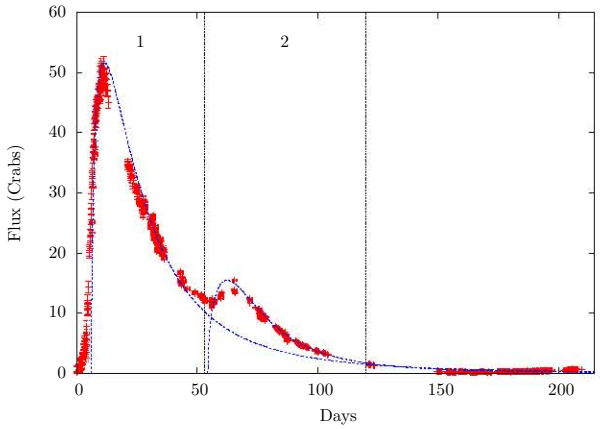

Figure 3.6: The figure shows a burst on the X-ray light curve of the microquasar A06200-00. The data was taken from Elvis et al. (1975) and Matilsky (1976) which was kindly provided by Jeffrey E. McClintock. The continuous curve on the plot is the best fit using the semi-analytical model of Mendoza et al. (2009) and described in section §3.1, using a linear fit to the data yields $\dot{m} = 3.27 \times 10^{-11} \mathrm{M}_{\odot}/\mathrm{yr}$ and $\omega = 200$ days. The second peak after the maximum is modelled as an additional oscillating velocity component at the day 55.

Hydrodynamics associated to the X-ray light curve of A0620-00.

Y. Coronado • S. Mendoza

Abstract From 1975 to 1976, an outburst was detected in the light curve of the X-ray transient A0620-00 using the Ariel V and SAS-3 experiments. In this letter we model the outburst with the hydrodynamical model proposed by Mendoza et al. (2009). The physical model is constructed assumming basic mass and momentum conservation laws associated to the motion of the shock waves developed inside the expanding relativistic jet of the source. These internal shock waves are produced as a result of periodic variations of the inyected mass and velocity of the flow at the base of the jet. The observations of this X-ray light curve present two clear bumps. The first one is modelled assuming periodic variations of the inyected velocity at the base of the jet, while the second one can either be modelled by further velocity oscillations, or by a periodic variation of the mass injection rate at the base of the jet at a latter time. The fitting of the data fixes different parameters of the model, such as the mean mass injection rate at the base of the jet and the oscillation frequency of the flow as measured on the rest frame of the central source.

Keywords – Relativistic processes – Hydrodynamics – X-rays: individual: A0620-00

1 Introduction

On August 3rd, 1975 the low-mass X-ray binary black hole transient A0620-00, exhibited its most powerful outburst detected by the Sky Survey Experiment on board the Ariel V satellite in X-rays (Elvis et al. 1975). On August 8th, this micro-quasar was also followed by the SAS-3 X-ray observatory (Matilsky et al. 1976). Subsequently it was also seen in different wavelengths, from radio to ultraviolet (see Kuulkers 1998, for a review). At that time, A0620-00 became the most powerful X-ray source in the sky for almost two months.

Five days after the discovery of A0620-00 intense variations on time scales of days, which reached a maximum value ~ 50 times that of the Crab Nebula in the energy interval of $1.5-6$ KeV, suggested that the source was an an excellent candidate for a stellar mass black hole with a stellar companion. This idea was further corroborated by the direct observations made by McClintock & Remillard (1986) which resolved the binary components of the source. The estimated distance to A0620-00 is ~ 1Kpc (Shahbaz et al. 1994), being one of the nearest X-ray transients objects, hosting a black hole with a mass function $f(m) = 3.18 \pm 0.16\, M_{\odot}$ (McClintock & Remillard 1986; Marsh et al. 1994).

Using dynamical and stellar numerical models, the inclination of the accretion disc with respect to the orbit spanned by the black hole and the stellar companion yields $i = 51^{\circ} \pm 0.9$, implying a black hole mass $6.6 \pm 0.25\, M_{\odot}$, and an estimated distance to the source 1.06 ± 0.12 Kpc (Cantrell et al. 2010).

The radio emission of A0620-00 was detected in 1975 (Davis et al. 1975; Owen et al. 1976a), with no jet resolved. Since many X-ray transient systems containing a black hole have radio emission that follows their X-ray outburst with clear detections of relativistic outflows or jets (Abdo et al. 2009), it was clear that a jet should have been produced in the X-ray outburst of A0620-00. Kuulkers et al. (1999) infered the existance of that jet by compiling different radio observations, concluding that the speed of the jet $\sim 0.9c$, where c is the velocity of light.

Y. Coronado

Instituto de Astronomía, Universidad Nacional Autónoma de México, AP 70-264, Distrito Federal 04510, México

S. Mendoza

Instituto de Astronomía, Universidad Nacional Autónoma de México, AP 70-264, Distrito Federal 04510, México

In this letter, we assume that the mechanism producing the observed light curve of A0620-00 is caused by variations in the injected flow at the base of the jet, which leads to the formation of shock waves that propagate along the jet. The hydrodynamical jet model presented in Mendoza et al. (2009, hereafter M09) describes the motion of working surfaces inside a relativistic jet, which are able to fit the observed light curves of long gamma-rays bursts (lGRBs) as well as the light curve of the blazar PKS 1510-089 (Cabrera et al. 2013). The shape of the X-ray light curve of the micro-quasar A0620-00 is similar to the one observed in lGRBs, showing an exponential rapid increase with a slow decay. With all these, the the physical ingredients of the phenomena that produces the light curve of A0620-00 can be considered similar to those ones ocurring in lGRB and on PKS 1510-089, but with different physical scales of energy, sizes, masses, accretion power rates, etc. (Mirabel & Rodriguez 2002).

The letter is organised as follows. In Section 2 we present the X-ray data of the light curve of A0620-00. In Section 3 we briefly describe the main features of the hydrodynamic model by M09, and using that model we fit the observational data in Section 4. Finally, the results of our fits and the discussion of the main physical parameters inferred by the modelling are presented in Section 5.

2 Observational data

The observational 1975-1976 X-ray light curve of the micro-quasar A0620-00 is shown in Figure 1 and was kindly provided by Jeffrey McClintock. It consist of a composition of two independent lightcurves obtained by Elvis et al. (1975) and Matilsky et al. (1976), with instruments on board Ariel V and SAS-3 respectively. Both data count-rates have been converted to flux Crab units, according to the instruments specifications (Whitlock et al. 1992). With this it is possible to get a complete light curve of the 1975-1976 outburst, including a bump in the decaying outburst. Figure 1 shows the plotted data on a linear scale, with the advantage of revealing the impressive outburst of 1975 and a clear second bump a few days after the maximum. To convert from Crabs to mJy, we use the conversion given by Kirsch et al. (2005) and Bradt et al. (1979) for the Ariel V data (in the energy range $1-13$ KeV) and the one in http://heasarc.gsfc.nasa.gov/docs/sas3 for the SAS-3 satellite (in the energy range $2-10$KeV). This conversion is coherent with the results obtained by Kirsch et al. (2005), for which 1Crab $\approx 2.4\times 10^{-11}\mathrm{Wm}^{-2}$ in the energy range $1-13$KeV.

In order to calculate the Luminosity L we multiply the obtained Flux F by $4\pi D^2\delta^{-p}$, where $\delta := 1/\Gamma(v_0)(1-(v_0/c)\cos\theta)$. For this particular case, since the inclination angle $i\approx 51^\circ$, then the angle θ between the jet and our line of sight is $\approx 39^\circ$, with a distance to the source $D=1\,\mathrm{Kpc}$ (Owen et al. 1976b; Shahbaz et al. 1994; Cantrell et al. 2010). The beaming index p for synchrotron radiation is 3 (Longair 2011) and we have chosen such value in accordance to the calculations of blazars and lGRBs (Wu et al. 2011; Mendoza et al. 2009; Cabrera et al. 2013), having in mind a unified radiative model for the flow inside all relativistic astrophysical jets. With this luminosity, and with the average jet bulk speed of $v_0=0.9c$ (Kuulkers et al. 1999), we are able to fit the observational data with the hydrodynamical model of M09.

Attempts to model the light curve of A0620-00 were made by Kuulkers et al. (1999) who noticed that this behaviour might well be understood modelling many "*synchrotron bubble*" ejections. Since micro-quasars are thought to be short scaled versions of quasars and are thus logical scaled counterparts of lGRB (Mirabel & Rodriguez 2002), it is quite natural to model their behaviour using the model by M09 to model their light curve. We thus assume that velocity and mass variations at the base of the jet of the micro-quasar A0620-00 produce internal shock waves that travel inside the expanding relativistic jet and that these shock waves in turn are able to reproduce its observed light curve.

3 The hydrodynamical model.

Many relativistic jets show internal shock waves, which are due to the interaction of the jet with inhomogeneities of the surrounding medium (see e.g Mendoza & Longair 2001), the bending of jets (see e.g Mendoza & Longair 2002) and time fluctuations in the velocity and mass of the ejected material (cf. Rees & Meszaros 1994; Jamil et al. 2008; Mendoza et al. 2009). In particular the semi-analytical model of M09 is a hydrodynamical description of time fluctuations at the base of the jet that develop shock waves inside an expanding relativistic jet.

The model of M09 produce internal shock waves by periodic oscillations of speed and mass discharge at the base of the jet. This mechanism injects fast fluid that overtakes slow one, producing an initial discontinuity which eventually forms a working surface expanding along the jet. The extra kinetic energy inside the working surface is thus radiated away. The efficiency converting factor between kinetic energy and observed radiation is assummed to be ~ 0.1 (see section 4), which

differs from the choice ~ 1 used by M09 and Cabrera et al. (2013) for lGRBs and the Blazar PKS1510-089. As we will discuss in section 5, the ~ 0.1 value yields physical parameters which are coherent with previous calculations.

Following M09, we assume that the flow is injected at the base of the jet with a periodic velocity v given by:

$$v(\tau) = v_0 + c\eta^2 \sin\omega\tau, \tag{1}$$

and a periodic mass injection rate:

$$\dot{m}(\tau) = \dot{m}_0 + \epsilon^2 \sin\Omega\tau, \tag{2}$$

where τ is the time measured in the proper frame of the source, the velocity v_0 is the "average" velocity of the flow inside the jet, and ω is the oscillation frequency of the flow. The positive constant parameters η^2 and ϵ^2 are obtained by fitting the observational data, with the particular feature that η^2 has to be sufficiently small so that the bulk velocity $v(\tau)$ does not exceed the velocity of light c. The mass injection rate $\dot{m}_0$ is the "average" discharge of the flow at the base of the jet, and Ω is its oscillation frequency.

4 Modelling the X-ray light curve

As previously discussed, the first outburst resembles the light curve of a typical lGRB. As such, we model that burst by assuming $\dot{m} = $ const., in complete accordance to the calculations by M09. The bump in the decay of the first burst is modelled in two ways. The first is by assuming a new ejection with constant discharge added up to the first outburst. The second way is by assuming an oscillating mass discharge $\dot{m}$ produced at a particular time while the first outburst decays.

In the first burst, where $\dot{m} =$ const., the semi-analytical model presented by M09, requires to know the values of v_0, η^2, ω and $\dot{m}$. The "mean" velocity value v_0 can be taken from observational data. For this particular case, we choose the inferred value from a wide variety of radio observations modelled through ejection mechanisms by Kuulkers et al. (1999) which yields a Lorentz factor $\Gamma(v_0) = 2.3$. Since the value of η^2 has to be small due to the expected variations inside the jet, we start with a small value of η^2 such that the bulk velocity of the flow $v(\tau = 0) \sim 0.1 \times v_0$. The velocity variations $v(\tau)$ are thus allowed to vary from this value up to the extreme upper limit $\Gamma(v(\tau)) \sim 10$. As pointed by M09, the mass ejection rate is related to the observed luminosity $L = \sigma\dot{m}c^2$ and is obtained directly from the fits of the light curve as will be discussed in what follows.

The second burst can be described by two different mechanisms: (a) The mass discharge $\dot{m}$ is kept constant and the velocity is the sum of the velocity as in equation (1) with an extra oscillating term $\eta'^2 \sin\omega'\tau$, with the same v_0, η^2 and ω used for the callibration of the first outburst. (b) The velocity is the same as the one used for the callibration of the first burst, and the mass discharge $\dot{m}$ is allowed to oscillate as in equation (2), with $\dot{m}_0$ given by the results obtained with the callibration of the first outburst.

Following Cabrera et al. (2013), we set a dimensionless system of units to perform the required fitting. To do so, the luminosity is measured in units of the peak luminosity and the time in units of the FWHM of each particular outburst. This system of units is such that for the first outburst $\omega = 1$ and $\dot{m} = 1$, with the only unknown η^2 obtained by a linear regression analysis to within 10% of accuracy. For the case of the second outburst: (a) The only unknown is η'^2 obtained with a further linear regression analysis. (b) The unknown quantity is ϵ^2 which can be obtained by another regression analysis. To return to the physical system of units one can recall at any particular step that the luminosity $L = \sigma\dot{m}c^2$, where σ is the efficiency conversion factor. For the case of micro-quasars, the bolometric luminosity L obtained from an accretion process onto a central object is given by: $L_{\rm acc} = f\eta\dot{m}_{\rm disc}c^2$, where η is the disc efficiency and f is the total accretion rate external to the radiating region which is not ejected in the jet or winds with fixed values of $\eta = 0.1$ (which is also used in the calculations by Gallo et al. (2006) and Esin et al. (1997)) and $f = 0.75$ (Körding et al. 2006). Since the jet power is supplied by the accretion power of the disc, it follows that (e.g. Falcke & Biermann 1995) $\dot{m} = \alpha\eta\dot{m}_{\rm disc}$, where $\alpha \leq 1$. We have chosen the maximum value $\alpha = 1$, which represents an upper bound to the radiated luminosity by the jet and yields no acretion power to possible existing winds. Note also that the time $t = \lambda^{-1}\tau$ with

$$\lambda = \begin{cases} \omega, & \text{first outburst,} \\ \omega', & \text{second outburst, case (a),} \\ \Omega, & \text{second outburst, case (b).} \end{cases}$$

5 Discussion

The results of the fits to the X-ray data presented in Section 2 using the model by M09 are shown in Figures 2 and 3. The obtained values for the physical

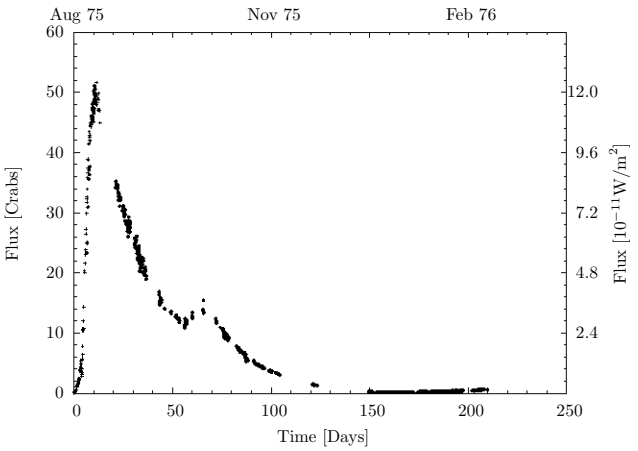

Fig. 1 The figure shows the X-ray light curve of the micro-quasar A0620-00. The crossess correspond to the Ariel V observations, which covers the uprise of the curve and the beginning of its decay. The points are SAS-3 observations, which cover the first outburst and the bump at the decaying of the burst.

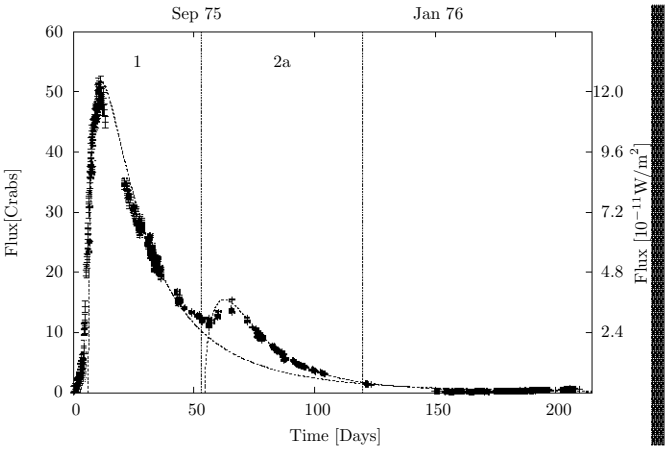

Fig. 2 The figure shows the fits to the X-ray light curve observations of the micro-quasar A0620-00, which corresponds to velocity variations and constant mass discharges for the first and second outburst (model (a) -see text). The second outburst has an additional oscillating velocity component as compared to the first one.

1st. outburst			
η^2/c	ω	$\dot{m}$	$\Gamma_{\max}$
10^{-3}	10^{-2}d	$10^{-11}M_{\odot}\mathrm{yr}^{-1}$	
1.679	6.6	2.2132	2.31
2nd. outburst - case (a)			
η'^2/c	ω'	$\dot{m}$	$\Gamma_{\max}$
10^{-3}	10^{-2}d	$10^{-11}M_{\odot}\mathrm{yr}^{-1}$	
0.061	249.1	0.6617	3.61
2nd. outburst - case (b)			
ϵ^2/c	Ω	$\dot{m}$	$\Gamma_{\max}$
$10^{-9}M_{\odot}\mathrm{y}^{-1}$	10^{-2}d	$10^{-11}M_{\odot}\mathrm{yr}^{-1}$	
0.8959	1.5	0.5888	2.31

Table 1 Obtained values for the free parameters of the model by M09 after fitting with X-ray observations of the light curve of the micro-quasar A062-00, accurate to within 10%. The background Lorentz factor of the bulk velocity of the flow was assumed to be 2.29. The maximum Lorentz factor of the flow in each outburst is represented by $\Gamma_{\max}$, and the minimum is $\sim 1.8 - 2.2$.

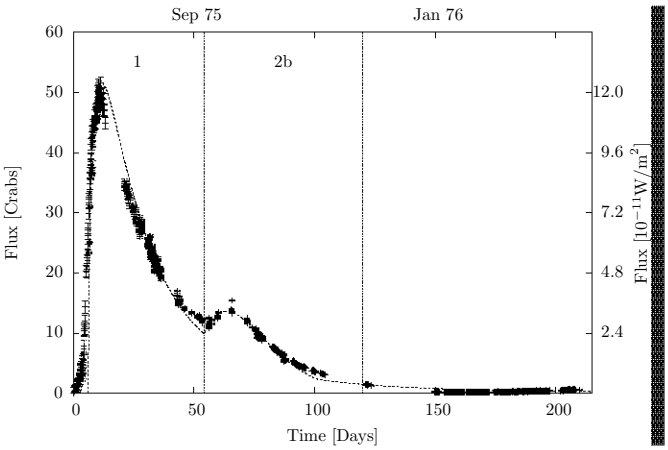

Fig. 3 The figure shows the fits to the X-ray light curve observations of the micro-quasar A0620-00, which corresponds to velocity variations for the first and second outburst, but with constant mass discharge at the first outburst and oscillating mass discharge at the second outburst (model (b) -see text).

parameters of the model are presented in Table 1. We have also included the maximum and minimum Lorentz factors, obtained for the bulk velocity of the flow. Direct inspection on the results of the Table show that $\dot{m} \sim 10^{-11} - 10^{-12} \mathrm{M}_{\odot} \mathrm{yr}^{-1}$, $\omega^{-1} \sim 0.01 - 2\,\mathrm{days}$ with a maximum Lorentz factor $2.3 - 3.6$. It is important to mention that the inferred mass ejection rates are of the same order of magnitude as the mass accretion rates obtained by Huang & Wheeler (1989) and McClintock et al. (1995). This means that the assumption $\alpha = 1$ with no power supplied to winds is a good assumption.

A00620-00 resulted to be an ideal target to test the model by Mendoza et al. (2009) since it closely resembles a lGRB in this outstanding outburst in x-rays. Future tests of the model have to be done with a wide variety of light curves from a large collection of microquasars.

6 Acknowledgements

The authors gratefully acknowledge the kindness of Jeffrey E. McClintock for providing the observational data and for pointing to the relevant articles discussing those observations. This work was supported a DGAPA-UNAM grant (PAPIIT IN111513-3). YUC and SM thank support granted by CONACyT: 210965 and 26344.

References

Abdo, A. A., Ackermann, M., Arimoto, M., et al. 2009, Science, 323, 1688

Bradt, H. V., Doxsey, R. E., & Jernigan, J. G. 1979, in X-ray Astronomy, ed. W. A. Baity & L. E. Peterson, 3–66

Cabrera, J. I., Coronado, Y., Benítez, E., et al. 2013, Mon. Not. R. Astron. Soc., 434, L6

Cantrell, A. G., Bailyn, C. D., Orosz, J. A., et al. 2010, Astrophys. J., 710, 1127

Davis, R. J., Edwards, M. R., Morison, J., & Spencer, R. E. 1975, Nature, 257, 659

Elvis, M., Page, C. G., Pounds, K. A., Ricketts, M. J., & Turner, M. J. L. 1975, Nature, 257, 656

Esin, A. A., McClintock, J. E., & Narayan, R. 1997, Astrophys. J., 489, 865

Falcke, H., & Biermann, P. L. 1995, Astron. Astrophys., 293, 665

Gallo, E., Fender, R. P., Miller-Jones, J. C. A., et al. 2006, Mon. Not. R. Astron. Soc., 370, 1351

Huang, M., & Wheeler, J. C. 1989, Astrophys. J., 343, 229

Jamil, O., Fender, R. P., & Kaiser, C. R. 2008, in Microquasars and Beyond

Kirsch, M. G., Briel, U. G., Burrows, D., et al. 2005, in Society of Photo-Optical Instrumentation Engineers (SPIE) Conference Series, Vol. 5898, UV, X-Ray, and Gamma-Ray Space Instrumentation for Astronomy XIV, ed. O. H. W. Siegmund, 22–33

Körding, E. G., Fender, R. P., & Migliari, S. 2006, Mon. Not. R. Astron. Soc., 369, 1451

Kuulkers, E. 1998, New Astron. Rev., 42, 1

Kuulkers, E., Fender, R. P., Spencer, R. E., Davis, R. J., & Morison, I. 1999, Mon. Not. R. Astron. Soc., 306, 919

Longair, M. S. 2011, High Energy Astrophysics

Marsh, T. R., Robinson, E. L., & Wood, J. H. 1994, Mon. Not. R. Astron. Soc., 266, 137

Matilsky, T., Bradt, H. V., Buff, J., et al. 1976, Astrophys. J. Lett., 210, L127

McClintock, J. E., Horne, K., & Remillard, R. A. 1995, Astrophys. J., 442, 358

McClintock, J. E., & Remillard, R. A. 1986, Astrophys. J., 308, 110

Mendoza, S., Hidalgo, J. C., Olvera, D., & Cabrera, J. I. 2009, Mon. Not. R. Astron. Soc., 395, 1403

Mendoza, S., & Longair, M. S. 2001, Mon. Not. R. Astron. Soc., 324, 149

—. 2002, Mon. Not. R. Astron. Soc., 331, 323

Mirabel, I. F., & Rodriguez, L. F. 2002, Sky Telesc., 103, 050000

Owen, F. N., Balonek, T. J., Dickey, J., Terzian, Y., & Gottesman, S. T. 1976a, Astrophys. J. Lett., 203, L15

—. 1976b, Astrophys. J. Lett., 203, L15

Rees, M. J., & Meszaros, P. 1994, Astrophys. J. Lett., 430, L93

Shahbaz, T., Naylor, T., & Charles, P. A. 1994, Mon. Not. R. Astron. Soc., 268, 756

Whitlock, L., Lochner, J., & Rhode, K. 1992, Legacy, 2, 25

Wu, Q., Zou, Y.-C., Cao, X., Wang, D.-X., & Chen, L. 2011, Astrophys. J. Lett., 740, L21

This manuscript was prepared with the AAS LaTeX macros v5.2.

§3.4 Blazar PKS 1510-089

In order to test the connection between different astrophysical jets such as Gamma-ray Blazars and long Gamma Ray Burst (lGRBs), a new model was considered to explain the high variability of the blazar in terms of the injection parameters at the base of the jet.

Among all the AGNs, the blazars, represent the most energetic ones, with the most powerful jets showing a highly variable spectral energy distribution (SED) in all the electromagnetic spectrum. The blazars, when considered as radio loud sources, are classified as BL Lac and flat-spectrum radio quasars -FRSQ. In particular PKS 1510-089 belongs to the last and is known to be one of the most powerful astrophysical objects in the universe, with highly relativistic jets pointing towards the observer's line of sight $\approx .4 - 3\,\mathrm{deg}$, displaying apparent superluminal velocities between 20c to 46c.

PKS 1510-089 was one of the sources detected by EGRET (Hartman et al., 1999), and was monitored at high energies by AGILE (D'Ammando et al., 2008; Pucella et al., 2009)and Fermi-LAT since 2008 (Tramacere, 2008; Ciprini & Corbel, 2009). It has also been observed by MAGIC and HESS (Wagner et al., 2010; Cortina, 2012). The light curve of PKS 1510-089 exhibits three prominent outbursts in γ-rays in the years 2008, 2009 and 2011. The last one shows a tremendous peak for almost a week. The high activity in gamma rays and detailed observations turns it into an excellent candidate to test the light curve to be modelled with Mendoza's et al. (2009) model.

We fitted the outburst by a new criteria in order to reduce the time of exploration in the space of parameters v_0, η^2, $\dot{m}$ and ω. The first assumption was to fit v_0 as the mean velocity inferred observations. The mass ejection rate $\dot{m}$ is then a free parameter used to adjust the luminosity of each outburst. The frequency ω is fixed to the Full Width at High Maximum (FWHM) of each outburst. Finally, the free parameter η^2 fitted by a statistical χ^2 criteria.

The fits reproduce the behaviour of all the PKS 1510-089 peaks very well over a 3σ statistical error and provide a range of parameters for the speed and mass ejection rate. Once the outburst were modelled, we made a luminosity integration over time for each burst to calculate the total energy contained in the outburst useful for a comparison with other astrophysical objects, mainly with the long GRB's. The resulting value of this released energy is $\sim 10^{39}$ – 10^{40} J, which shows the tremendous energy released by each individual outburst. This energy is to be compared with the energy released in about 10 s by a lGRB which is $\sim 10^{44}$ J.

The most energetic burst, recorded in 2011, injected a total mass of $\dot{m}\Delta t \sim 10^{-3}\,\mathrm{M}_{\odot}$ at the base of the jet, and lasted $\Delta t \sim$ 15days. Analysis of all bursts shows that the ejected mass interval is $10^{-5}M_{\odot} \lesssim m \lesssim 10^{-3}M_{\odot}$, for a time duration range such that 4days $\lesssim \Delta t \lesssim$ 30days.

The range of parameters for PKS 1510-089 are $\dot{m} \sim (2-25) \times 10^{-3}\mathrm{M}_{\odot}\mathrm{yr}^{-1}$, $\omega^{-1} \sim (0.3-2.6)\times 10^{3}\,\mathrm{s}$ and variations of the Lorentz factor $\Gamma \sim 10-380$ denote a scaling between the lGRB counterparts found by Mendoza et al. (2009) for which $\dot{m} \sim 10^{-1}-10^{-2}\mathrm{M}_{\odot}\mathrm{s}^{-1}$, $\omega^{-1} \sim$ 10s and $\Gamma \sim 50-500$. Note that the maximum and minimum values of the Lorentz factor for a particular outburst take into account the observational errors of the light curve. The real value lies between those calculated ranges. The inferred high relativistic Lorentz factors associated to the motion of the bulk velocity of the flow inside the PKS 1510-089 jet makes it an ideal candidate for the application of the hydrodynamical model of Mendoza et al. (2009). This is why that physical model can be applied naturally to lGRB and "in this particular case" to the extreme relativistic motion of the jet in the Blazar PKS 1510-089.

Monthly Notices of the ROYAL ASTRONOMICAL SOCIETY

MNRASL **434,** L6–L10 (2013) doi:10.1093/mnrasl/slt063
Advance Access publication 2013 June 18

A hydrodynamical model for the *Fermi*-LAT γ-ray light curve of blazar PKS 1510−089

J. I. Cabrera,[1⋆] Y. Coronado,[1⋆] E. Benítez,[1⋆] S. Mendoza,[1⋆] D. Hiriart[2⋆] and M. Sorcia[1⋆]

[1]*Instituto de Astronomía, Universidad Nacional Autónoma de México, AP 70-264, 04510 Distrito Federal, Mexico*
[2]*Instituto de Astronomía, Universidad Nacional Autónoma de México, AP 877, 22800 Ensenada, BC, Mexico*

Accepted 2013 May 13. Received 2013 April 30; in original form 2012 November 30

ABSTRACT

A physical description of the formation and propagation of working surfaces inside the relativistic jet of the blazar PKS 1510−089 are used to model its γ-ray variability light curve using *Fermi*-LAT data from 2008 to 2012. The physical model is based on conservation laws of mass and momentum at the working surface as explained by Mendoza et al. (2009). The hydrodynamical description of a working surface is parametrized by the initial velocity and mass injection rate at the base of the jet. We show that periodic variations on the injected velocity profiles are able to account for the observed luminosity, fixing model parameters such as mass ejection rates of the central engine injected at the base of the jet, oscillation frequencies of the flow and maximum Lorentz factors of the bulk flow during a particular burst.

Key words: galaxies: active – quasars: individual: PKS 1510–089 – gamma-rays: galaxies.

1 INTRODUCTION

Among all types of AGN, blazars (blazar class is defined as radio-loud sources conformed by the BL Lac objects and the flat-spectrum radio quasars – FSRQ; see e.g. Fossati et al. 1997; Ghisellini et al. 1998, and references therein) represent the most energetic class. They are known to have the most powerful jets (e.g. Lister et al. 2009) and also show a highly variable spectral energy distribution (SED) from the radio to the γ-rays wavelengths (see Abdo et al. 2010a; D'Ammando et al. 2011, and references therein).

The FSRQ PKS 1510−089 is known to be one of the most powerful astrophysical objects with a highly collimated relativistic jet that has shown apparent superluminal velocities between 20*c* to 46*c* and with a semi-angle aperture for the jet $\sim 0.^{\circ}2$ (Jorstad et al. 2005). Since the angle between the relativistic jet and the observer's line of sight $\sim 1.^{\circ}4$–3°, the jet almost coincides with the observer's line of sight (Homan et al. 2002; Marscher et al. 2010). PKS 1510−089 was one of the γ-ray sources detected by EGRET (Hartman et al. 1999). It has been monitored at high energies with *AGILE* (D'Ammando et al. 2008; Pucella et al. 2008; Lucarelli et al. 2012) and by *Fermi*-LAT and *AGILE* (Tramacere 2008; Ciprini & Corbel 2009; D'Ammando et al. 2009). It has also been studied with Major Atmospheric Gamma-ray Imaging Cherenkov Telescope (MAGIC) and High Energy Stereoscopic System (HESS; Wagner et al. 2010; Cortina 2012). The most prominent outbursts displayed by PKS 1510−089 were reported by Kataoka et al. (2008), Ciprini & Corbel (2009) and Orienti et al. (2013). The high activity observed in this source turns it into an ideal target for the physical study of its highly relativistic jet.

Precise models for the light curve (LC) produced by the outburst and flares from blazars are not done using directly the data variations observed in different wavelengths. Instead, models are applied to explain the behaviour of the SED (e.g. Abdo et al. 2010a; D'Ammando et al. 2011). Direct understanding of the LC requires a precise knowledge of the hydrodynamical behaviour of the relativistic flow. Mendoza et al. (2009, hereafter M09) have constructed a hydrodynamical model of the motion of a working surface inside a relativistic jet which is able to fit the observed LCs of long gamma-ray bursts (lGRBs). Since the jets in blazars are highly relativistic and their jet is nearly pointing towards the observer, similar to the jets observed in lGRBs, the physical ingredients of both phenomena can be considered the same but occurring at different physical scales of energy, sizes, masses, accretion rates, etc. (cf. Mirabel & Rodriguez 2002).

The blazar PKS 1510−089 is of tremendous importance since it exhibits extreme relativistic motions. As such, its energy curve must present luminosity variations and periods of extreme activity displayed as outbursts that, when physically modelled, can yield a better understanding of the physical parameters associated with the mechanism producing the observed luminosity.

In this Letter, we assume that the mechanism producing the observed LC in a typical lGRB is exactly the same that produces the variable LC of the blazar PKS 1510−089. We thus apply the

⋆E-mail: jcabrera@ciencias.unam.mx (JIC), coronado@astro.unam.mx (YC), erika@astro.unam.mx (EB), sergio@astro.unam.mx (SM), hiriart@astrosen.unam.mx (DH), msorcia@astro.unam.mx (MS).

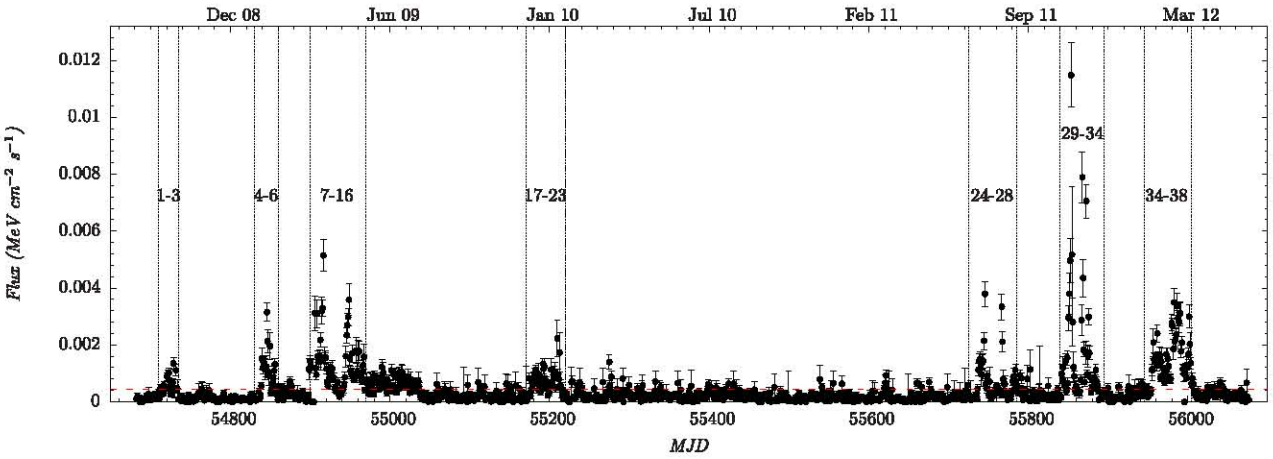

Figure 1. *Fermi*-LAT LC of blazar PKS 1510−089 (from 0.2 to 300 GeV) obtained from 2008 August to 2012 May. The outburst identification number (ID) labelled in the figure stands for the different flares selected in our work (see the text). The 3σ noise level is represented by the red horizontal dashed line.

hydrodynamical jet model presented in M09 to the LC variations displayed by the blazar PKS 1510−089 in the γ-ray domain, using public data obtained with the *Fermi*-LAT telescope.

The Letter is organized as follows. In Section 2, we explain in general terms the data reduction process. In Section 3, we describe the characteristics of our hydrodynamic model. The fit done to the data with the hydrodynamic model is explained in Section 4. The results of our fits and the discussion of the main physical parameters obtained in the modelling are presented in Section 5. Throughout this Letter, we use a standard cosmology with $H_0 = 71\,\mathrm{km\,s^{-1}\,Mpc^{-1}}$, $\Omega_\mathrm{m} = 0.27$ and $\Omega_\lambda = 0.73$ (see e.g Kataoka et al. 2008, and references therein).

2 *Fermi*-LAT DATA

The γ-ray fluxes were obtained in the range 0.2–300 GeV using the public data base of *Fermi*-LAT from 2008 August 08 to 2012 May 28. The data were reduced with the *Fermi* science tool package (see e.g. Atwood et al. 2009) in the same energy range, taking into account the diffuse Galactic background radiation, the instrument response matrix p7v6, and considering a zenith angle $<105^\circ$. We also calculated the active time of the detector and the point spread function. The γ-ray LC was constructed modelling the flux with a power law of the form $\mathrm{d}N/\mathrm{d}E = N_0(E/E_0)^\gamma$, with $\gamma = 2$–3 in accordance with the results of Abdo et al. (2010b). The fluxes and errors obtained with this package are given in photons $\times$ cm^{-2} s^{-1}. For further physical interpretation of the data, we have converted these fluxes and errors to MeV cm^{-2} s^{-1}.

The photons considered for analysis were taken from a region centred on the coordinates of PKS 1510−089 with a radius of 15°. Fig. 1 shows the γ-ray LC, with a bin size of 1 d. We chose these bins, since the errors are larger using shorter bin sizes, complicating the analysis of the data and because particular outbursts can be adequately resolved.

From Fig. 1, it follows that the source displayed the historical maximum outburst in MJD 558 51, corresponding to 2011 October 17 and reported by Hungwe, Dutka & Ojha (2011). Another important outburst occurred in MJD 548 99 (2009 March 9) and was observed with *AGILE* (D'Ammando et al. 2009). Several flares or outbursts can be observed in the LC. The most relevant events occurred in MJD 547 17 (2008 September 8), MJD 548 43 (2009 January 12), MJD 552 00 (2010 January 4; Benítez et al. 2011), MJD 557 30 (2011 June 18) and MJD 559 54 (2012 January 28). This last event was also observed by *AGILE* (Verrecchia et al. 2012) and MAGIC (Cortina 2012). Note that Marscher et al. (2010) report extra flares <200MeV during the period 548 50–549 50 MJD, which are not seen in our > 200MeV selection.

3 A HYDRODYNAMICAL MODEL FOR THE LC OF PKS 1510−089

The formation of internal shock waves on a relativistic jet are commonly explained by different mechanisms, such as the interaction of the jet with inhomogeneities of the surrounding medium, the bending of jets and time fluctuations in the parameters of the ejection (see e.g. Rees & Meszaros 1994; Mendoza & Longair 2002; Jamil, Fender & Kaiser 2008; M09). In particular, the model by M09 is a hydrodynamical description that can be applied to shock waves inside relativistic jets. This semi-analytical model describes the formation of a working surface inside a hydrodynamical jet due to periodic variations of the injected flow. When fast flow overtakes slow flow, an initial discontinuity is formed and a working surface (two shock waves separated by a contact discontinuity) is produced. The working surface travels along the jet and radiates away kinetic energy. The paper by M09 assumed that the efficiency converting factor is ∼1 and that it is mostly emitted in the γ-ray band. As explained in Section 1, the blazar PKS 1510−089 behaves as a scaled typical lGRB and as such, the hypothesis used by M09 can be extended to this particular object. As we will discuss in Section 5, this assumption is coherent with the physical properties found from the model. Following M09, we assume that flow is injected at the base of the jet with a periodic velocity given by

$$v(\tau) = v_0 + c\eta^2 \sin\omega\tau, \quad (1)$$

where τ is the time in the rest frame of the source, the velocity v_0 is the 'background' bulk velocity of the flow inside the jet and ω is the oscillation frequency. The positive constant parameter η^2 is chosen in such a way that oscillations of the flow are small so that the bulk velocity $v(\tau)$ of the flow does not exceed the velocity of light c. The mass ejection rate $\dot{m}(\tau)$ from the central engine which is injected at the base of the jet is assumed constant through a particular outburst event, but is allowed to vary from one outburst to another. The radiated energy of the flow as a function of time is calculated as the difference between the total energy E_0 injected at the base of the jet and the kinetic energy inside the working surface E_ws. The luminosity L is thus calculated as the derivative of this radiated

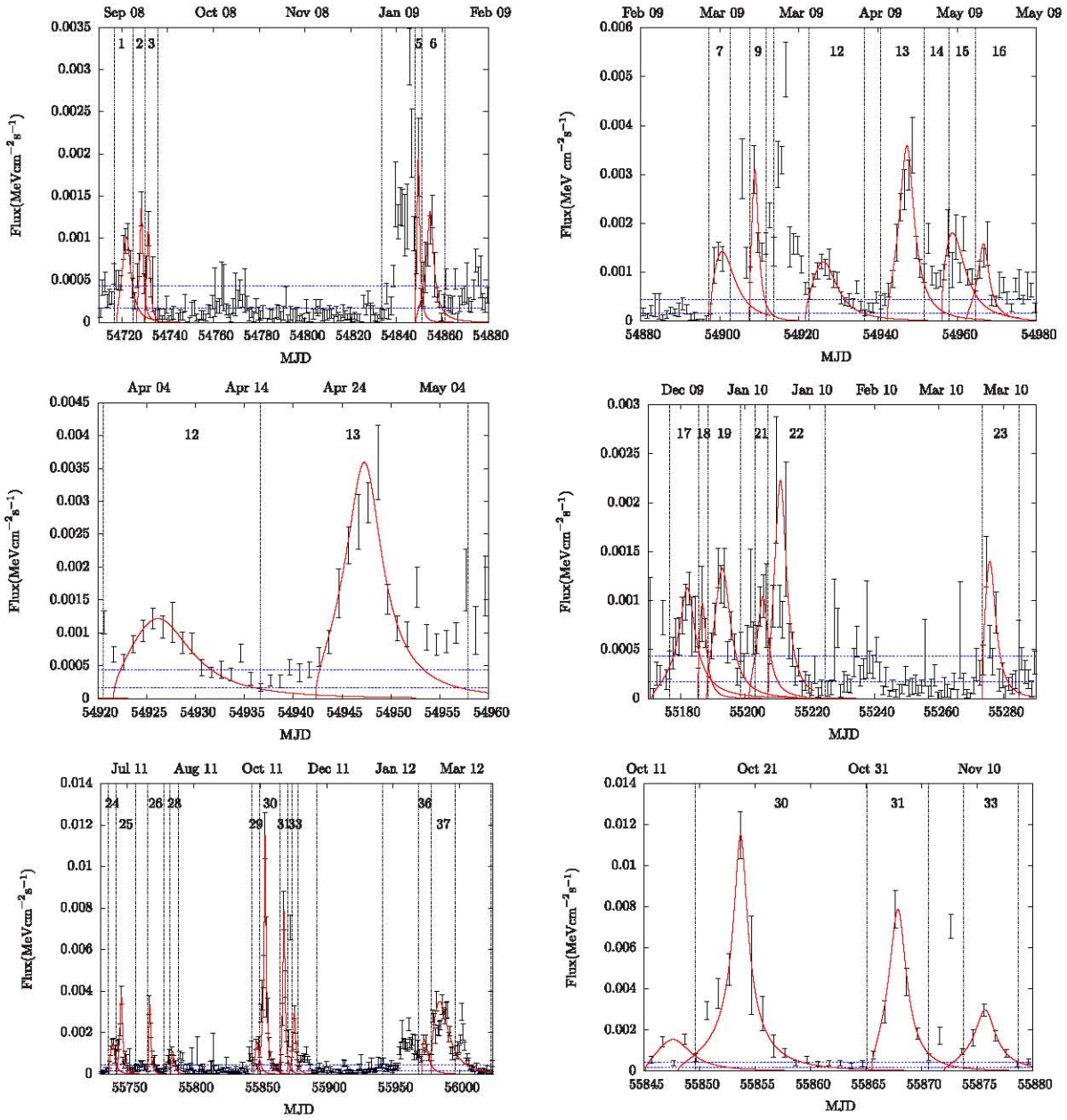

Figure 2. In each panel, the continuous red curve represents the fitting done to the LC of PKS 1580−089 with the semi-analytical model of internal shock waves (working surfaces) by M09. Blue horizontal dotted lines in all panels show the 1σ and 3σ noise levels. Top-left panel shows variations from 2008 September to 2009 February. Top-right panel shows variations from 2009 February to 2009 May. The central-left panel shows a zoom of the peaks 12 and 13. The central-right panel shows a few outbursts observed from 2009 December to 2010 March. Bottom-left panel shows recent variations occurred from 2011 July to 2012 March. Finally, bottom-right panel shows a zoom of the prominent October 2011 outburst. This outburst is approximately three times more luminous than the one observed in 2009 March. Up to now, this is the most violent outburst observed in the γ-ray waveband by *Fermi*.

energy with respect to time. As described by M09, there are two ways of calculating this luminosity curve. The first method consisted in a semi-analytical procedure and the second is performed with a full hydrodynamical numerical model. The authors showed that the semi-analytical model is in good agreement with the full numerical simulation, and as such we model the LC of PKS 1510−089 using their semi-analytical approach.

The semi-analytical approach is based on the assumption that equation (1) is valid and as such, one needs to know (or find through fits to observational data) the values of v_0, η^2, ω and $\dot{m}$. Furthermore, the mass ejection rate $\dot{m}$ enters in the description of the problem through the luminosity relation: $L \propto \dot{m}c^2$. The average bulk velocity v_0 must come from observational data [for this particular source, D'Ammando et al. (2008) reports a value $\Gamma(v_0) = 18$]. With this, the model is left with three free parameters: η^2, $\dot{m}$ and ω, which can be fixed by fitting the best theoretical LC to the observational data.

4 MODELLING THE γ-RAY LC

To model the LC of Fig. 1, we have selected the most conspicuous flares. The criterion used consists of selecting only those flares that are beyond 3σ noise level according to the errors shown in the LC.

By doing so, it turns out that 38 relevant peaks were chosen for our fitting.

As explained in Section 3, the model has four free parameters. The velocity parameter v_0 for this particular object is such that its Lorentz factor is $\Gamma(v_0) = 18$. To calculate the measured luminosity L from the observed flux F, we multiply the observed flux F by (Dermer 1995; Dermer & Menon 2009; Longair 2011; Ghisellini et al. 1993): $4\pi D_{\rm L}^2 \delta^{-p}$, where the relativistic beaming $\delta := 1/\Gamma(v_0)(1-(v_0/c)\cos\theta) \sim 18$, for a luminosity distance $D_{\rm L}$, which for this particular case is $D_{\rm L} = 1919$ Mpc and the angle $\theta \sim 1.^\circ 4$–3° is the angle between the jet and the observer's line of sight (cf. Section 1). We have selected a beaming index $p = 3$ in accordance with the results of Wu et al. (2011) for blazars and lGRBs.

The model presented by M09 is such that the theoretical luminosity and time are presented in a very particular system of units. To fit the best theoretical LC to the data, one needs to have a common system of units. To achieve this, we have normalized the 'measured' luminosity to its peak and the measured time to the full width at half-maximum (FWHM) of the measured LC. In order to compare with the theoretical model, the theoretical LC is also normalized to its peak and the time is normalized to the FWHM of the theoretical luminosity curve. Once both theoretical and measured LCs are in this common dimensionless system of units, this procedure allows us to fit the best theoretical LC by performing a χ^2 statistical test to find the optimal parameter η^2. Note that in this normalized system of units, the model only depends on one free parameter: η. Once the value of η is found, we can rescale back to physical units and in such a rescaling, the parameters $\dot{m}$ and ω are obtained, since according to M09, $L \propto \dot{m}c^2$ and $t \propto \omega^{-1}$. The luminosity fits are then transformed to the observed flux dividing them by $4\pi D_L/\delta^{3+\alpha}$. The results of these fits are shown in Fig. 2. The obtained values of the physical parameters of the model for each particular modelled outburst are presented in Table 1.

There is a certain subclass of outbursts that we do not model. These outbursts, labelled 8, 10, 20, 27 and 32 in Fig. 1, do not have enough data to allow us an accurate modelling. The outburst labelled 11 seems to have a fall that develops into a constant value before reaching an expected minimum and no data points further, so it seems incomplete. Outburst 14 has huge errors and the χ^2 statistical test does not converge. Outbursts 34 and 35 have large errors which also makes the modelling not accurate.

Table 1. Different physical quantities obtained for the outbursts modelled in this work. The background Lorentz factor of the bulk velocity of the flow was assumed to be 18. The first three columns from left to right are the date, numeric identification of the outburst (ID #) and the date corresponding to the maximum luminosity for a particular outburst. Columns four and six are the obtained values for the parameters η^2 (measured in units of the speed of light c) and the inverse frequency ω^{-1} relevant to the particular variational model of equation (1). Column five corresponds to the maximum upper limit of the Lorentz factor of the flow for each particular outburst. The minimum Lorentz factor of the flow for all outbursts is ∼12–13. Column seven represents the mass injection rate $\dot{m}$ of the flow at the base of the jet. The values of all inferred parameters are accurate to within 10 per cent.

Date	ID number	MJD +540 00	η^2/c 10^{-3}	$\Gamma_{\rm max}$	ω^{-1} 10^3 s	$\dot{m}$ $10^{-3}\,{\rm M}_\odot\,{\rm yr}^{-1}$
08 Sep	1	722.66	1.500	106	1.05	2.16
08 Sep	2	728.66	1.520	143	0.50	2.87
08 Sep	3	731.66	1.510	120	0.41	2.37
09 Jan	5	849.66	1.501	107	0.34	4.18
09 Jan	6	855.66	1.533	209	1.49	2.80
09 Mar	7	899.66	1.330	48	0.94	3.04
09 Mar	9	908.66	1.460	76	0.37	6.61
09 Apr	12	925.66	1.430	66	1.27	2.60
09 Apr	13	948.66	1.515	130	1.22	7.67
09 May	15	957.66	1.300	45	0.88	3.85
09 May	16	967.66	1.523	152	1.05	3.38
09 Dec	17	1182.66	1.534	219	2.60	2.40
09 Dec	18	1186.66	1.400	58	0.39	2.06
09 Dec	19	1191.66	1.488	94	1.24	2.84
10 Jan	21	1205.66	1.510	120	1.04	2.23
10 Jan	22	1209.66	1.493	98	0.95	4.76
10 Mar	23	1274.66	1.430	66	0.68	2.99
11 Jun	24	1739.66	1.460	76	0.74	3.16
11 Jul	25	1745.66	1.527	169	0.81	8.09
11 Jul	26	1766.66	1.469	81	0.36	7.13
11 Aug	28	1783.66	1.380	55	0.41	2.40
11 Oct	29	1848.66	1.460	76	0.67	3.30
11 Oct	30	1853.66	1.541	383	1.32	24.52
11 Nov	31	1867.66	1.522	149	0.57	16.83
11 Nov	33	1875.66	1.531	193	0.88	6.37
12 Feb	36	1972.66	1.220	39	0.66	3.55
12 Mar	37	1982.66	1.350	50	2.03	7.48

5 DISCUSSION

We have modelled the LC of blazar PKS 1510−089 for almost 4 years using the hydrodynamical model of M09. The modelling was performed by assuming a periodic velocity injection mechanism at the base of the relativistic jet that leads to the formation of a working surface and is capable of losing energy as it travels along the jet. As explained in Section 3, the model by M09 was constructed to deal with LCs of lGRB. However, the blazar PKS 1510−089 has many physical characteristics to be considered a geometrical large scaled version of an lGRB since it has a highly relativistic jet that points towards the observer. The results presented in Table 1 show high upper limits for the bulk Lorentz factors achieved with oscillations of the flow, that reach values as large as $\lesssim$380 for one particular event. These inferred huge Lorentz factors in the bulk velocity oscillation of this blazar show another close similarity with lGRBs.

The range of parameters as presented in Table 1, i.e. $\dot{m} \sim (2\text{–}25) \times 10^{-3}\,{\rm M}_\odot\,{\rm yr}^{-1}$, $\omega^{-1} \sim (0.3\text{–}2.6) \times 10^3$ s and variations of the Lorentz factor $\Gamma \sim$ 10–380, denote a scaling between the lGRB counterparts found in M09 for which $\dot{m} \sim 10^{-1}$–$10^{-2}\,{\rm M}_\odot\,{\rm s}^{-1}$, $\omega^{-1} \sim$ 10s and $\Gamma \sim$ 50–500. Note that the maximum and minimum values of the Lorentz factor for a particular outburst take into account the observational errors of the LC. The real value lies in between those calculated ranges. The inferred high relativistic Lorentz factors associated with the motion of the bulk velocity of the flow inside the jet of PKS 1510−089 makes it an ideal candidate for the application of the hydrodynamical model of M09. This is why that physical model can be applied naturally to lGRB and in this particular case to the extreme relativistic motion of the jet in the blazar PKS 1510−089. The energy released in each outburst can be calculated by taking the integral of the luminosity with respect to time, which occurs typically over periods of a few days. The value of this released energy is $\sim 10^{39}$–10^{40} J, which shows the tremendous energy released by each individual outburst. This energy is to be compared with the energy released in about 10 s by an lGRB which is $\sim 10^{44}$ J.

The most energetic burst, labelled 30, injected at the base of the jet a total mass $m = \dot{m}\Delta t \sim 10^{-3}\,{\rm M}_\odot$ while the burst lasted $\Delta t \sim$ 15 d. Analysis of all bursts shows that the ejected mass interval is $10^{-5}\,{\rm M}_\odot \lesssim m \lesssim 10^{-3}\,{\rm M}_\odot$, for a time duration range 4 d $\lesssim \Delta t \lesssim$ 30 d.

The variations of the injected flow at the base of the jet cause the formation of working surfaces that produce bursts of γ-rays in the structure of the jet. The physical mechanism producing the oscillations of the input flow, which allows fast fluid to overtake the slow one, leading to the formation of working surfaces, is beyond the scope of this Letter. However, steady flow deviations and oscillations in such complicated phenomena are expected since the accretion–ejection mechanism associated with a particular object is not necessarily expected to be of constant velocity and mass accretion–ejection rates.

It is important to note that the assumption of seeing a blazar as a scaled version of an lGRB is not new. In an early attempt to find a unified model of jet and central-engine power, Mirabel & Rodriguez (2002) made this identification. The more relativistic a blazar jet is, the more it will resemble an lGRB. The idea of having a unified physical model for all types of astrophysical jets was first suggested by the pioneering works for the astrophysical scaling laws of black holes by Sams, Eckart & Sunyaev (1996) and Rees (1998). The work presented in this Letter further strengthens arguments about a unified picture of all astrophysical relativistic jets.

PKS 1510−089 resulted to be an ideal target to test the model by M09 since it closely resembles an lGRB in some of its outbursts. Future tests of the model have to be done with a wide variety of LCs from a large collection of blazars and microquasars.

ACKNOWLEDGEMENTS

We thank the anonymous referee for his valuable comments who helped us to produce a much improved version of our Letter. This work was supported by three DGAPA-UNAM grants (PAPIIT IN116210-3, IN116211-3, IN111513-3). JIC acknowledges support given by IAUNAM as a visiting researcher. JIC, YUC, EB, SM, DH and MS thank support granted by CONACyT: 50102, 210965, 13654, 26344, 8366, 177304. We acknowledge the use of the *Fermi*-LAT publicly available data as well as the public data reduction software.

REFERENCES

Abdo A. A. et al., 2010a, ApJ, 716, 30
Abdo A. A. et al., 2010b, ApJ, 721, 1425
Atwood W. B. et al., 2009, ApJ, 697, 1071
Benítez E. et al., 2011, Rev. Mex. Astron. Astrofis. Ser. Conf., 40, 44
Ciprini S., Corbel S., 2009, Astron. Telegram, 1897, 1
Cortina J., 2012, Astron. Telegram, 3965, 1
D'Ammando F. et al., 2008, Astron. Telegram, 1436, 1
D'Ammando F. et al., 2009, A&A, 508, 181
D'Ammando F. et al., 2011, A&A, 529, A145
Dermer C. D., 1995, ApJ, 446, L63
Dermer C. D., Menon G., 2009, High Energy Radiation from Black Holes: Gamma Rays, Cosmic Rays, and Neutrinos. Princeton Univ. Press, Princeton, NJ
Fossati G., Celotti A., Ghisellini G., Maraschi L., 1997, in Ostrowski M., Sikora M., Madejski G., Begelman M., eds, Relativistic Jets in AGNs. p. 245
Ghisellini G., Padovani P., Celotti A., Maraschi L., 1993, ApJ, 407, 65
Ghisellini G., Celotti A., Fossati G., Maraschi L., Comastri A., 1998, MNRAS, 301, 451
Hartman R. C. et al., 1999, ApJS, 123, 79
Homan D. C., Wardle J. F. C., Cheung C. C., Roberts D. H., Attridge J. M., 2002, ApJ, 580, 742
Hungwe F., Dutka M., Ojha R., 2011, Astron. Telegram, 3694, 1
Jamil O., Fender R. P., Kaiser C. R., 2008, Proc. VII Microquasar Workshop: Microquasars and Beyond. Microquasars and Beyond, Available at: http://pos.sissa.it/cgi-bin/reader/conf.cgi?confid=62
Jorstad S. G. et al., 2005, AJ, 130, 1418
Kataoka J. et al., 2008, ApJ, 672, 787
Lister M. L., Homan D. C., Kadler M., Kellermann K. I., Kovalev Y. Y., Ros E., Savolainen T., Zensus J. A., 2009, ApJ, 696, L22
Longair M. S., 2011, High Energy Astrophysics. Cambridge Univ. Press, Cambridge
Lucarelli F. et al., 2012, Astron. Telegram, 3934, 1
Marscher A. P. et al., 2010, ApJ, 710, L126
Mendoza S., Longair M. S., 2002, MNRAS, 331, 323
Mendoza S., Hidalgo J. C., Olvera D., Cabrera J. I., 2009, MNRAS, 395, 1403 (M09)
Mirabel I. F., Rodriguez L. F., 2002, Sky Telesc., 103, 050000
Orienti M. et al., 2013, MNRAS, 428, 2418
Pucella G. et al., 2008, A&A, 491, L21
Rees M. J., 1998, in Wald R. M., ed., Black Holes and Relativistic Stars. University of Chicago Press, Chicago, p. 79
Rees M. J., Meszaros P., 1994, ApJ, 430, L93
Sams B. J., Eckart A., Sunyaev R., 1996, Nat, 382, 47
Tramacere A., 2008, Astron. Telegram, 1743, 1
Verrecchia F. et al., 2012, Astron. Telegram, 3907, 1
Wagner S. J., Behera B., H.E.S.S. Collaboration, 2010, High Energy Astrophysics Division #11, #7.05. BAAS, 41, 660
Wu Q., Zou Y.-C., Cao X., Wang D.-X., Chen L., 2011, ApJ, 740, L21

This paper has been typeset from a TEX/LATEX file prepared by the author.

Chapter 4

Analytical solution to a working surface

The use of a semi-analytical models include a series of approximations that, during a first handling of the problem, gives us an idea of the scaling relations between the jets at different scales. Here we present an analytical model to describe the working surface without the classical thin layer approximation used in astrophysics and allows to describe the evolution of a pair of shock waves separated by a contact surface, i.e., a working surface at non-relativistic speed.

Hydrodynamical model

§4.1 Model

In most of the hydrodynamical models the thin layer approximation defines an infinitesimal thin working surface, i.e., two shock waves with a contact discontinuity inside them. In the present work we solve the problem without an approximation, using different systems of reference in order to describe a working surface in terms of the jet and surrounding hydrodynamical variables.

We define three systems of reference for the working surface, the first one acts as an auxiliary system which considers two stationary shock waves moving in opposite directions towards the contact discontinuity at both sides of them. The second is fixes the contact discontinuity leading both shock waves to move away from the fixing point. The last one

describes a working surface moving inside of a medium with speed zero.

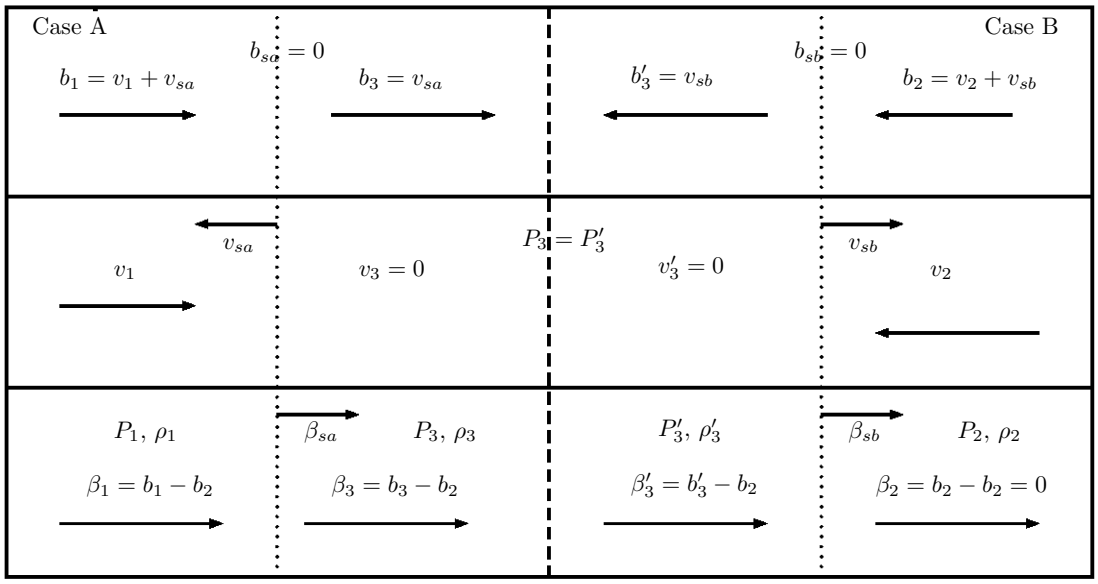

Figure 4.1: Systems of reference for a working surface, where the arrows indicate the directions of the flow or shock wave, the dotted lines are the shock waves and the dashed line stands for the contact discontinuity. The top panel shows a static working surface centred on the contact discontinuity. The middle panel presents two static shock waves towards the center, which we divide in to two isolated cases. The bottom panel corresponds to a working surface moving inside a stationary medium.

In order to obtain the hydrodynamical variables over the third system of reference, we first use the system of reference with the two cases taken as separate problems, naming the left and right shock by the case **A** and **B** respectively.

§4.1.1 Case A

Although there are in the literature different approaches to the problem of a working surface travelling inside a jet, we describe this via the jet and ambient hydrodynamical variables.

Case A corresponds to the left shock, see 4.1. The shock is stationary and we use the expressions given by Landau, following their notation and using a sub index 1 for the pre-shock conditions (jet conditions) and 3 for post-shock conditions.

$$b_3^2 = \frac{1}{2}(c_{s3}^2/\kappa)\left[\kappa - 1 + (\kappa+1)P_1/P_3\right], \tag{4.1}$$

$$b_1^2 = \frac{1}{2}(c_{s3}^2/\kappa)\left[\kappa - 1 + (\kappa+1)P_3/P_1\right], \tag{4.2}$$

where κ is the ratio of specific heats at constant pressure and constant volume, and c_{si} is the speed of sound of the particular region i. Starting with the continuity equation, we solve for the velocity ratio given by Landau & Lifshitz (1995) equations (89.6) and (89.7):

$$\frac{\rho_3}{\rho_1} = \frac{b_1}{b_3} = \frac{(\kappa+1)M_1^2}{(\kappa-1)M_1^2+2}, \tag{4.3}$$

$$\frac{P_3}{P_1} = \frac{2\kappa M_1^2}{\kappa+1} - \frac{\kappa-1}{\kappa+1}, \tag{4.4}$$

$$\frac{T_3}{T_1} = \frac{\left[2\kappa M_1^2 - (\kappa-1)\right]\left[(\kappa-1)M_1^2+2\right]}{(\kappa-1)^2 M_1}, \tag{4.5}$$

where the Mach number for the region 3 is $M_3 = v_3/c_{s3}$. Then we solve for M_1

$$M_3^2 = \left[\frac{2+M_1^2(\kappa-1)}{2\kappa M_1^2 - (\kappa-1)}\right]. \tag{4.6}$$

Solving for ρ_3, P_3 and b_3 using (4.3) and (4.4) we obtain.

$$\rho_3 = \left[\frac{(\kappa+1)M_1^2}{(\kappa-1)M_1^2+2}\right]\rho_1, \tag{4.7}$$

$$P_3 = \left[\frac{2\kappa M_1^2 - (\kappa-1)}{\kappa+1}\right]P_1, \tag{4.8}$$

$$b_3 = \left[\frac{2+M_1^2(\kappa-1)}{M_1^2(\kappa+1)}\right]b_1, \tag{4.9}$$

§4.1.2 Case B

We repeat the same procedure with the shock at the right side, identifying the post-shock and pre-shock (ambient conditions) regions as 3' and 2 respectively. Using the relations for the velocity in a shock wave equation (89.4) from Landau & Lifshitz (1995), for both

regions:

$$b_2^2 = \frac{1}{2}(c_{s2}^2/\kappa)\left[\kappa - 1 + (\kappa+1)P_3'/P_2\right], \tag{4.10}$$

$$b_3'^2 = \frac{1}{2}(c_{s2}^2/\kappa)\left[\kappa - 1 + (\kappa+1)P_2/P_3'\right], \tag{4.11}$$

from the continuity equation we solve for the velocity ratio given by Landau & Lifshitz (1995) equations (89.6) and (89.7):

$$\frac{\rho_3'}{\rho_2} = \frac{b_2}{b_3'} = \frac{(\kappa+1)M_2^2}{(\kappa-1)M_2^2+2}, \tag{4.12}$$

$$\frac{P_3'}{P_2} = \frac{2\kappa M_2^2}{\kappa+1} - \frac{\kappa-1}{\kappa+1}, \tag{4.13}$$

$$\frac{T_3'}{T_2} = \frac{\left[2\kappa M_2^2 - (\kappa-1)\right]\left[(\kappa-1)M_2^2+2\right]}{(\kappa-1)^2 M_2}, \tag{4.14}$$

where the Mach number for the region 2 is $M_2 = b_2/c_{s2}$. Then we solve for M_3'

$$M_3'^2 = \frac{2+(\kappa-1)M_2^2}{2\kappa M_2^2 - (\kappa-1)}, \tag{4.15}$$

solving for $\rho_{\prime 3}$, P_3' and b_3' using (4.12) and (4.13) we obtain.

$$P_3' = \left[\frac{2\kappa M_2^2 - (\kappa-1)}{\kappa+1}\right] P_2, \tag{4.16}$$

$$b_3' = \left[\frac{(\kappa-1)M_2^2+2}{(\kappa+1)M_2^2}\right] b_2, \tag{4.17}$$

$$\rho_{\prime 3} = \left[\frac{(\kappa+1)M_2^2}{(\kappa-1)M_2^2+2}\right] \rho_2, \tag{4.18}$$

§4.2 Coordinate transformations.

The transformations of coordinates between the different systems of reference allows us to express the hydrodynamical variables in terms of a full moving system. The velocities on the shock rest frame are b_1, b_2, b_3 and b_3', for the working surface rest frame v_1, v_2, v_3 and v_3' and, finally for the moving working surface or ambient medium rest frame, β_1, β_2, β_3 and β_3'.

$$\beta_1 = b_1 - b_2, \tag{4.19}$$
$$\beta_2 = b_2 - b_2, \tag{4.20}$$
$$\beta_3 = b_3 - b_2, \tag{4.21}$$
$$\beta_3' = b_3' - b_2, \tag{4.22}$$
$$\beta_{sa} = \beta_3 - \beta_1, \tag{4.23}$$
$$\beta_{sb} = \beta_3' - \beta_2, \tag{4.24}$$
$$b_1 = v_1 + v_{sa}, \tag{4.25}$$
$$b_2 = -(v_2 + v_{sb}), \tag{4.26}$$
$$b_3 = v_{sa}, \tag{4.27}$$
$$b_3' = v_{sb}, \tag{4.28}$$
$$b_{sa} = 0, \tag{4.29}$$
$$b_{sb} = 0, \tag{4.30}$$
$$v_3 = 0, \tag{4.31}$$
$$v_3' = 0, \tag{4.32}$$

Using (4.9) and substituting (4.6), and then solving for M_3 we obtain the following for the case **A**

$$b_1/b_3 = \frac{(\kappa-1)M_3^2 + 2}{(\kappa+1)M_3^2} \tag{4.33}$$

Then, using the relation (4.27) between the shock velocity v_{sa} and the fluid velocity b_3, we could exchange the speed on the Mach number $M_3 = b_3/c_{s3}$, where c_{s3} is the speed of sound in the third region.

Using the relations (4.3), (4.25) and (4.27)

$$\frac{b_1}{b_3} = \frac{v_1 + v_{sa}}{v_{sa}} = \left(\frac{(\kappa+1)M_{sa}^2}{(\kappa-1)M_{sa}^2+2} \right)^{-1},$$
$$\frac{v_1 + v_{sa}}{v_{sa}} = \left(\frac{(\kappa+1)(v_{sa}/c_{sa})^2}{(\kappa-1)(v_{sa}/c_{sa})^2+2} \right)^{-1} \Longrightarrow v_{sa}^2 + v_{sa}\left(v_1\frac{\kappa+1}{2}\right) - c_{sa}^2,$$

Solving for case **A**'s shock velocity we obtain:

$$vsa = -\frac{(\kappa+1)v_1}{4} \pm \frac{\sqrt{\left[(\kappa+1)v_1\right]^2 + 16c_{sa}^2}}{4}, \tag{4.34}$$

Where c_{sa} is the speed of sound of the region three.

For the case **B** we rearrange the equations (4.12) and (4.15) in order to obtain the primed speed ratio of the second and third regions in terms of the Mach number M_3'.

$$\frac{b_2}{b_3'} = \frac{(\kappa-1)M_3'^2+2}{(\kappa+1)M_3'^2}, \tag{4.35}$$

Then, using relation (4.28) between the shock velocity v_{sb} and the fluid velocity b_3', we exchange the speed on the Mach number $M_3' = b_3'/c_{s3}'$, where c_{s3}' is the speed of sound in the primed third region.

Using relations (4.12), (4.26) and (4.28)

$$\frac{b_2}{b_3'} = \frac{v_2 + v_{sb}}{v_{sb}} = \frac{(\kappa-1)M_{sb}^2+2}{(\kappa+1)M_{sb}^2},$$
$$\frac{v_2}{v_{sb}} + 1 = \frac{(\kappa-1)(v_{sb}/c_{sb})^2+2}{(\kappa+1)(v_{sb}/c_{sb})^2} \Longrightarrow v_{sb}^2 + v_{sb}\left(v_2\frac{\kappa+1}{2}\right) - c_{sb}^2,$$

Solving the system for v_{sb}, we get:

$$v_{sb} = -\frac{v_2(\kappa+1)}{4} \pm \frac{\sqrt{\left[v_2(\kappa+1)\right]^2 + 16c_{sb}^2}}{4}, \tag{4.36}$$

Where c_{sb} is the speed of sound of the primed third fluid.

The next step is to find the variables of the working surface P_3, ρ_3, P_3' and ρ_3'in terms of injected and ambient variables. In order to do this, we use the condition for a contact surface on the rest frame working surface, ($P_3' = P_3$). Using equations (4.8) and (4.16) we

get:

$$P_1\left[\frac{2\kappa M_1^2-(\kappa-1)}{\kappa+1}\right]=\left[\frac{2\kappa M_2^2-(\kappa-1)}{\kappa+1}\right]P_2, \tag{4.37}$$

$$\Longrightarrow M_2=\frac{\sqrt{\frac{2\,M_1^2P_1}{P_2}+\frac{P_1}{\kappa P_2}-\frac{P_1}{P_2}-\frac{1}{\kappa}+1}}{\sqrt{2}}, \tag{4.38}$$

From the expression (4.19) we could obtain a relation between the Mach number at the first and second shocks that constitute the working surface.

$$\begin{aligned}\beta_1&=b_1-b_2,\\ \frac{\beta_1}{c_{s1}}&=\frac{b_1-b_2}{c_{s1}},\\ m_1&=M_1-\frac{b_2}{c_{s1}},\\ m_1=M_1-M_2\frac{c_{s2}}{c_{s1}}&\Longrightarrow M_2=(M_1-m_1)\,\frac{c_{s1}}{c_{s2}},\end{aligned}$$

Using (4.38) and the previous expression, we solve for M_1.

$$M_1=\frac{2{c_{s1}}^2\kappa m_1P_2}{2{c_{s1}}^2\kappa P_2-2{c_{s2}}^2\kappa P_1}\pm\sqrt{2}c_{s2}\cdot \frac{\left[\left({c_{s1}}^2\kappa^2-{c_{s1}}^2\kappa\right)P_2{}^2+\left(2{c_{s1}}^2\kappa^2{m_1}^2+\left(-{c_{s2}}^2-{c_{s1}}^2\right)\kappa^2+\left({c_{s2}}^2+{c_{s1}}^2\right)\kappa\right)P_1P_2+\left({c_{s2}}^2\kappa^2-{c_{s2}}^2\kappa\right)P_1{}^2\right]^{1/2}}{2{c_{s1}}^2\kappa P_2-2{c_{s2}}^2\kappa P_1}, \tag{4.39}$$

Substituting in (4.38), we solve for M_2,obtaining a final expressions of the Mach number in terms or the injected and ambient hydrodynamical variables $\beta 1$, P_1, ρ_1 and $\beta_2=0$, P_2, ρ_2, respectively.

Substituting the pressure and density obtained on the shock rest frame on (4.25), and (4.26) and solving for v_1 and v_2, we obtain:

$$v_1 = \sqrt{p_3 - p_1}\sqrt{(1/\rho_1) - (1/\rho_3)}, \tag{4.40}$$

$$v_2 = -\sqrt{p_3 - p_2}\sqrt{(1/\rho_2) - (1/\rho_3')}, \tag{4.41}$$

from now on we substitute equations (4.8), (4.7), (4.16) and (4.18) on expressions (4.40) and (4.41), stated in terms of Mach numbers M_1 and M_2.

$$v_1 = \sqrt{\frac{2M_1^2 - 2}{(\kappa+1)\rho_1 M_1^2}}\sqrt{\frac{(2\kappa M_1^2 - 2\kappa)P_1}{(\kappa+1)M_1^2}}, \tag{4.42}$$

$$v_2 = -\sqrt{\frac{2M_2^2 - 2}{(\kappa+1)\rho_2 M_2^2}}\sqrt{\frac{(2\kappa M_2^2 - 2\kappa)P_2}{(\kappa+1)M_2^2}}, \tag{4.43}$$

We obtain the velocities of the working surface on the moving frame β_3 and β_3' from the equations (4.21), (4.22), and (4.27)-(4.30).

$$\beta_3 = b_1 - v_1 - b_1 + \beta_1 = \beta_1 - v_1 = \beta_1 - \sqrt{\frac{2M_1^2 - 2}{(\kappa+1)\rho_1 M_1^2}}\sqrt{\frac{(2\kappa M_1^2 - 2\kappa)P_1}{(\kappa+1)M_1^2}}, \tag{4.44}$$

$$\beta_3' = b_2 - v_2 - b_2 = -v_2 = \sqrt{\frac{2M_2^2 - 2}{(\kappa+1)\rho_2 M_2^2}}\sqrt{\frac{(2\kappa M_2^2 - 2\kappa)P_2}{(\kappa+1)M_2^2}}, \tag{4.45}$$

$$\beta_3' = b_3' + v_2 + b_3' = v_2 + 2v_{sb}, \tag{4.46}$$

Solving for P_3 from equation (4.40):

$$p_3 = \frac{v_1^2}{\rho_1^{-1} - \rho_3^{-1}} + p_1, \tag{4.47}$$

$$p_3 = \frac{v_1^2}{\frac{2M_1^2-2}{(\kappa+1)\rho_1 M_1^2}} + p_1, \tag{4.48}$$

$$p_3 = \frac{\frac{2M_1^2-2}{(\kappa+1)\rho_1 M_1^2}\frac{(2\kappa M_1^2-2\kappa)P_1}{(\kappa+1)M_1^2}}{\frac{2M_1^2-2}{(\kappa+1)\rho_1 M_1^2}} + p_1, \tag{4.49}$$

$$p_3 = \frac{2\kappa M_1^2 + P_1[M_1^2(\kappa+1) - 2\kappa]}{(\kappa+1)M_1^2}, \tag{4.50}$$

since the conditions over the contact surface involve $P_3 = P_3'$, the last two hydrodynamical variables to solve are ρ_3 and ρ_3', which can be achieved by using relations (4.40) and (4.41), respectively, thus yielding.

$$\rho_3 = \frac{\rho_1(p_3 - p_1)}{(p_3 - p_1) - v_1^2\rho_1}, \tag{4.51}$$

$$\rho_3' = \frac{\rho_2(p_3 - p_2)}{(p_3 - p_2) - v_2^2\rho_2}, \tag{4.52}$$

Finally, in order to obtain the velocity of the shocks on the moving frame, we select a positive direction to the right see Fig. 4.1, so we obtain:

$$\beta_{sa} = -v_2, \tag{4.53}$$

$$\beta_{sb} = -v_2 + v_{sb} = b_2, \tag{4.54}$$

§4.3 Strong Shock Conditions

Case A

For strong shock conditions we have $P_3/P_1 \gg 1$, so we rewrite the equations (4.2)

$$b_1^2 = \frac{1}{2}(c_{s3}^2/\kappa)\left[(\kappa+1)P_3/P_1\right], \tag{4.55}$$

$$b_3^2 = \frac{1}{2}(c_{s1}^2/\kappa)\left[\kappa-1\right], \tag{4.56}$$

For case A, we rewrite equations (4.8), (4.9), (4.7) with the strong shock conditions $M_1 >> 1$ and $M_3^2 = (\kappa-1)/2\kappa$.

$$P_3 \approx P_1\left[\frac{2\kappa M_1^2}{\kappa+1}\right] = \frac{2\rho_1 P_1}{\kappa+1}, \tag{4.57}$$

$$b_3 \approx b_1\left[\frac{\kappa-1}{\kappa+1}\right], \tag{4.58}$$

$$\rho_3 \approx \rho_1\left[\frac{\kappa+1}{\kappa-1}\right], \tag{4.59}$$

Case B

For strong shock conditions we have $P_3'/P_2 \gg 1$, so we rewrite equations (4.11)

$$b_2^2 = \frac{1}{2}(c_{s3}^{'2}/\kappa)\left[(\kappa+1)P_3'/P_2\right], \tag{4.60}$$

$$b_3^{'2} = \frac{1}{2}(c_{s2}^2/\kappa)\left[\kappa-1\right], \tag{4.61}$$

For case B, we rewrite equations (4.16), (4.17), (4.18) with the strong shock conditions $M_2 >> 1$ and $M_3^{'2} = (\kappa-1)/2\kappa$.

$$P_3' \approx P_2\left[\frac{2\kappa M_2^2}{\kappa+1}\right] = \frac{2\rho_2 P_2}{\kappa+1}, \tag{4.62}$$

$$b_3' \approx b_2\left[\frac{\kappa-1}{\kappa+1}\right], \tag{4.63}$$

$$\rho_3' \approx \rho_2\left[\frac{\kappa+1}{\kappa-1}\right], \tag{4.64}$$

the strong shock conditions over (4.34), (4.36), (4.42) and (4.43) are:

$$v_{sa} \approx \frac{v_1(\kappa-1)}{2}, \tag{4.65}$$

$$v_{sb} \approx \frac{v_2(\kappa-1)}{2}, \tag{4.66}$$

$$v_1 \approx \sqrt{\frac{\left[2\kappa M_1^2+\kappa+1\right]2P_1}{(\kappa+1)^2\rho_1}} = \sqrt{\frac{4\rho_1 b_1^2 - 2P_1(\kappa+1)}{(\kappa+1)^2\rho_1}}, \tag{4.67}$$

$$v_2 \approx \sqrt{\frac{\left[2\kappa M_2^2+\kappa+1\right]2P_2}{(\kappa+1)^2\rho_2}} = \sqrt{\frac{4\rho_2 b_2^2 - 2P_2(\kappa+1)}{(\kappa+1)^2\rho_2}}, \tag{4.68}$$

$$\tag{4.69}$$

§4.4 Injected Energy

Taking the Rankine-Hugoniot jump conditions in energy:

$$\frac{1}{2}b_1^2 + \epsilon_1 + \frac{P_1}{\rho_1} = \frac{1}{2}b_3^2 + \epsilon_3 + \frac{P_3}{\rho_3}, \tag{4.70}$$

$$\frac{1}{2}b_3'^2 + \epsilon_3' + \frac{P_3'}{\rho_3'} = \frac{1}{2}b_2^2 + \epsilon_2 + \frac{P_2}{\rho_2}, \tag{4.71}$$

Case A

Substituting (4.8), (4.9), (4.7) in (4.70)

$$\frac{1}{2}b_1^2 + \epsilon_1 + \frac{P_1}{\rho_1} = \frac{1}{2}\left[\left[\frac{2}{M_1^2(\kappa+1)} + \frac{(\kappa-1)}{\kappa+1}\right]b_1\right]^2 + \epsilon_3 + \frac{P_1\left[\frac{2\kappa M_1^2-(\kappa-1)}{\kappa+1}\right]}{\left[\frac{2}{M_1^2(\kappa+1)} + \frac{(\kappa-1)}{\kappa+1}\right]^{-1}\rho_1}, \tag{4.72}$$

For the case A, the kinetic energy on the strong shock reference system, given by the preshock kinetic energy, is:

$$E_{k3} = \frac{1}{2}\beta_3^2\rho_3, \tag{4.73}$$

Case B

Substituting (4.16), (4.17), (4.18) in (4.71)

$$\frac{1}{2}\left(\left(\frac{(\kappa-1)M_2^2+2}{(\kappa+1)M_2^2}\right)b_2\right)^2+\epsilon_3'+\frac{\left(\frac{2\kappa M_2^2}{\kappa+1}-\frac{\kappa-1}{\kappa+1}\right)P_2}{\rho_3'}=\frac{1}{2}b_2^2+\epsilon_2+\frac{P_2}{\rho_2}, \tag{4.74}$$

For the case B, the kinetic energy on the strong shock reference system, given by the preshock kinetic energy, is:

$$E_{k3}'=\frac{1}{2}\beta_3'^2\rho_3', \tag{4.75}$$

The thermal energies for both cases are:

$$Et_3=\frac{3}{2}\frac{KT_3'}{m}=\frac{3}{2}\frac{KT_2}{m}\frac{\left[2\kappa M_2^2-(\kappa-1)\right]\left[(\kappa-1)M_2^2+2\right]}{(\kappa+1)^2M_2^2}, \tag{4.76}$$

$$E't_3=\frac{3}{2}\frac{KT_3}{m}=\frac{3}{2}\frac{KT_1}{m}\frac{\left[2\kappa M_1^2-(\kappa-1)\right]^{\frac{3}{2}}\left[(\kappa-1)M_1^2+2\right]^{\frac{1}{2}}}{(\kappa+1)^2M_1}, \tag{4.77}$$

The strong shock conditions over the Mach number are given by:

$$M_1\gg 1, \tag{4.78}$$

$$M_2\approx M_1\frac{\kappa-1}{\kappa+1}\left[\frac{\kappa+1}{2\kappa(\kappa-1)M_1^2}\right]^{\frac{1}{2}}=\left(\frac{\kappa-1}{2\kappa}\right)^{\frac{1}{2}}, \tag{4.79}$$

The Thermal energies on strong shock conditions are given by :

$$\frac{3}{2}\frac{KT_1}{m}\longrightarrow 0, \tag{4.80}$$

$$\frac{3}{2}\frac{KT_3}{m}=\frac{3}{2}\frac{2\kappa(\kappa-1)K}{(\kappa+1)^2m}T_1M_1^2=\frac{3(\kappa-1)}{(\kappa+1)^2}u_1^2=\frac{3(\kappa-1)}{(\kappa+1)^2}(\bar{v_{sb}}+\bar{v_2})^2, \tag{4.81}$$

§4.5 Thin layer conditions over front shock

It is possible to obtain the velocity of the shock in terms of the injection velocity over a medium of constant pressure from the conservation equation of flux moment for a shock within the thin working surface approximation (Norman et al., 1983)

$$U_{rp} = V_b \left(1 + \sqrt{\frac{\rho_m}{\rho_b}}\right)^{-1}, \tag{4.82}$$

Where U_{rp} is the velocity of the working surface, V_b is the injected fluid velocity and the densities of the external medium and injected fluid are given by ρ_m and ρ_b.

Identifying the variables respect to the moving system of reference, we get:

$$U_{rp} = \beta_1 \left(1 + \sqrt{\frac{\rho_2}{\rho_1}}\right)^{-1}, \tag{4.83}$$

Imposing the strong shock conditions in (4.59) and (4.64), we obtain the following condition:

$$\frac{\rho_2}{\rho_1} = \frac{\rho_3^{'}}{\rho_3}, \tag{4.84}$$

This last condition imposes a necessary condition over the Mach number $M_1 = M_2$, from which we can see this constitutes as thin working surface.

Mon. Not. R. Astron. Soc. **000**, 1–5 (2013) Printed 27 May 2015 (MN LATEX style file v2.2)

A hydrodynamical model for light curves

Y. Coronado[1⋆], S. Mendoza[1⋆ ⋆]
[1] *Instituto de Astronomía, Universidad Nacional Autónoma de México, AP 70-264, 04510 Distrito Federal, México*

27 May 2015

ABSTRACT
In this work we present the analytical solution in one dimension to the problem of a working surface moving inside a static medium, without the classical thin surface approximation. This allows us to describe a jet depending on the injected hydrodynamical variables of the jet and external density and pressure. We obtain the energy release of the working surface in terms of the jet and external medium variables. When compared with previous works, we recover the thin surface solution. Finally, we compare this analytical solution to the light curve of the radio source 3C120, a well-know FR-I galaxy from 2002 to 2007, using a stepped variation of the injected velocity profile. This simple approximation reproduces the general trend of the light curve.

Key words: Hydrodynamics - galaxies: jets

1 INTRODUCTION

One of the most prominent features of active galaxies are their bipolar outflows with high speed flux and extreme collimated flows, knows as jets. These connect and transport material from the nucleus to the lobes.

Morphology studies of jets are classified into two objects FR-I and FR-II taking in account the luminosity ratio between the core and the lobes in radio wavelengths, and describing the first one as weak jets, and the second as strong collimated jets.

The first hydrodynamical models tried to explain this dichotomy of jets morphology in terms of the density ratio between the jet and external medium $\eta = \rho_b/\rho_m$ and the beam Mach number M_b. The third parameter, the adiabatic index ,is fixed by assuming a pressure matched jet $K = P_b/P_m$. All these studies take in account a balance of pressure and the conservation laws of hydrodynamics (Norman et al. 1983).

Most of the analytical models for internal shocks in the theoretical frame were developed using the definition of working surfaces, with two shock waves separated by a contact surface with an approximation of thin layer. These layers produce all the radiated energy observed on the knots of jets as internal shocks of jets.

In the spirit to describe a full analytical solution for a working surface without the thin layer approximation, we present an analytical solution in terms of the jet and medium hydrodynamical variables. In order to do this, we use two auxiliary systems of reference and their associated solutions. The first system considers the two shocks of the working surface as stationary while the second one takes the contact discontinuity as stationary. The solution is given a third system of reference with a working surface advance outwards in a stationary medium.

⋆ E-mail address: coronado@astro.unam.mx (YC), sergio@astro.unam.mx(SM).

2 MODEL

We construct an analytical solution to the problem of a working surface moving inside a jet, produced by the interaction of two parcels of fluid shocked by a difference of velocities between them, this produce a working surface, ie. two shock waves with a contact discontinuity inside of them.

The purpose of this work is to attempt to solve the problem without using the thin surface approximation, which regards the working surface as having an infinitesimal width. To do this, we define two auxiliary systems of reference in order to solve the problem in terms of the hydrodynamical variables of injection and external medium where the jet propagates.

As we described previously, the working surface consists of two shocks and a contact surface. The first system of reference regards the two shock waves as stationary in two separate cases. The second system of reference takes the contact surface as stationary, leading both shock waves to move away from the stationary point.

The last system of reference corresponds to a moving working surface over a stationary external medium that is equivalent to moving the second system of reference and taking the velocity transformation into account.

All of these systems are shown in figure 1, indicating their corresponding transformation of velocities and direc-

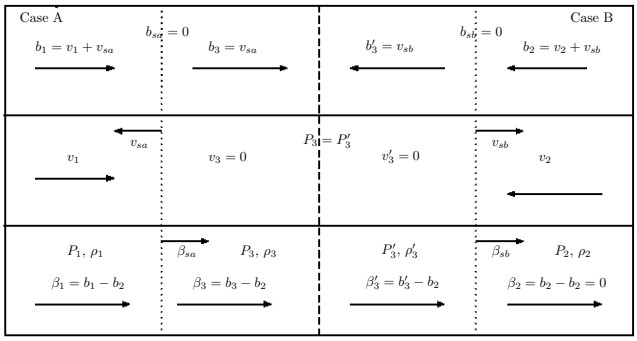

Figure 1. Systems of reference for a working surface, where the arrows indicate the directions of the flow or the shock waves, the dotted lines are the shock waves and the dashed line stands for the contact discontinuity. The top panel shows two stationary shock waves that move towards the center. We divide this into two isolated cases. The middle panel presents a static working surface centred on the contact discontinuity. The bottom panel corresponds to a working surface moving inside a stationary medium.

tions, as well the hydrodynamical conditions over working surface.

The first system of reference is divided into two cases. We assume that the two shock waves are independent solving each case, obtaining the pressure, density and speed of the third and primed third zones in terms of the first and second zones respectively.

$$\rho_3 = \left[\frac{(\gamma+1)M_1^2}{(\gamma-1)M_1^2+2}\right]\rho_1 \tag{1}$$

$$P_3 = \left[\frac{2\gamma M_1^2-(\gamma-1)}{\gamma+1}\right]P_1 \tag{2}$$

$$b_3 = \left[\frac{2+M_1^2(\gamma-1)}{M_1^2(\gamma+1)}\right]b_1 \tag{3}$$

where M_1 corresponds to the Mach number of the first region, defined in the shock stationary system, i.e., $M_1 = b_1/c_1$ where b_1 is the speed of the first fluid, and c_1 is the speed of sound of this region.

$$P'_3 = \left[\frac{2\gamma M_2^2-(\gamma-1)}{\gamma+1}\right]P_2 \tag{4}$$

$$b'_3 = \left[\frac{(\gamma-1)M_2^2+2}{(\gamma+1)M_2^2}\right]b_2 \tag{5}$$

$$\rho'_3 = \left[\frac{(\gamma+1)M_2^2}{(\gamma-1)M_2^2+2}\right]\rho_2 \tag{6}$$

where M_2 correspond to the Mach number of the second region, defined in the shock stationary system i.e., $M_2 = b_2/c_2$ where b_2 is the speed of the second fluid, and c_2 is the speed of sound of this region.

Using the coordinate transformation between the different systems of reference and the ratio of speed regions for the cases A and B, we find the speed of the shocks v_{sa} and v_{sb} of the stationary contact surface system of reference, obtaining:

$$vsa = -\frac{(\gamma+1)v_1}{4} \pm \frac{\sqrt{[(\gamma+1)v_1]^2+16c_{sa}^2}}{4} \tag{7}$$

where $c_{sa} = v_{sa}/M_{sa}$ is the speed of sound associated to the shock in the interface of zones one and three.

$$v_{sb} = -\frac{v_2(\gamma+1)}{4} \pm \frac{\sqrt{[v_2(\gamma+1)]^2+16c_{sb}^2}}{4} \tag{8}$$

where $c_{sa} = v_{sa}/M_{sa}$ is the speed of sound associated to the shock in the interface of zones three prime and two.

According to (Landau & Lifshitz 1987), the conditions of contact surface force this region to present a constant pressure at both sites, in other words, the pressure of regions three and three prime are the same $P_3 = P'_3$. Using this and equations (2) and (4) we get:

$$P_1\left[\frac{2\gamma M_1^2-(\gamma-1)}{\gamma+1}\right] = \left[\frac{2\gamma M_2^2-(\gamma-1)}{\gamma+1}\right]P_2 \tag{9}$$

$$\Longrightarrow M_2 = \frac{\sqrt{\frac{2\,M_1^2 P_1}{P_2}+\frac{P_1}{\gamma P_2}-\frac{P_1}{P_2}-\frac{1}{\gamma}+1}}{\sqrt{2}} \tag{10}$$

from the expression for the injection speed in the full moving system of reference, $\beta_1 = b_1 - b_2$, we obtain a relation between the Mach number at the first and second shocks that constitute the working surface.

$$\begin{aligned}\beta_1 &= b_1 - b_2\\ \frac{\beta_1}{c_1} &= \frac{b_1-b_2}{c_1}\\ m_1 &= M_1 - \frac{b_2}{c_1}\\ m_1 = M_1 - M_2\frac{c_2}{c_1} &\Longrightarrow M_2 = (M_1-m_1)\frac{c_1}{c_2}\end{aligned}$$

using (10) and the previous expression, we solve for M_1.

$$\begin{aligned}M_1 \quad = \quad & \frac{2{c_1}^2\gamma m_1 P_2}{2{c_1}^2\gamma P_2 - 2{c_2}^2\gamma P_1} \pm \frac{\sqrt{2}c_2}{2{c_1}^2\gamma P_2 - 2{c_2}^2\gamma P_1}\\ & \left[\left[2{c_1}^2\gamma^2{m_1}^2+\gamma\left({c_2}^2+{c_1}^2\right)(1-\gamma)\right]P_1P_2\right.\\ & \left.+\left(\left({c_1}^2\gamma(\gamma-1)\right){P_2}^2+\left({c_2}^2\gamma\left(\gamma-1\right)\right){P_1}^2\right]^{1/2}\right.\end{aligned} \tag{11}$$

substituting in (10), we solve for M_2,obtaining a final expression of the Mach number in terms or the injected and ambient hydrodynamical variables $\beta 1$, P_1, ρ_1 and $\beta_2 = 0$, P_2, ρ_2, respectively.

Furthermore, using the expression (100.1) from Landau & Lifshitz (1995), the pressure and density obtained on the shock rest frame, we solve for v_1 and v_2 thus obtain:

$$v_1 = \sqrt{P_3 - P_1}\sqrt{(1/\rho_1)-(1/\rho_3)} \tag{12}$$

$$v_2 = -\sqrt{P_3 - P_2}\sqrt{(1/\rho_2)-(1/\rho'_3)} \tag{13}$$

now we substitute the equations (2) (1), (4) and (6) on the expressions (12) and (13), in order for them to be stated in terms of Mach numbers M_1 and M_2.

$$v_1 = \sqrt{\frac{2M_1^2 - 2}{(\gamma+1)\rho_1 M_1^2}}\sqrt{\frac{(2\gamma M_1^2 - 2\gamma)P_1}{(\gamma+1)M_1^2}} \tag{14}$$

$$v_2 = -\sqrt{\frac{2M_2^2 - 2}{(\gamma+1)\rho_2 M_2^2}}\sqrt{\frac{(2\gamma M_2^2 - 2\gamma)P_2}{(\gamma+1)M_2^2}} \tag{15}$$

solving for P_3 from equation (12) we obtain in terms of Mach numbers:

$$P_3 = \frac{2\gamma M_1^2 + P_1[M_1^2(\gamma+1) - 2\gamma]}{(\gamma+1)M_1^2} \tag{16}$$

Because of the conditions over the contact surface imply that $P_3 = P_3'$, the last two hydrodynamical variables to solve are ρ_3 and ρ_3' which can be achieved using relations (12) and (13), respectively, and thus obtaining.

$$\rho_3 = \frac{\rho_1(p_3 - p_1)}{(p_3 - p_1) - v_1^2\rho_1} \tag{17}$$

$$\rho_3' = \frac{\rho_2(p_3 - p_2)}{(p_3 - p_2) - v_2^2\rho_2} \tag{18}$$

Finally, in order to obtain the velocity of the shocks on the moving frame, we select a positive direction to the right see Fig. 1, so we obtain:

$$\beta_{sa} = -v_2 \tag{19}$$

$$\beta_{sb} = -v_2 + v_{sb} = b_2 \tag{20}$$

2.1 Strong Shock Conditions

One of the most important and useful approximations are the strong shock conditions given by $\frac{P_3}{P_1} \gg 1$ and $\frac{P_3'}{P_2} \gg 1$ for the casea A and B respectively. These approximations are equivalent to $M_1 >> 1$ and $M_3^2 = (\gamma-1)/2\gamma$ for case A and $M_2 >> 1$ and $M_3'^2 = (\gamma-1)/2\gamma$ for case B, we get rewritten equations (2), (3), (1).

$$P_3 \approx P_1\left[\frac{2\gamma M_1^2}{\gamma+1}\right] = \frac{2\rho_1 P_1}{\gamma+1} \tag{21}$$

$$b_3 \approx b_1\left[\frac{\gamma-1}{\gamma+1}\right] \tag{22}$$

$$\rho_3 \approx \rho_1\left[\frac{\gamma+1}{\gamma-1}\right] \tag{23}$$

and the equations (4), (5) and (6).

$$P_3' \approx P_2\left[\frac{2\gamma M_2^2}{\gamma+1}\right] = \frac{2\rho_2 P_2}{\gamma+1} \tag{24}$$

$$b_3' \approx b_2\left[\frac{\gamma-1}{\gamma+1}\right] \tag{25}$$

$$\rho_3' \approx \rho_2\left[\frac{\gamma+1}{\gamma-1}\right] \tag{26}$$

And the strong shock conditions over (7), (8), (14) and (15) are:

$$v_{sa} \approx \frac{v_1(\gamma-1)}{2} \tag{27}$$

$$v_{sb} \approx \frac{v_2(\gamma-1)}{2} \tag{28}$$

$$v_1 \approx \sqrt{\frac{[2\gamma M_1^2 + \gamma + 1]\,2P_1}{(\gamma+1)^2\rho_1}} = \sqrt{\frac{4\rho_1 b_1^2 - 2P_1(\gamma+1)}{(\gamma+1)^2\rho_1}} \tag{29}$$

$$v_2 \approx \sqrt{\frac{[2\gamma M_2^2 + \gamma + 1]\,2P_2}{(\gamma+1)^2\rho_2}} = \sqrt{\frac{4\rho_2 b_2^2 - 2P_2(\gamma+1)}{(\gamma+1)^2\rho_2}} \tag{30}$$

$$\tag{31}$$

3 ENERGETIC CONDITIONS.

For the calculation of the energy inside the working surface we take the strong shock conditions over the Mach number:

$$M_1 \gg 1 \tag{32}$$

$$M_2 \approx M_1\frac{\gamma-1}{\gamma+1}\left[\frac{\gamma+1}{2\gamma(\gamma-1)M_1^2}\right]^{\frac{1}{2}} = \left(\frac{\gamma-1}{2\gamma}\right)^{\frac{1}{2}} \tag{33}$$

for cases A and B, we get the kinetic energy per volume of the region three and three prime as:

$$E_{k3} = \frac{1}{2}\beta_3^2\rho_3 \tag{34}$$

$$E_{k3}' = \frac{1}{2}\beta_3'^2\rho_3' \tag{35}$$

In this case the thermal energy for both cases are:

$$E_{t3} = \frac{3}{2}\frac{KT_2}{m}\frac{\left[2\gamma M_2^2 - (\gamma-1)\right]\left[(\gamma-1)M_2^2 + 2\right]}{(\gamma+1)^2 M_2} \tag{36}$$

$$E_{t3}' = \frac{3}{2}\frac{KT_1}{m}\frac{\left[2\gamma M_1^2 - (\gamma-1)\right]^{\frac{3}{2}}\left[(\gamma-1)M_1^2 + 2\right]^{\frac{1}{2}}}{(\gamma+1)^2 M_1} \tag{37}$$

The thermal energy on strong shock conditions is:

$$\frac{3}{2}\frac{KT_1}{m} \longrightarrow 0 \tag{38}$$

$$\frac{3}{2}\frac{KT_3}{m} = \frac{3}{2}\frac{2\gamma(\gamma-1)K}{(\gamma+1)^2 m}T_1 M_1^2 = \frac{3(\gamma-1)}{(\gamma+1)^2}(\bar{v_{sb}} + \bar{v_2})^2 \tag{39}$$

If we calculate now the total kinetic energy inside of the working surface $E_{kin} = E_{k3} + E_{k3}'$ and assume it is completely radiated away, then the luminosity $L := dE_{kin}/dt$ of the working surface is given by:

$$L = \rho_3\frac{d\beta_3}{dt} + \frac{1}{2}\beta_3^2\frac{d\rho_3}{dt} + \rho_3'\frac{d\beta_3'}{dt} + \frac{1}{2}\beta_3'^2\frac{d\rho_3'}{dt} \tag{40}$$

4 THIN LAYER CONDITIONS OVER THE SHOCK FRONT

Using the conservation equation for flux momentum of a shock in the thin working surface approximation, it is possible to get the velocity of the shock in terms of the injection velocity cover a medium of constant pressure as (Norman et al. 1983)

$$U_{rp} = V_b \left(1 + \sqrt{\frac{\rho_m}{\rho_b}}\right)^{-1} \tag{41}$$

where U_{rp} is the velocity of the working surface, V_b is the injected fluid velocity and the density of the external medium and injected fluid are given by ρ_m and ρ_b.

Identifying the variables with regards the moving system of reference, we have:

$$U_{rp} = \beta_1 \left(1 + \sqrt{\frac{\rho_2}{\rho_1}}\right)^{-1} \tag{42}$$

imposing the strong shock conditions in (23) and (26), we obtain the following condition:

$$\frac{\rho_2}{\rho_1} = \frac{\rho_3^{'}}{\rho_3} \tag{43}$$

This last condition imposes a necessary condition over the Mach number $M_1 = M_2$, from which we see this constitutes a thin working surface, thus recovering the general case of the approximation.

5 LIGHT CURVES

As an application of this analytical description using the energetic conditions (34)-(37), let us consider a change in the injected speed. We assume the injected velocity v has a pulse form given by:

$$v(t) = v_0 + \eta v_0 \tag{44}$$

in which the constant $\eta > 1$ and applied in a short period of time. With this expression for the speed, it is possible to solve the energy equations and integrate them over a period of time, calculating the total luminosity (40).

Due to the model dependencies on the hydrodynamical variables, velocity, pressure and density of the jet as well the ambient medium, we have performed a test of the model in one particular case of jets: the extragalactic jet of 3C120, an active galactic nuclei classified as a Fanaroff-Riley class I source (Fanaroff & Riley 1974) with a prominent one-side jet extending to about 100 Kpc (Walker et al. 1987). The host galaxy has a redshift z=0.033 (Baldwin et al. 1980) with a luminous distance of 138 Mpc with cosmological parameters $H_0 = 73 km/s/Mpc$, $\Omega_m = 0.27$ and $\Omega_0 = 0.73$.

The radio observations of 3C120 at 43 and 22 GHz show that the inner radio structure exhibits a subluminal to superliminal transition on very small scales. The 3C 120 jet shows superluminal knots and it has been suggested that the jet structure in their innermost zone may be described by components interacting with the external medium.

In order to test the model, we selected the light curve observations in radio at 37 GHz of 3C 120, from 2002 to 2007 (Marscher et al. 2002). The model is applied to the burst of late 2003.

The following considerations were included for the parameters of the model: the rate of density and pressure are $\rho_j/\rho_m \approx 10^{-4}$ and $P_j/P_m \approx 8$. The jet advance inside a stationary medium $\beta_2 = 0$ and the injected speed is determined by a fit of the light curve, using the values of pressure and density of the simulations of (Bordas et al. 2011). Therefore, the calculation of the total energy require a volume of the jet with an opening angle of 10 (Agudo et al. 2012). Assuming that the shock that produces the burst observed at the end of 2003 is located at 1 Kpc from the core, we could obtain a volume of $10^{42} m^3 = 10^{-2} pc^3$ for the region of emission.

Using the luminous distance, we obtain a total luminosity in radio at 37 GHz with the best selection of parameters by a ξ^2 test over speed, fixing the pressure and density according to table 1.

In figure 2 we present the best fit to the light curve taking a long decay curve, which gives us a general behaviour of the light curve of the speed fluid of the bulk velocity $v_0$and a small variation of the speed ηv_0 producing the shock, leading to a burst over the light curve.

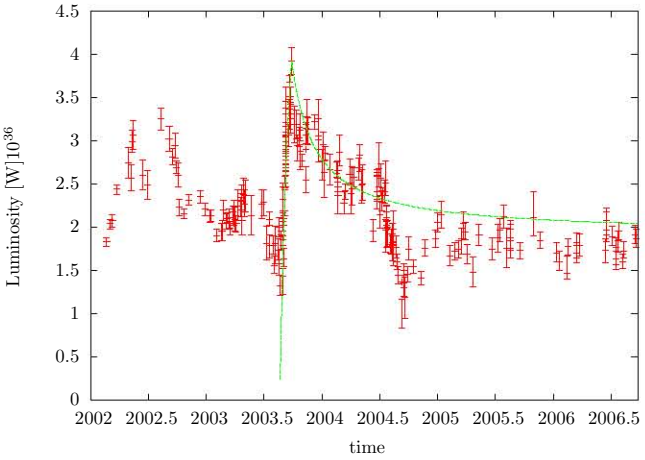

Figure 2. Observational data of 3C120 at 32 GHz from 2002 to 2007. The line corresponds to the best model fit for a long burst as a test of the hydrodynamical model. Using the data of the table 1.

Parameter	3C120
P_j	1.5×10^{-10}Pa
P_{ext}	0.1875×10^{-10}Pa
ρ_j	5×10^{-23}Kgm^{-3}
ρ_{ext}	1.5×10^{-19}Kgm^{-3}
v_0/c	0.165
$v_0\eta/c$	0.33

Table 1. Hydrodynamical quantities obtained for the outbursts modelled in this work. The pressure and density are assumed to be similar (Bordas et al. 2011). The last two parameters are obtained by a variational model of equation (44). The values of these parameters are accurate to within 10%.

6 DISCUSSION

The development of a classical analytical model for a working surface in terms of the injected and external medium allows to follow the evolution of shocks from a thick layer to

a thin layer without the need for the thin layer approximation used in most of hydrodynamical models (Norman et al. 1983).

This first application to light curves shows the accessible description of a shocks. The case of 3C 120 with a clear relativistic regime (Walker et al. 1987) is successfully reproduced by the model. Unless the model is developed in a classical frame, the values obtained for 3 C120 are a first approach for a relativistic model.

An extension of the model to a relativistic regime is currently under development to obtain a final description of the evolution of internal shock waves in relativistic jets.

7 ACKNOWLEDGMENTS

This work was supported by

REFERENCES

Agudo I., Gómez J. L., Casadio C., Cawthorne T. V., Roca-Sogorb M., 2012, ApJ, 752, 92

Baldwin J. A., Carswell R. F., Wampler E. J., Boksenberg A., Smith H. E., Burbidge E. M., 1980, ApJ, 236, 388

Bordas P., Bosch-Ramon V., Perucho M., 2011, MNRAS, 412, 1229

Fanaroff B. L., Riley J. M., 1974, MNRAS, 167, 31P

Landau L., Lifshitz E., 1987, Fluid Mechanics, 2th ed. edn. Course of Theoretical Physics Vol. 6, Pergamon

Landau L., Lifshitz E., 1995, Fluid Mechanics, 2nd ed. edn. Course of Theoretical Physics Vol. 2, Pergamon

Marscher A. P., Jorstad S. G., Gómez J., Aller M. F., Teräsranta H., Lister M. L., Stirling A. M., 2002, Nature, 417, 625

Norman M. L., Winkler K. H. A., Smarr L., 1983, in Ferrari A., Pacholczyk A. G., eds, Astrophysics and Space Science Library Vol. 103, Astrophysical Jets. pp 227–250

Walker R. C., Benson J. M., Unwin S. C., 1987, ApJ, 316, 546

Conclusions

The phenomena of shock waves moving inside astrophysical jets is described by Mendoza et al. (2009) as periodic variations of velocity or mass injected at the base of the jet. These variations produce ejections of fluid inside the jet, in such a way that a faster fluid overtakes previous slower ejections, producing an initial discontinuity on the hydrodynamical quantities and so, leading to the formation of a working surface, i.e. two shock waves separated by a contact discontinuity. The working surface represents the emission region of the knots inside relativistic jets. The central engine ejects the material at the base of the jet in a preferred direction so that the working surface is described as a collision of two parcels of fluid moving along the jet.

The Mendoza et al. (2009) model assumes that the radiation time scales are small as compared to the characteristic dynamical times of the jet, allowing a ballistic description of the problem with semi-analytical solutions. Under the assumption that the working surface is thin and that there are no mass losses within it, the energy loss inside the working surface can be calculated as the difference between the total energy injected at the base of the jet, and the energy of the flow inside the working surface. Assuming an efficient mechanism which converts all this kinetic energy loss in to radiation power, the luminosity is can be calculated as the time derivative of this radiated energy. This luminosity is a function that depends on the velocities and mass injection rates of the fluid . The simplest assumption to make is that the flow variables are injected in a periodic way since this assumption naturally forces the flow to produce working surfaces moving along the jet. The original model by Mendoza et al. (2009) was constructed to reproduce light curves associated to long gamma-ray bursts.

In this thesis we have used the model of Mendoza et al. (2009) in order to explain multi-wavelength light curves associated to different astrophysical objects: blazars, microquasars and quasars. To do so, the model is used in the most general form and the fits

to different sources were performed using different statistical tools varying from simple χ^2 methods to genetic algorithms. The astrophysical jets modelled were:

(a) The multi-wavelength light curve of the HST-1 knot inside the jet of the galaxy M87. Long time observations of this knot have produced detailed light curves in the X-ray, UV and radio bands. The knot emission developed a maximum intensity in 2005, and all wavelengths show two very clear and well detailed outbursts. In order to model the associated light curves of the HST-1 knot, we used periodic oscillations in the injected flow velocity and mass ejection rate at the base of the jet. The fits of the model parameters to the observational data was performed using a genetic algorithm and the results were obtained with an accuracy grater than a 2-σ statistical confidence level.

The best parameter estimation yields a maximum mass ejection rate discharge at the base of the jet $\dot{m} \sim 10^{-2} M_{\odot}/\mathrm{yr}$ and a maximum Lorentz factor ~ 30, both corresponding to the maximum of the light curve in 2005.

(b) The μ-quasar A06200-00, showing an impressive outburst from 1975 to 1976 produced a well detailed light curve in X-ray bands showing a main outburst followed by a smaller one. We successfully modelled the source using two different scenarios. The first considers two separated superpositioned bursts produced by periodic variations in the injected flow velocity. The second has additional periodic variations in the mass ejection rate. The fits to the observational data was performed with a linear regression analysis to within 10 % of accuracy.

Both scenarios yield a mass ejection rate $\dot{m} \sim 10^{-11} - 10^{-12} M_{\odot}/\mathrm{yr}^{-1}$, in accordance to previous models of the μ-quasar A06200-00, with a maximum Lorentz factor $2.3 - 3.6$.

(c) The blazar PKS 1510-089 observed in γ-rays from 2008 to 2012, exhibit three prominent outbursts in the years 2008, 2009 and 2011. The last one shows a tremendous outburst lasting for almost a week which put the source on the spectacular position of being the most luminous source in γ-rays in the sky so far observed . The high activity in gamma rays and detailed observations was a gift since the source is an excellent candidate to be modelled using the proposal by Mendoza et al. (2009).

The fits to the light curve were performed using periodic velocity variations of the jet for each outburst detected in PKS 1510-089. Using a χ^2 statistical test, Lorentz factors $\Gamma \sim 10 - 380$ and mass injection rates $\dot{m} \sim 2 - 25 \times 10^{-3} M_{\odot}\mathrm{yr}^{-1}$ were inferred.

Such high Lorentz factors have never been inferred in a blazar and the source can be thought of a scaled long gamma-ray burst.

Finally, we presented the firsts steps into a new non-relativistic full hydrodynamical model for a working surface with an analytical solution without the need of the traditional thin layer approximation. This model takes in account all the hydrodynamical variables of the jet to calculate the luminosity of the light curve. The model was applied to fit the light curve associated to the jet of the FR-I galaxy 3C120.

The model of Mendoza et al. (2009) can successfully be applied to different astrophysical objects containing jets such long gamma-ray bursts, quasars, blazars and μ-quasars, showing that possible scaling relations must exist for all the physical phenomena that generate the internal shock waves. Although the original model by Mendoza et al. (2009) approximates the jet with a ballistic description, we presented a new approach to the solution of a working surface for non- relativistic jets. Future developments of this model have to be done relativistically and will be useful for applications of internal shock waves inside high energetic jets associated to long gamma-ray bursts, quasars, blazars and micro-quasars.

Bibliography

Alfvén, H. & Herlofson, N., 1950. Cosmic Radiation and Radio Stars. *Physical Review*, **78**, 616–616.

Baade, W. & Minkowski, R., 1954. Identification of the Radio Sources in Cassiopeia, Cygnus a, and Puppis a. *ApJ*, **119**, 206–+.

Baars, J. W. M., Genzel, R., Pauliny-Toth, I. I. K. & Witzel, A., 1977. The absolute spectrum of CAS A - an accurate flux density scale and a set of secondary calibrators. *åp*, **61**, 99–106.

Bicknell, G. V., 1995. Relativistic Jets and the Fanaroff-Riley Classification of Radio Galaxies. *ApJS*, **101**, 29–+.

Biretta, J. A., Sparks, W. B. & Macchetto, F., 1999. Hubble Space Telescope Observations of Superluminal Motion in the M87 Jet. *ApJ*, **520**, 621–626.

Birkinshaw, M., 1984. The Kelvin-Helmholtz instability for relativistic particle beams. I - Stability analyses in the time and space domains for vortex-sheet flows. *MNRAS*, **208**, 887–903.

Blandford, R. D. & Rees, M. J., 1974. A 'twin-exhaust' model for double radio sources. *MNRAS*, **169**, 395–415.

Blandford, R. D. & Rees, M. J., 1978. Extended and compact extragalactic radio sources - Interpretation and theory. *Physica Scripta*, **17**, 265–274.

Boettcher, M., 2010. Models for the Spectral Energy Distributions and Variability of Blazars. *ArXiv e-prints*.

Bošnjak, Ž. & Daigne, F., 2014. Spectral evolution in gamma-ray bursts: Predictions of the internal shock model and comparison to observations. *Astronomy and Astrophysics*, **568**, A45.

Bowman, M., Leahy, J. P. & Komissarov, S. S., 1996. The deceleration of relativistic jets by entrainment. *MNRAS*, **279**, 899–+.

Buckingham, E., 1915. The Principle of Similitude. *Nature*, **96**, 396–397.

Cantó, J., Raga, A. C. & D'Alessio, P., 2000. Analytic solutions to the problem of jets with time-dependent injection velocities. *MNRAS*, **313**, 656–662.

Castro-Tirado, A. J., Zapatero-Osorio, M. R., Caon, N., Cairos, L. M., Hjorth, J. et al., 1999. Decay of the GRB 990123 Optical Afterglow: Implications for the Fireball Model. *Science*, **283**, 2069.

Chang, C. S., Ros, E., Kovalev, Y. Y. & Lister, M. L., 2010. VLBI detection of the HST-1 feature in the M 87 jet at 2 cm. *åp*, **515**, A38+.

Cheung, C. C., Harris, D. E. & Stawarz, Ł., 2007. Superluminal Radio Features in the M87 Jet and the Site of Flaring TeV Gamma-Ray Emission. *ApJL*, **663**, L65–L68.

Cielo, S., Antonuccio-Delogu, V., Macciò, A. V., Romeo, A. D. & Silk, J., 2014. 3D simulations of the early stages of AGN jets: geometry, thermodynamics and backflow. *MNRAS*, **439**, 2903–2916.

Ciprini, S. & Corbel, S., 2009. Fermi-LAT detection of another rapid GeV flare from the blazar PKS 1510-089. *The Astronomer's Telegram*, **1897**, 1.

Corbel, S. et al., 2002. Large-Scale, Decelerating, Relativistic X-ray Jets from the Microquasar XTE J1550-654.

Cortina, J., 2012. MAGIC detects very high energy gamma-ray emission from the FSRQ PKS 1510-089. *The Astronomer's Telegram*, **3965**, 1.

Curtis, H. D., 1918. The planetary nebulae. *Publications of Lick Observatory*, **13**, 55–74.

D'Ammando, F. et al., 2008. AGILE detection of a gamma-ray source coincident with Blazar PKS 1510-08. *The Astronomer's Telegram*, **1436**, 1.

Das, T. K., 1999. Modelling the Origin of Astrophysical Jets from Galactic and Extragalactic Sources. *ArXiv Astrophysics e-prints*.

De Young, D. S., 1967. Inertial Confinement of Extended Radio Sources. *Nature*, **216**, 129–131.

Elvis, M., Page, C. G., Pounds, K. A., Ricketts, M. J. & Turner, M. J. L., 1975. Discovery of powerful transient X-ray source A0620-00 with Ariel V Sky Survey Experiment. *Nature*, **257**, 656–+.

Esin, A. A., McClintock, J. E. & Narayan, R., 1997. Advection-Dominated Accretion and the Spectral States of Black Hole X-Ray Binaries: Application to Nova Muscae 1991. *Astrophys. J.*, **489**, 865.

Falcke, H., Koerding, E. & Markoff, S., 2004. A Scheme to Unify Low-Power Accreting Black Holes - Jet- Dominated Accretion Flows and the Radio/X-Ray Correlation. *Astron. Astrophys.*, **414**, 895–903.

Falle, S. A. E. G. & Raga, A. C., 1993. The structure of knots in variable stellar jets. I - Symmetric knots. *MNRAS*, **261**, 573–583.

Falle, S. A. E. G. & Raga, A. C., 1995. The structure of knots in variable stellar jets-II. Asymmetric knots. *MNRAS*, **272**, 785–799.

Fender, R., Belloni, T. & Gallo, E., 2005. A Unified Model for Black Hole X-Ray Binary Jets? *Astrophysics and Space Science*, **300**, 1–13.

Fender, R. & Gallo, E., 2014. An Overview of Jets and Outflows in Stellar Mass Black Holes. *Space Science Reviews*, **183**, 323–337.

Fender, R. P., Belloni, T. M. & Gallo, E., 2004. Towards a unified model for black hole X-ray binary jets. *Mon. Not. Roy. Astron. Soc.*, **355**, 1105–1118.

Giroletti, M., Hada, K., Giovannini, G., Casadio, C., Beilicke, M., Cesarini, A., Cheung, C. C., Doi, A., Krawczynski, H., Kino, M., Lee, N. P. & Nagai, H., 2012. The kinematic of HST-1 in the jet of M 87. *Astronomy and Astrophysics*, **538**, L10.

Gopal-Krishna & Wiita, P. J., 2000. Extragalactic radio sources with hybrid morphology: implications for the Fanaroff-Riley dichotomy. *åp*, **363**, 507–516.

Harris, D. E., Cheung, C. C., Biretta, J. A., Sparks, W. B., Junor, W., Perlman, E. S. & Wilson, A. S., 2006. The Outburst of HST-1 in the M87 Jet. *ApJ*, **640**, 211–218.

Harris, D. E., Cheung, C. C., Stawarz, Ł., Biretta, J. A. & Perlman, E. S., 2009. Variability Timescales in the M87 Jet: Signatures of E^2 Losses, Discovery of a Quasi Period in HST-1, and the Site of TeV Flaring. *ApJ*, **699**, 305–314.

Hartman, R. C., Bertsch, D. L., Bloom, S. D., Chen, A. W., Deines-Jones, P. et al., 1999. The Third EGRET Catalog of High-Energy Gamma-Ray Sources. *ApJS*, **123**, 79–202.

Homan, J. & Belloni, T., 2005. The evolution of black hole states. *Astrophys. Space Sci.*, **300**, 107–117.

Jansky, K. G., 1933. Radio Waves from Outside the Solar System. *Nature*, **132**, 66–+.

Jennison, R. C. & Das Gupta, M. K., 1953. Fine Structure of the Extra-terrestrial Radio Source Cygnus I. *Nature*, **172**, 996–997.

Jordán, A., Côté, P., Blakeslee, J. P., Ferrarese, L., McLaughlin, D. E., Mei, S., Peng, E. W., Tonry, J. L., Merritt, D., Milosavljević, M., Sarazin, C. L., Sivakoff, G. R. & West, M. J., 2005. The ACS Virgo Cluster Survey. X. Half-Light Radii of Globular Clusters in Early-Type Galaxies: Environmental Dependencies and a Standard Ruler for Distance Estimation. *ApJ*, **634**, 1002–1019.

Kaiser, C. R., Sunyaev, R. & Spruit, H. C., 2000. Internal shock model for microquasars. *Astronomy and Astrophysics*, **356**, 975–988.

Keppens, R., Porth, O., Monceau-Baroux, R. & Walg, S., 2013. Relativistic HD and MHD modelling for AGN jets. *Plasma Physics and Controlled Fusion*, **55**(12), 124038.

Kolykhalov, P. I. & Sunyaev, R. A., 1984. Radiation of accretion disks in quasars and galactic nuclei. *Advances in Space Research*, **3**, 249–254.

Kuulkers, E., Fender, R. P., Spencer, R. E., Davis, R. J. & Morison, I., 1999. Multiple ejections during the 1975 outburst of A0620-00. *MNRAS*, **306**, 919–925.

Landau, L. & Lifshitz, E., 1995. *Fluid Mechanics*, vol. 2 of *Course of Theoretical Physics*. Pergamon, 2nd ed.

Levinson, A., 2006. High-Energy Aspects of Astrophysical Jets. *International Journal of Modern Physics A*, **21**, 6015–6054.

Longair, M. S., Ryle, M. & Scheuer, P. A. G., 1973. Models of extended radio-sources. *MNRAS*, **164**, 243.

Maccarone, T. J., Fender, R. P. & Ho, L. C., 2006. *From X-Ray Binaries to Quasars: Black Holes on All Mass Scales*.

Madrid, J. P., 2009. Hubble Space Telescope Observations of an Extraordinary Flare in the M87 Jet. *Astronomical Journal*, **137**, 3864–3868.

Margon, B., 1984. Observations of SS 433. *Ann. Rev. Ast. & Ast.*, **22**, 507–536.

Marshall, H. L., Miller, B. P., Davis, D. S., Perlman, E. S., Wise, M., Canizares, C. R. & Harris, D. E., 2002. A High-Resolution X-Ray Image of the Jet in M87. *ApJ*, **564**, 683–687.

Matilsky, T., 1976. V616 Monocerotis (A0620-00). *IAU Cirulars*, **2949**, 1–+.

Meier, D. L., 2001. The Association of Jet Production with Geometrically Thick Accretion Flows and Black Hole Rotation. *ApJL*, **548**, L9–L12.

Mendoza, S., 2002. *Astrofísica Relativista*.

Mendoza, S., Hidalgo, J. C., Olvera, D. & Cabrera, J. I., 2009. Internal shocks in relativistic jets with time-dependent sources. *MNRAS*, **395**, 1403–1408.

Merloni, A., Heinz, S. & Di Matteo, T., 2003. A fundamental plane of black hole activity. *Mon. Not. Roy. Astron. Soc.*, **345**, 1057.

Mészáros, P., 2002. Theories of Gamma-Ray Bursts. *Ann. Rev. Ast. & Ast.*, **40**, 137–169.

Mirabel, I. F. & Rodríguez, L. F., 1998. Microquasars in our Galaxy. *Nature*, **392**, 673–676.

Mitchell, M., 1998. *An introduction to genetic algorithms*. A Bradford book. MIT Press, 1st ed.

Norman, M. L., Winkler, K. H. A. & Smarr, L., 1983. Propagation and morphology of pressure-confined supersonic jets. In A. Ferrari & A. G. Pacholczyk, eds., *Astrophysical Jets*, vol. 103 of *Astrophysics and Space Science Library*, 227–250.

Norman, M. L., Winkler, K.-H. A., Smarr, L. & Smith, M. D., 1982. Structure and dynamics of supersonic jets. *Astronomy and Astrophysics*, **113**, 285–302.

Panaitescu, A., Spada, M. & Mészáros, P., 1999. Power Density Spectra of Gamma-Ray Bursts in the Internal Shock Model. *ApJL*, **522**, L105–L108.

Perley, R. A., Dreher, J. W. & Cowan, J. J., 1984. The jet and filaments in Cygnus A. *ApJL*, **285**, L35–L38.

Piran, T., 2004. The physics of gamma-ray bursts. *Reviews of Modern Physics*, **76**, 1143–1210.

Pucella, G. et al., 2009. AGILE detection of a persistent and very intense gamma-ray flaring state of the blazar PKS 1510-089. *The Astronomer's Telegram*, **1968**, 1.

Raga, A. C., Binette, L., Canto, J. & Calvet, N., 1990. Stellar jets with intrinsically variable sources. *ApJ*, **364**, 601–610.

Raga, A. C. & Kofman, L., 1992. Knots in stellar jets from time-dependent sources. *ApJ*, **386**, 222–228.

Razin, V. A., 1958. The Polarization of Cosmic Radio Radiation at Wavelengths of 1.45 and 3.3 Meters. *Soviet Astronomy*, **2**, 216–+.

Reber, G., 1944. Cosmic Static. *ApJ*, **100**, 279–+.

Rees, M. J., 1966. Appearance of Relativistically Expanding Radio Sources. *Nature*, **211**, 468–470.

Rees, M. J., 1978. The M87 jet - Internal shocks in a plasma beam. *MNRAS*, **184**, 61P–65P.

Rees, M. J., 1984. Black Hole Models for Active Galactic Nuclei. *Ann. Rev. Ast. & Ast.*, **22**, 471–506.

Rees, M. J., 1998. Black Holes and Relativistic Stars. **ed. Wald, RM, University of Chicago**, 79–101.

Rees, M. J. & Meszaros, P., 1994. Unsteady outflow models for cosmological gamma-ray bursts. *ApJL*, **430**, L93–L96.

Sahayanathan, S. & Misra, R., 2005. Interpretation of the Radio/X-Ray Knots of AGN Jets within the Internal Shock Model Framework. *ApJ*, **628**, 611–616.

Sams, B. J., Eckart, A. & Sunyaev, R., 1996. Near-infrared jets in the Galactic microquasar GRS1915+105. *Nature*, **382**, 47–49.

Scheuer, P. A. G., 1974. Models of extragalactic radio sources with a continuous energy supply from a central object. *MNRAS*, **166**, 513–528.

Schmidt, M., 1963. 3C 273 : A Star-Like Object with Large Red-Shift. *Nature*, **197**, 1040.

Spada, M., Ghisellini, G., Lazzati, D. & Celotti, A., 2001. Internal shocks in the jets of radio-loud quasars. *MNRAS*, **325**, 1559–1570.

Stawarz, Ł., Aharonian, F., Kataoka, J., Ostrowski, M., Siemiginowska, A. & Sikora, M., 2006. Dynamics and high-energy emission of the flaring HST-1 knot in the M 87 jet. *MNRAS*, **370**, 981–992.

Sunyaev, R., Churazov, E., Gilfanov, M., Pavlinsky, M., Grebenev, S., Babalyan, G., Dekhanov, I., Khavenson, N., Bouchet, L., Mandrou, P., Roques, J. P., Vedrenne, G., Cordier, B., Goldwurm, A., Lebrun, F. & Paul, J., 1991. Three spectral states of 1E 1740.7 - 2942 - From standard Cygnus X-1 type spectrum to the evidence of electron-positron annihilation feature. *ApJL*, **383**, L49–L52.

Taub, A. H., 1948. Relativistic Rankine-Hugoniot Equations. *Physical Review*, **74**, 328–334.

Tramacere, A., 2008. Fermi LAT observations of the PKS 1510-089 outburst. *The Astronomer's Telegram*, **1743**, 1.

Wagner, S. J., Behera, B. & H.E.S.S. Collaboration, 2010. Hess Observations Of Quasars. In *AAS/High Energy Astrophysics Division #11*, vol. 42 of *Bulletin of the American Astronomical Society*, 660.

Walg, S., Achterberg, A., Markoff, S., Keppens, R. & Meliani, Z., 2013. Relativistic AGN jets I. The delicate interplay between jet structure, cocoon morphology and jet-head propagation. *MNRAS*, **433**, 1453–1478.

Westerhout, G., Seeger, C. L., Brouw, W. N. & Tinbergen, J., 1962. Polarization of the galactic 75-cm radiation. *Bulletin Astronomical Institute of the Netherlands*, **16**, 187–+.